UNIVERSITY OF OKLAHOMA

GRADUATE COLLEGE

TURBULENT TRANSPORT AND SURFACE INTERACTIONS WITHIN INHOMOGENEOUS ATMOSPHERIC ENVIRONMENTS: AN EVALUATION OF PARAMETERIZATION SCHEMES IN THE WEATHER RESEARCH AND FORECASTING MODEL

A THESIS

SUBMITTED TO THE GRADUATE FACULTY

in partial fulfillment of the requirements for the

Degree of

MASTER OF SCIENCE IN METEOROLOGY

By

JEREMY A. GIBBS

Norman, Oklahoma

2008

TURBULENT TRANSPORT AND SURFACE INTERACTIONS WITHIN INHOMOGENEOUS ATMOSPHERIC ENVIRONMENTS: AN EVALUATION OF PARAMETERIZATION SCHEMES IN THE WEATHER RESEARCH AND FORECASTING MODEL

A THESIS APPROVED FOR THE
SCHOOL OF METEOROLOGY

By

Prof. Evgeni Fedorovich

Prof. Lance Leslie

Dr. Alexander van Eijk

Dedication

This thesis is dedicated to my sister and mom for their unwavering support throughout this journey.

I also dedicate this thesis to the love of my life, Larissa Hines, whose love and support are the foundation upon which I stand in life.

"The important thing is not to stop questioning." - Albert Einstein

Acknowledgements

Firstly, this thesis would not have been possible without the generous support from TNO Defense, Security, and Safety located in Den Haag, Netherlands through the contract FY07-ORA1-40.

I would like to thank my committee members for being so selfless with their time and ideas. I greatly appreciated Dr. Lance Leslie's down-to-earth approach to suggestions and criticisms. Dr. Alexander van Eijk was especially influential in this study, not only by offering an outside viewpoint to research, but by securing the relationship between the University of Oklahoma and TNO. Without Dr. van Eijk's efforts, this thesis would not have been possible.

A special gratitude is owed to my adviser, Dr. Evgeni Fedorovich. Two years ago, Dr. Fedorovich offered a voice of support to an unproven undergraduate in myself, for which I am forever indebted. His support is so greatly appreciated as it provided an opportunity for me to pursue my educational goals. That opportunity was truly a life-changing gift. Throughout this thesis, Dr. Fedorovich was not only my biggest supporter, but also my biggest critic. His honest and constructive appraisal pushed me to seek excellence in everything. While as busy an any other faculty member, Dr. Fedorovich always offered an open-door policy in which he would drop everything to assist me with my relatively meaningless problems. It is for all of this that I consider Dr. Fedorovich a true mentor and friend.

I have forged lifelong bonds with all of my friends. I am so thankful for the emotional support and camaraderie that they have provided.

I must also thank my family for their unwavering support. I was able to remain even-keeled and keep a healthy perspective on life through their support. I am greatly appreciative to the Hines family for all that they have done for me over the past six years. I would not have attained any success in life without my mom, Sharon Joyner.

She bore me, raised me, supported me, taught me, and loved me. She is a true role model and claims the largest portion of my character.

Finally, I want to express sincere love and appreciation to the most important person in my life, Larissa Hines. Over the past six years, our relationship has blossomed and our love has strengthened. It is through this love that I garner everyday inspiration.

Contents

List Of Tables

List Of Figures

Abstract

The WRF model is a popular tool, both in research and operational meteorology, offering a practical method to model atmospheric quantities at fine grid spacing. However, proper consideration is often not given to the underlying physics of the model, particularly in terms of turbulent transport and surface interactions (TTSI). The use of these schemes requires greater inspection because the parameterization of TTSI sub-grid scale processes becomes increasingly important when employing fine grid spacing within the model. The comparison domain utilized in the WRF model for this study was centered over the Atmospheric Radiation Measurement (ARM) Program site located in Lamont, Oklahoma.

Two cases from June 2007 were chosen based on their meteorological representativeness of late spring conditions in Oklahoma. The Dryline case of June 7th included strong warming, wind shifts, and moisture changes due to the passage of a dryline. The Postfrontal case of June 8th was preceded by the passage of a cold front in the overnight hours and included the associated cooler temperatures, northerly winds, and stronger static stability.

Sensitivity of model predictions was investigated by employing different and sensible configurations of TTSI schemes. Additionally, the model representation of TTSI sub-grid scale processes was examined by studying the comparability of WRF model predictions with observational and fine-scale numerical simulation data. Finally, recommendations are offered on the use of TTSI parameterization schemes in the WRF model under particular meteorological conditions.

Chapter 1

Introduction

1.1 Motivation

Complex mesoscale models are rapidly becoming popular tools in the field of numerical weather prediction (NWP). The capacity of such models to predict atmospheric features at fine grid spacing is paramount to this popularity. The current tendency, both in research and operations, is to implement horizontal grid spacing within the model to the range of 1 to 4km. The practical ease-of-use of NWP models at fine grid spacing is a byproduct of both increased model complexity and an exponential growth in computing capabilities. Unfortunately, the gains in model sophistication have led to an increase in "black-box" users who are simply content to obtain results with the assumption that mesoscale models represent fine-scale atmospheric features with absolute accuracy. This assumption is made without proper regard to the underlying physical parameterization schemes, particularly in terms of turbulent transport and surface interactions (TTSI) within the boundary layer. Large-scale atmospheric features often rely greatly on small-scale phenomena through upscale growth. Subsequently, model predictions may vary substantially depending on how these small-scale processes are represented. This thesis examines the sensitivity of model predictions by employing different and sensible configurations of TTSI schemes. Additionally, the model representation of TTSI sub-grid scale processes is investigated by studying the comparability of WRF model predictions with observational and fine-scale numerical simulation data. Finally, recommendations are offered on the use of TTSI parameterization schemes in the WRF model under particular meteorological conditions.

1.2 The Model

One of the more popular state-of-the-art NWP models is The Weather Research and Forecasting (WRF) model (Skamarock et al. 2008). The WRF model is a highly portable code that can run on a wide range of computing platforms, including both desktop environments and multi-processor supercomputing clusters. The model includes two dynamical solvers, numerous physical parameterization packages, an intricate initialization program, and an advanced three-dimensional variational (3DVAR) data assimilation system. For this study, WRF version 3.0.1 was employed utilizing the Advanced Research WRF (ARW) dynamical core. The ARW solves Euler non-hydrostatic, fully-compressible governing equations of atmospheric dynamics and thermodynamics utilizing the staggered Arakawa C-grid and vertical η-coordinate (Skamarock et al. 2008). The coordinate, also referred to as a mass vertical coordinate, is defined as

$$\eta = (p_h - p_{ht})/\mu \quad \text{where} \quad \mu = p_{hs} - p_{ht} \ . \tag{1.1}$$

Here, p_h is the hydrostatic component of pressure at the considered model level while p_{hs} and p_{ht} represent the hydrostatic component of pressure at the surface and top boundaries, respectively. The η-coordinate is essentially a normalized pressure coordinate, ranging from one at the surface to zero at the top of the domain bounds. Due to this implementation, the vertical grid spacing is stretched with height, unlike the horizontal grid dimensions, which are regularly spaced. To adequately cover the lower atmosphere, one may define more vertical grid levels in the lower portion of the atmosphere than is prescribed by the default interpolation scheme. Figure (1.1) depicts the ARW vertical coordinate.

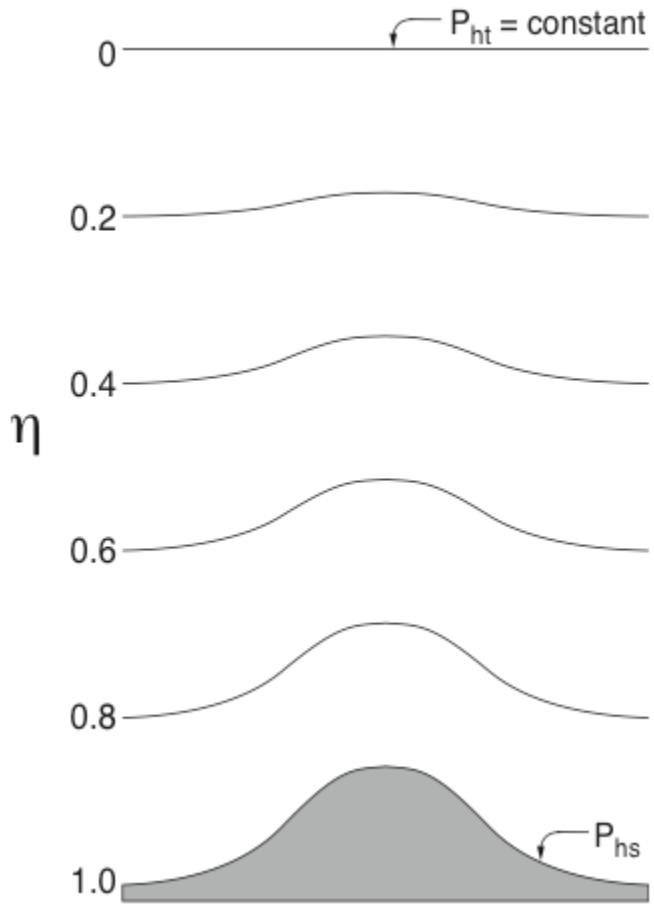

Figure 1.1: The Advanced Research WRF (ARW) vertical η-coordinate. From Skamarock et al. (2008).

In the WRF model, sub-grid scale parameterizations fall into seven categories. These classifications include physical processes within microphysics (MP), cumulus convection (CC), land-surface models (LSM), atmospheric radiation (AR), surface-layer (SL), planetary boundary layer (PBL), and turbulent mixing. This thesis, while providing a brief overview of the MP, CC, LSM, and AR schemes, focuses on the PBL, SL, and turbulent mixing parameterizations.

1.3 Goals

Turbulent transport and the associated surface interactions play a key role in distributing heat, moisture, and momentum throughout the boundary layer. This transport is handled by turbulent eddies. Since these eddies are not generally explicitly resolvable on the mesoscale, their characteristics are parameterized to allow the model to replicate their behavior. These parameterizations feed information to the resolvable portions of the atmosphere. Herein lies the importance of having an accurate scheme to produce realistic behavior of TTSI sub-grid scale processes.

This thesis reviews an in-depth and select subset of TTSI parameterization schemes in the WRF model and describes their interactions. High-resolution WRF model predictions incorporating these sensible options are generated within stressing and inhomogeneous environments. In this case, the term *inhomogeneous* refers to the distinct temporal evolution of meteorological fields beyond normal diurnal fluctuations. The predictions were compared with observational data from the Atmospheric Radiation Measurement (ARM) Program site located in Lamont, Oklahoma (LMN) and fine-scale numerical simulation data from a University of Oklahoma large eddy simulation (LES) following Fedorovich et al. (2001a,b, 2004), hereinafter referred to as LES. Since LES explicitly resolves features on scales considered sub-grid in the WRF model, its solutions are considered as "truth" in this study.

As was mentioned in Stensrud (2007), little has fundamentally changed in model parameterizations over recent decades. Thus, a perspicuous examination of each scheme's behavior may lead to an improved understanding of their associated physical processes. The goal is to present a coherent appraisal of TTSI physics within the WRF model and to offer guidance on their use under particular meteorological conditions.

1.4 Outline of Remaining Chapters

The remaining chapters give an in-depth description of how parameterization processes exist and interact in a mesoscale NWP model, evaluate predictions from such schemes in conjunction with observational and fine-scale numerical simulation data, offer an understanding of the importance of findings, and propose where future research is needed.

Chapter (2) gives a detailed characterization of the physics packages offered within the WRF model. Not only are the fundamentals and theory behind each scheme chronicled, the intricate interfacing of these processes is defined. The latter is of most importance in understanding how parameterizations exist in NWP models. Chapter (3) expounds the model arrangements used for each comparison exercise. Properties of the model domain are explained and configurations for each run are listed. Here, the idea of model spin-up and stable solutions are examined, along with defining realistic lateral boundary conditions (LBC). The description of evaluations made against observational and fine-scale numerical simulation data are described in Chapter (4). It is in this chapter that important findings are detailed and their importance examined. Chapter (5) summarizes the denouement of the exercises, offers explanations, and provide a path for future research and advancements in the topics covered within this thesis.

Chapter 2

Model Physics

Mesoscale models, such as the WRF model, offer a rather succinct procedural methodology to predict atmospheric phenomena. Generally, initial fields of meteorological quantities are provided to the model as a first approximation of the current state of the atmosphere. These fields are often provided by analyses from global models, which include surface and upper-air observations, along with numerous other observational sources, including those from remote sensing instruments. These analyses are found using some type of interpolation procedure that brings the irregularly spaced observations to a regularly spaced grid. The mesoscale NWP model then takes the analyses fields and places them on a grid within the domain of interest. Since most NWP models are at a finer-scale grid spacing than that of the global analyses, further interpolation is needed. The need for multiple interpolation procedures is a large source of error in model predictions, often resulting in the model spin-up problem, as discussed in (3.4). Once the initial fields are placed on the regular grid located within the domain of interest, complex equations progress the model forward in time, resulting in predictions of atmospheric quantities.

However, these methods are constrained by limitations in current computer hardware. Such limits preclude the absolute representation of the atmosphere, both spatially and temporally, by NWP models, even if exact initial fields could be prescribed. Essentially, modern computers have finite memory resources, and as such, cannot allow for a sufficiently large three-dimensional grid. Furthermore, the constraints of computational speed inhibit the instantaneous calculation of meteorological fields in time. Subsequently, concessions are made to overcome such obstacles. These include

the use of finite difference methods to advance the model solutions in time, as well as the parameterization of processes that occur at scales not resolvable due to grid spacing limitations. However, as computers allow for smaller grid spacing, models begin resolving processes that are chaotic in nature. Therefore, an exact realization will never occur and one must consider the meaningfulness of employing finer and finer grid spacing in models.

This thesis focuses on parameterization schemes, particularly in terms of TTSI physics. These schemes are crucial to model predictions because they act to replicate meteorological processes, such as surface fluxes of heat and moisture due to transport by turbulent motions. These small-scale processes greatly influence large-scale solutions through upscale growth, making them worthy of consideration.

2.1 The Importance of Parameterization Schemes

The core of numerical weather prediction models lies in computational fluid dynamics. Much work goes into understanding partial differential equations, developing complex finite difference methods, implementing boundary conditions, and many other serpentine numerical schemes. Often though, the understanding of vital sub-grid scale processes are neglected. Stensrud (2007) describes the importance of such parameterization schemes in numerical models:

> While some may argue in defense that parameterization schemes are fluid and changing all the time, implying that studying them is fruitless, closer inspection reveals that many basic assumptions used in the parameterization of specific processes have changed little over the past decades. The study of parameterization schemes also opens a window that allows one to examine our most fundamental ideas about how these physical processes function and explore how they behave. Thus, the study of parameterization is a vital and necessary component in the study of numerical weather prediction and deserves far greater attention.

Even as models, such as the WRF model, continually improve upon resolvable scales, there will always exist scales that are not captured. Current hardware limitations

preclude such absolute representations of the atmosphere. As such, numerical models must make approximations to physical processes. This is done through finite difference methods and parameterizations of sub-grid scale processes. Take for example a model grid with horizontal spacing of 10km used in a simulation of the convective boundary layer. At this resolution, small clouds or convective eddies exist at spatial extents well within a single grid cell. This means that such a feature cannot be represented directly by the model. While one might be content to simply ignore these smaller features in favor of looking at the bigger synoptic picture, doing so would result in solutions with little physical sense. Such small-scale features must be considered to accurately account for upscale growth contributions. Thus, parameterization schemes are paramount to numerical models as they act to represent complex physical processes and relate them to existing model variables.

As stated in Chapter (1), parameterization options present in the WRF model ARW solver fall into seven categories, each containing several choices. Those categories are MP, CC, AR, LSM, SL, PBL, and turbulent mixing. The first four categories were left unchanged throughout all experiments, and are hereinafter referred to as "baseline physics". The SL, PBL and turbulent mixing schemes are of main importance in this study and are referred to as "TTSI physics". Overviews of each category, along with descriptions of each utilized parameterization scheme, are given according to Skamarock et al. (2008). Further characterization of the interactions among each category is also described.

2.2 Microphysics

The microphysics package includes explicitly resolved water vapor, cloud, and precipitation processes. In the WRF model, microphysics is employed at the end of each time-step as an adjustment process. This guarantees that the final saturation

balance is accurate for the updated temperature and moisture fields. In this respect, the microphysics schemes do not provide tendencies of such atmospheric quantities.

The WRF Single Moment 6-class (WSM6) mixed-phase scheme was used as the MP option. According to Skamarock et al. (2008), as a general rule, grids with horizontal spacing of 10km or less, where updrafts may be resolved, a mixed-phase scheme should be employed. Mixed-phase processes are those that result from the interaction of ice and water particles. An example of such a process is riming, which produces graupel or hail. The six considered classes include vapor, rain, snow, cloud ice, cloud water, and graupel. The WSM6 parameterization uses a diagnostic relation for ice number concentration based on ice mass content rather than temperature, unlike many other MP schemes. The freezing/melting processes are computed during the fall-term sub-steps to increase accuracy in the vertical heating profile of these processes. The order of the processes is also optimized to decrease the sensitivity of the scheme to the model time-step. Saturation adjustment in WSM6 follows Dudhia (1989) and Hong et al. (1998) in separately treating ice and water processes. This differs directly with the Lin et al. (1983) scheme, which handles them as a combined process. The efficiency and theoretical backgrounds of the WSM6 scheme provide adequate reasoning for its use as the MP scheme.

2.3 Cumulus Convection

The cumulus convection schemes represent the sub-grid-scale effects of convective clouds. Namely, they are designed to reproduce vertical fluxes due to unresolved updrafts and downdrafts along with compensating motion outside of the clouds. Cumulus convection schemes are triggered in, and operate in, individual columns. There, they provide vertical heating and moistening profiles along with the convective component of surface rainfall. A select number of these schemes provide cloud and precipitation field tendencies within the column.

According to Skamarock et al. (2008), when horizontal grid spacing is below 3km, no cumulus scheme is needed because convective motions are resolvable at such scales. For this reason, no CC parameterization was implemented in this study.

2.4 Atmospheric Radiation

Atmospheric radiation schemes account for atmospheric heating due to radiative flux divergence and surface downward longwave and shortwave radiation for the ground heat budget. Every radiation scheme is a one-dimensional column model, where each column is treated independently and the associated fluxes correspond to those in infinitely horizontally uniform planes. Longwave radiation includes infrared radiation absorbed and emitted by gases and surfaces. Upward longwave radiation flux from the ground is determined by the surface emissivity that in turn depends on land use type, as well as the ground temperature. Shortwave radiation includes visible and surrounding wavelengths that make up the solar spectrum. In this regard, the only source of shortwave radiation is the sun. However, processes include absorption, reflection, and scattering in the atmosphere and at surfaces. For shortwave radiation, the upward flux is the reflection due to surface albedo. Within the atmosphere the radiation responds to model-predicted cloud and water vapor distributions, as well as specified carbon dioxide, ozone, and trace gas concentrations. Atmospheric radiation schemes provide potential temperature tendencies.

The shortwave radiation scheme used was the Dudhia (1989) parameterization. Originally in The Pennsylvania State University (PSU) 5th-Generation Mesoscale Model (MM5), the scheme has simple downward integration of solar flux, accounting for clear-air scattering, water vapor absorption, and cloud albedo and absorption.

The longwave radiation scheme employed was the rapid radiative transfer model (RRTM) (Mlawer et al. 1997). Taken from MM5, RRTM is a spectral-band scheme

using the correlated-k method. The scheme utilizes pre-set tables to accurately represent longwave processes due to water vapor, ozone, carbon dioxide, and trace gases, as well as accounting for cloud optical depth.

2.5 Land-Surface Model

LSMs use atmospheric information from the SL scheme, radiative forcing from the radiation scheme, and precipitation forcing from the microphysics and convective schemes, together with internal information on the land's state variables and surface properties, to provide heat and moisture fluxes over land and sea-ice points. These fluxes provide a lower boundary condition for vertical transport done in the PBL schemes, or in the vertical diffusion scheme in which a PBL option is not employed, such as in LES mode. LSMs offer various degrees of sophistication in dealing with thermal and moisture fluxes in multiple soil layers and also may handle vegetation, root, and canopy effects along with snow-cover prediction. There is no horizontal interaction between neighboring points, so the LSM may be considered a one-dimensional column model. The LSM provides no tendencies, but does update the land's state variables which include the ground (skin) temperature, soil temperature profile, soil moisture profile, snow cover, and canopy properties.

The Noah LSM is the successor to the OSU LSM described in Chen and Dudhia (2001). The LSM was developed by both the National Center for Environmental Prediction (NCEP) and the National Center for Atmospheric Research (NCAR) and is almost identical to NCEP's operational North American Model (NAM). It was designed to be mutually beneficial to research and operational objectives. Noah is a 4-layer soil temperature and moisture model with canopy moisture and snow cover prediction. It includes root zone, evapotranspiration, soil drainage, and runoff, taking into account vegetation categories, monthly vegetation fraction, and soil texture. The scheme provides sensible and latent heat fluxes to the PBL scheme. Noah LSM

improves upon the OSU LSM urban treatment and now considers surface emission properties. The sophistication of the Noah LSM as compared to the other LSM schemes made it an ideal candidate for the experiments described Chapter (4).

2.6 Surface Layer Schemes

The SL schemes provide friction velocities and exchange coefficients that enable the calculation of surface heat and moisture fluxes by the LSM and surface stress in the PBL scheme. Over water, the surface fluxes and diagnostic fields are computed in the SL scheme itself. Each SL option is tied to a particular PBL scheme. The schemes provide no tendencies, rather only the stability-dependent information about the SL for the LSM and PBL schemes.

There are currently three main SL parameterization options included in the latest release of the WRF model, all based on similarity theory as proposed by Monin and Obukhov (1954). These options include the MM5 scheme, the Janjic scheme, and the Pleim scheme.

2.6.1 Basic Relationships: Monin-Obukhov Similarity Theory

Pleim (2006) succinctly describes the importance of surface layer flux-profile relationships in NWP models.

> Interactive linkages between state variables at the earth's surface and in the atmospheric surface layer are essential components of numerical atmospheric models. Surface fluxes of heat, moisture, momentum, and any other modeled quantity (e.g., trace chemical species) are determined by gradients across the surface-atmosphere interface; at the same time, surface fluxes are critical processes determining the time evolution of these gradients. Hence, simultaneous solution of the surface fluxes and the surface layer profiles is required.

The WRF model, as in most typical atmospheric models, implements surface-layer similarity theory to characterize the flux-profile relationships.

Monin and Obukhov (1954) hypothesized that in the atmospheric surface layer flow, where the considered level is greater than that of the so-called roughness length z_0, the vertical gradients of Reynolds-averaged meteorological fields U, θ, q, and their associated turbulence moments are universal functions of a dimensionless height $\zeta = z/L$ when normalized by the corresponding surface-layer turbulence scales and length scale L. Here U represents velocity (ms^{-1}), θ is potential temperature (K), and q is water vapor mixing ratio (gkg^{-1}). The turbulence scales are given by

$$u_* = (\overline{w'u'}^2 + \overline{w'v'}^2)^{\frac{1}{4}} \ , \tag{2.1a}$$

$$\theta_* = \frac{-\overline{w'\theta'}}{u_*} \ , \quad \text{and} \tag{2.1b}$$

$$q_* = \frac{-\overline{w'q'}}{u_*} \ , \tag{2.1c}$$

with the Obukhov stability length scale given by

$$L = -\frac{\theta_r(\overline{w'u'}^2 + \overline{w'v'}^2)^{\frac{3}{4}}}{g\kappa\overline{w'\theta'_v}} \ , \tag{2.2a}$$

where θ_r designates some reference temperature, g is gravity, κ is von Kármán's constant. Additionally, u', v', and w' represent perturbations of the x-component, y-component, and z-component of velocity, θ' and θ'_v are the perturbations of potential and virtual potential temperature, respectively, and q' represents the perturbation of water vapor mixing ratio. Accordingly, $\overline{w'u'}$ and $\overline{w'v'}$ are kinematic momentum fluxes, $\overline{w'\theta'}$ and $\overline{w'\theta'_v}$ are kinematic heat and virtual heat fluxes, and $\overline{w'q'}$ is the kinematic moisture flux. Reynolds averaging is denoted by $\overline{()}$. L is assumed constant throughout the surface layer since surface-layer turbulent momentum and heat fluxes are assumed constant with height. For a neutrally stratified surface layer, L goes to infinity, the sign of L is undefined, and the integral flux-gradient relation follows the logarithmic profile law. In the stably stratified surface layer, with no turbulent shear stress, L tends to zero. If there exists non-zero turbulent shear stress, L is positive.

For the unstably stratified surface layer with non-zero turbulent shear stress, L is negative. Following the Monin-Obukhov similarity theory, profiles are defined for heat and momentum, respectively, for the non-neutral atmospheric surface layer as

$$\frac{\kappa z}{u_*}\frac{\partial U}{\partial z} = \phi_m\left(\zeta\right) \ , \tag{2.3a}$$

$$\frac{\kappa z}{\theta_*}\frac{\partial \theta}{\partial z} = \phi_h\left(\zeta\right) \ , \quad \text{and} \tag{2.3b}$$

$$\frac{\kappa z}{q_*}\frac{\partial q}{\partial z} = \phi_q\left(\zeta\right) \ . \tag{2.3c}$$

Here, ϕ_m, ϕ_h, and ϕ_q are empirically derived universal functions of dimensionless height ζ. It is often assumed that ϕ_h and ϕ_q are equivalent.

Next, kinematic fluxes of momentum, heat, and moisture are defined in terms of the turbulence scales (u_*, θ_*, and q_* respectively) as

$$F_m = -u_*^2 \ , \tag{2.4a}$$

$$F_h = -u_*\theta_* \ , \quad \text{and} \tag{2.4b}$$

$$F_q = -u_* q_* \ . \tag{2.4c}$$

Finally, the kinematic fluxes are described in terms of state variables by integrating Eq. (2.3) from the roughness height z_0 to height z and combining with Eq. (2.4). These relationships are given by

$$U = \frac{u_*}{\kappa}\left[\ln\left(\frac{z}{z_0}\right) - \psi_m\left(\zeta, \zeta_0\right)\right] \quad \text{and} \tag{2.5a}$$

$$\left(\theta - \theta_0\right) = \frac{\theta_*}{\kappa}\left[\ln\left(\frac{z}{z_0}\right) - \psi_h\left(\zeta, \zeta_0\right)\right] \ , \tag{2.5b}$$

$$\left(q - q_0\right) = \frac{q_*}{\kappa}\left[\ln\left(\frac{z}{z_0}\right) - \psi_h\left(\zeta, \zeta_0\right)\right] \ , \tag{2.5c}$$

where $\zeta_0 = z_0/L$. Additionally, θ_0 and q_0 are the potential temperature and moisture values at the roughness height z_0. ψ_m and ψ_h are stability correction functions given by

$$\psi_m = \int_{\zeta_0}^{\zeta} \frac{1 - \phi_m(\zeta')}{\zeta'} d\zeta' \ , \tag{2.6a}$$

$$\psi_h = \int_{\zeta_0}^{\zeta} \frac{1 - \phi_h(\zeta')}{\zeta'} d\zeta' \ . \tag{2.6b}$$

Similarity theory, however, is not perfect in representing the flux-profile relationship. The main quandary is that potential temperature and moisture values at roughness height z_0 are not generally known in numerical models. Alternatively, θ_0 and q_0 are approximated by the surface skin potential temperature (θ_g) and moisture (q_g)values. Consequently, momentum flux is defined from the gradient down to the roughness height z_0, while heat and moisture fluxes are defined from the gradient down to the surface. This results in an inconsistency between fluxes. This inconsistency is exacerbated on the extreme ends of the meteorological spectrum. For instance, under very stable or very unstable conditions, θ_g and θ_0 can differ by a large margin. Another problem of similarity theory lies in the need to solve the complex stability correction functions. Each SL scheme in the WRF model attempts to alleviate at least one of these dilemmas, if not both.

2.6.2 MM5 Parameterization

Relations between ϕ functions and ζ were experimentally estimated by Dyer and Hicks (1970) for the three major stability regimes discussed in Zhang and Anthes (1982). The regimes are classified as: stable (Ri > 0.2), damped mechanical turbulence ($0.2 >$ Ri > 0), and forced convection (Ri ≤ 0). Here, Ri is the Richardson number, which is the ratio of buoyancy forces to inertial forces. For the stable regime, it assumed that no turbulence exists. Subsequently, based on this premise, the damped mechanical

regime is described as stable in nature and the forced convection regime is considered to be unstable.

For unstable conditions ($\zeta < 0$), when the gradient Richardson number is approximated as $\mathrm{Ri} = \zeta$, the ϕ functions are given by

$$\phi_m = [1 - 16\zeta]^{-\frac{1}{4}} \quad \text{and} \tag{2.7a}$$

$$\phi_h = [1 - 16\zeta]^{-\frac{1}{2}} \ . \tag{2.7b}$$

For stable conditions ($\zeta > 0$), with $\frac{\mathrm{Ri}}{1-5\mathrm{Ri}} = \zeta$,

$$\phi_m = 1 + 5\zeta \quad \text{and} \tag{2.8a}$$

$$\phi_h = 1 + 5\zeta \ . \tag{2.8b}$$

Fluxes can then be found using the "flux-gradient relationship" as described in (2.6.1). Since gradients are defined and the profiles are approximated by the Dyer and Hicks (1970) functions, SL turbulence velocity and temperature scales can be prescribed following Eq. (2.3). Once the surface layer scales are known, turbulent fluxes of heat and momentum are calculated according to Eq. (2.4).

Paulson (1970) found that the relationships given by Dyer and Hicks (1970) performed better compared with those from either a log-linear approximation or those from Panofsky (1963). The reasoning for this conclusion is that the Dyer approximation sets $\alpha = 1/\phi_m$, where $\alpha = K_h/K_m$ is the inverse turbulent Prandtl number, while other calculations assumed α to be unity. Here K_h and K_m refer the heat and momentum eddy diffusivities, respectively. The Dyer and Panofsky formulations faired similarly in wind profiles, but the Dyer formulation produced more realistic temperature profiles. This is a direct result of Dyer allowing α to vary as a function of stability.

For water surfaces, surface roughness height must be separately considered from that over land, in which z_0 is defined from the land use category. With small capillary waves, the surface may be considered smooth and the Reynolds number is

approximated as $\mathrm{Re} = z_0 u_* / \nu \ll 1 \simeq 0.1$. Here, ν represents the kinematic molecular viscosity. The water surface is considered fully rough when $\mathrm{Re} \gg 1$. Here, the MM5 SL scheme implements a Charnock relation, which links the roughness length to friction velocity over water points:

$$z_0 = \frac{\alpha_c u_*^2}{g} \ , \tag{2.9}$$

where $\alpha_c = 0.14$ is the Charnock constant.

No thermal roughness length parameterization is included to address the flux consistency dilemma detailed in (2.6.1). A convective velocity accounting for the free convection regime following Beljaars (1994) is used to ensure non-vanishing surface fluxes of heat and moisture. This is needed because under free convection conditions, surface stresses approach zero and thusly so do surface fluxes. The convective velocity is simply a correction term added to the velocity, which guarantees a non-zero surface stress. The MM5 SL parameterization must be implemented juxtaposed with the Yonsei University (YSU) PBL scheme.

2.6.3 Janjic Parameterization

This SL scheme is also based on Monin and Obukhov (1954) similarity theory, with adjustments following Janjic (1994, 1996, 2002). The scheme assumes that turbulent fluxes are constant with height and that boundary conditions are to be prescribed at two levels, z_1 and z_2. After following a similar path described in the previous section, Janjic reaches a relation in the form

$$S_2 - S_1 = \left[\frac{F}{u_* \kappa} \right] \Phi_f, \tag{2.10}$$

where $S_{1,2}$ are prognostic variables at height $z_{1,2}$, F is the corresponding kinematic flux, κ is the von Kármán constant, and Φ_f is a function comprised of integral and stability functions. As an example, if $S = u$, and $F = \overline{w'u'}$, from (2.10)

$$u_2 - u_1 = \left[\frac{\overline{w'u'}}{u_* \kappa} \right] \Phi_m \ . \tag{2.11a}$$

The turbulence velocity scale, u_*, is often approximated as $(-\overline{w'u'}^{\frac{1}{2}})$, which leads to

$$u_2 - u_1 = \left(\frac{u_*}{\kappa}\right) \Phi_m. \tag{2.12a}$$

If z_1, z_2, u_1, u_2, and the Obukhov length L are known, both u_* and $\overline{w'u'}$ can be found. The issue is that L is generally unknown along with the fact that (2.10) is highly implicit. Accordingly, L is often times approximated as a function of $\mathrm{Ri_b}$, the bulk Richardson number, which approximates Ri by estimating local gradients through finite differences of meteorological variables across layers. An iterative approach is then employed to solve for the bulk exchange coefficients in which Janjic claims convergence with no more than three iterations, as a general rule. Over land however, the scheme replaced Φ_f stability functions with those from Dyer and Hicks (1970) and Paulson (1970). Under stable conditions, $\overline{w'\theta'_v}$ becomes very large and negative, meaning that L goes towards zero. An upper limit is placed on ζ to ensure that in such cases, surface fluxes are non-vanishing At the unstable regime, the Beljaars (1994) correction is applied to prevent the singularity in the case of an unstable SL with vanishing winds. In this case, L goes to zero due to the vanishing winds. The correction prevents such behavior by converting a fraction of the surface buoyancy flux to kinetic energy of the near-surface winds.

As stated previously, appreciation of the similarity theory requires specification of upper and lower boundary limits, $\zeta = z/L$ and $\zeta_0 = z_0/L$. The upper limit is taken at the first model level. It is assumed that the considered flow variables follow a logarithmic form as the lower boundary is approached and take their lower boundary values at the roughness height z_0.

The Janjic version of similarity theory states that the processes near the surface are not that straightforward. Within the thin layer of air next to the surface there is not enough space for turbulent eddies to develop such that molecular transport dominates. In reality, this molecular transport can significantly affect the surface

fluxes and thusly the PBL evolution. To account for this, an implicit viscous sub-layer following Zilitinkevich (1995) is employed over land and an explicit viscous sub-layer is implemented according to Janjic (1994) over water.

The Zilitinkevich (1995) method defines different roughness heights for different variables, possibly dependent on flow regimes. The basic concept in this method is to relate the roughness height for momentum to the roughness height for mass. For example, the equation for potential temperature in the SL may be given by $\theta(z) = \theta_0 + f(z_0)$. The problem is that in this case, θ_0 is not necessarily the surface value of potential temperature, but rather an integration constant. Thus the need to relate the two roughness heights. This method improves the surface flux representation not accounted for in the previous methods.

Over water, the Janjic (1994) method explicitly defines a viscous sub-layer. This method assumes that there are two distinct layers: a thin viscous sub-layer where vertical transports are only defined by molecular diffusion, and a turbulent layer on top of the sub-layer where vertical transports are only defined by turbulent fluxes. The method also assumes that the fluxes are continuous across these layers. A set of equations used to compute the height of the viscous sub-layer, along with fluxes at the sub-layer interface, allow for the lower boundary conditions to be taken at the computed heights as a weighted mean of the values at the surface and at the upper boundary. This viscous sub-layer over water is assumed to operate in three distinct regimes: smooth and transitional, rough, and rough with spray. When the Reynolds number reaches a prescribed threshold, the flow ceases to be smooth and the rough regime is entered. Here, the viscous sub-layer is turned off for momentum, but is left for moisture and heat. When the Reynolds number reaches another prescribed level, the regime is rough with spray and the whole viscous sub-layer collapses. In this regime, spray and breaking waves are assumed to provide a much more efficient method of exchange of heat and moisture between the water and air than could be

accomplished from molecular diffusion alone. This SL scheme must run in conjunction with the Mellor-Yamada (Janjic) PBL scheme.

2.6.4 Pleim Parameterization

It is noted in Pleim (2006) that two common approaches are used to overcome the consistency problem outlined in (2.6.1). The first approach is to define a separate thermal roughness height z_{0h} from the normal aerodynamic roughness height z_0. Basically, Eq. (2.5b) operates with z_{0h} instead of z_0. However, this method leads to complications since a new roughness height must be defined for each modeled quantity, including moisture and other chemical species. A second method is to define a quasi-laminar boundary layer (QLBL) resistance which adds to the turbulent aerodynamic resistance. To express θ_0 (θ at z_0) through the surface (skin) temperature θ_g, the following relationship is used.

$$\theta_* = \frac{(\theta_0 - \theta_g)}{u_*(R_a + R_b)} \ , \tag{2.13}$$

where R_a is the aerodynamic resistance accounting for turbulent diffusion, given by

$$R_a = \frac{1}{\kappa u_*}\left[\ln\left(\frac{z}{z_0}\right) - \psi_m\left(\zeta, \zeta_0\right)\right] \tag{2.14}$$

and R_b is the QLBL resistance accounting for molecular diffusion across a very thin QLBL abutting to the surface, given by

$$R_b = \frac{\mathrm{B}^{-1}}{u_*}\left(\frac{\mathrm{Sc}}{\mathrm{Pr}}\right)^{\frac{2}{3}} \ . \tag{2.15}$$

Here, $\mathrm{Sc} = \nu/D$ is the Schmidt number and D designates the molecular diffusivity of the scalar. The Prandtl number is given by $\mathrm{Pr} = \nu/\nu_\theta$, where ν_θ represents the molecular thermal diffusivity. The inverse Stanton number, denoted by B^{-1}, is a dimensionless heat transfer coefficient. Unlike the former approach, this method allows different quantities to be treated similarly given the appropriate definition of Sc based on diffusivity.

These approaches are combined for heat as

$$\ln\left(\frac{z_0}{z_{0h}}\right) = \kappa u_* R_b = \kappa \mathrm{B}^{-1} \ . \tag{2.16}$$

Based on empirical studies, $\kappa \mathrm{B}^{-1} = 2$ is treated as a constant over turbulent canopies. Solutions to Eqs. (2.3) - (2.16) are not possible without iteration, which is rather computationally expensive. To avoid this, a parameterization is employed where ζ is related to the bulk Richardson number, given by

$$\mathrm{Ri_b} = \frac{g z_1(\theta_1 - \theta_g)}{\theta_r(U_1^2 + V_1^2)} \ , \tag{2.17}$$

where indices denoted with subscript 1 refer to atmospheric variables at the lowest explicit model level.

The problem of analytically approximating the flux-profile relations is broken into two flow regimes: stable and unstable. For the stable regime, Blackadar (1976) is followed and ζ is approximated from $\mathrm{Ri_b}$ as

$$\zeta = \ln\left(\frac{z}{z_0}\right) \frac{\mathrm{Ri_b}}{1 - \frac{\mathrm{Ri_b}}{\mathrm{Ri_{crit}}}} \ , \tag{2.18}$$

where $\mathrm{Ri_{crit}} = 0.25$ is the critical Richardson number. It is deemed *critical* because it is below this value that the flow is assumed to be dynamically unstable and turbulent. The approximated ζ is implemented with the linear ψ functions offered by Webb (1970) and Dyer and Hicks (1970):

$$\psi_{(m,h)} = -\beta_{(m,h)}\zeta \ . \tag{2.19}$$

Linear functions fit experimental data well for moderately stable conditions ($0 < \zeta < 0.5$), however, underestimated fluxes exist under stronger stable conditions. It is offered that the slope of such functions should flatten in the range of $0.5 < \zeta < 1.0$. A simpler solution implements Eq. (2.19) for $0 < \zeta < 1.0$ and a reduced slope linear function at higher stabilities, where

$$\psi_{(m,h)} = 1 - \beta_{(m,h)}\zeta \ , \quad \text{for} \ \ \zeta > 1. \tag{2.20}$$

Eq. (2.18) must account for the reduced slope and is thusly written, when $\mathrm{Ri_b} > \mathrm{Ri_{cut}}$, as

$$\zeta = \ln\left(\frac{z}{z_0}\right) \frac{\mathrm{Ri_b}}{1 - \frac{\mathrm{Ri_{cut}}}{\mathrm{Ri_{crit}}}} \ , \tag{2.21}$$

where

$$\mathrm{Ri_{cut}} = \left[\ln\left(\frac{z}{z_0}\right) + \frac{1}{\mathrm{Ri_{crit}}}\right]^{-1} \ , \tag{2.22}$$

which is the solution of $\mathrm{Ri_b}$ when $\zeta =$ unity in Eq. (2.18).

Many complications arise within the unstable flow regime. Generally, a simple linear function of $\mathrm{Ri_b}$ is used to estimate ζ. However, the inclusion of the QLBL results in a more nonlinear relationship, which is amplified at greater roughness heights and faster wind speeds. Additionally, the functions are elaborate and computationally expensive. Previous studies used one empirical formula for ζ and another one for ψ. Here, a single empirical formulation is utilized to directly relate ψ to $\mathrm{Ri_b}$:

$$\psi_{h,m} = a_{h,m} \ln\left\{1 - b_{h,m}\left[\ln\left(\frac{z}{z_0}\right)\right]^{\frac{1}{2}} \mathrm{Ri_b}\right\} \ , \tag{2.23}$$

where

$$a_{h,m} = c_{h,m} + d_{h,m} \ln\left[\ln\left(\frac{z}{z_0}\right)\right] \ . \tag{2.24}$$

Empirically derived values yield $b_h = 15.7$, $b_m = 13.0$, $c_h = 0.04$, $c_m = 0.031$, $d_h = 0.355$, and $d_m = 0.276$. The QLBL R_b is used and defined by Eq. (2.15). In this case, R_b is analogous to $z_0/z_{0h} = 7.4$.

To summarize, the analytical approximation of the flux-gradient relationships in this scheme is achieved by estimating the ψ functions based on the bulk Richardson number without iteration. This method has different stable and unstable parts. Under stable flow characteristics, ζ is approximated following Eq. (2.18) for $0 < \zeta < 1$ and Eqs. (2.21) and (2.22) for $\zeta > 1$. Next, $\psi(\zeta)$ is evaluated from either Eq. (2.19) or Eq. (2.20), depending on the measure of stability. In unstable flow regimes, estimations of the ψ functions are made directly from $\mathrm{Ri_b}$ as stipulated in Eqs. (2.23) and (2.24). Finally, in both cases, momentum and heat fluxes are determined following Eqs. (2.4), (2.5), (2.13), (2.14), and (2.15).

2.7 Planetary Boundary Layer Schemes

The PBL scheme is responsible for vertical sub-grid fluxes due to eddy transports in the whole atmospheric column, not just within the boundary layer. This means that explicit vertical diffusion is de-activated with the assumption that the PBL scheme will handle such processes. The PBL scheme does not calculate horizontal diffusion, thus an additional computational scheme must be chosen to handle these processes. The most appropriate horizontal diffusion choices are those based on horizontal deformation or with a constant horizontal eddy diffusivity. The schemes are one-dimensional and assume that there is a clear separation of scales between sub-grid eddies and resolved eddies. Most PBL schemes consider dry mixing, but can also include saturation effects in the vertical stability that determines the mixing. The surface fluxes are provided by the SL and LSM schemes. The PBL scheme then determines the flux profiles within the well-mixed boundary layer and the stable layer. Thus, the PBL schemes provide atmospheric tendencies of temperature, moisture (including clouds), and horizontal momentum in the entire model column.

2.7.1 Yonsei University Parameterization

Hong et al. (2006) proposed a next generation PBL scheme to that in the Medium Range Forecast (MRF) model. This scheme is called the YSU scheme, named so because of its development at Yonsei University. Given are the algorithms for both mixed-layer diffusion and for free-atmosphere diffusion.

For the mixed-layer ($z \leq h$), where $h =$ the boundary layer depth, the turbulence diffusion equation for any prognostic variable, a, is given by

$$\frac{\partial a}{\partial t} = \frac{\partial}{\partial z}\left[K_a\left(\frac{\partial a}{\partial z} - \gamma_a\right) - \overline{(w'a')}_h\left(\frac{z}{h}\right)^3\right], \tag{2.25}$$

where K_a is the associated eddy diffusivity, γ_a is the counter-gradient correction term, which incorporates the contribution of the large scale eddies to the total flux, and

$\overline{(w'a')}_h$ is the flux at the inversion layer. This scheme is identical to the MRF scheme except that it now includes an asymptotic entrainment flux term at the inversion layer, $\overline{(w'a')}_h \left(\frac{z}{h}\right)^3$. In the MRF scheme, h was defined as the level at which boundary layer turbulent mixing diminishes. The MRF scheme implicitly parameterized these entrainment processes by raising h above the minimum flux level. The YSU scheme,however, explicitly treats the entrainment processes through the second term in (2.25). Thus, in the YSU scheme, h is defined as the level in which minimum flux exists at the inversion level.

The momentum diffusivity coefficient is given by

$$K_m = \kappa w_s z \left(1 - \frac{z}{h}\right)^p, \tag{2.26}$$

where p is the profile shape exponent, taken as 2, κ is the von Kármán constant, z is the height above the surface, h is the depth of the boundary layer, and w_s is the mixed layer velocity scale. The counter-gradient term, γ_a, is taken as

$$\gamma_a = b\frac{\overline{(w'a')}_0}{w_{s0}h}, \tag{2.27}$$

where $\overline{(w'a')}_0$ is the corresponding surface flux, b is a coefficient of proportionality, and $w_{s0}h$ is the mixed-layer velocity scale defined as the velocity of w_s in (2.26) at $z = 0.5h$.

To ensure compatibility between the SL top and bottom of the boundary layer, the YSU scheme employs the same Dyer and Hicks (1970) functions as employed in the MM5 similarity theory. The entrainment flux is taken to be -0.15 times the surface flux of buoyancy. Given this buoyancy flux at the inversion layer, the flux at the inversion layer for prognostic variables is proportional to the jump of each variable across the inversion layer. Thus, the fluxes are a function of the entrainment rate. Again, h is determined as the first neutral level by checking the stability between the lowest model level and levels above. K_m is ultimately found with h, w_{s0}, the entrainment fluxes, Pr, and the counter-gradient correction term.

In the free atmosphere, YSU utilizes a local diffusion scheme, or the so-called local-K approach. Local-K theory is a method for parameterizing the effects of turbulent mixing based on how small eddies will mix quantities along a local gradient of the transported quantity. The YSU scheme also defines an entrainment zone in which penetration of the entrainment flux above h is considered along with the local-K approach. Above this entrainment zone, the local-K method is considered alone.

Momentum and mass fluxes within the entrainment zone are defined as function of δ^{-1}, where δ is the entrainment zone depth. This depth can be approximated by

$$\frac{\delta}{h} = d_1 + d_2 \mathrm{Ri}^{-1}, \tag{2.28}$$

where constant are set as $d_1 = 0.2$ and $d_2 = 0.5$. Hong et al. (2006) showed that the scheme is independent of δ.

After the entrainment diffusivities are calculated, the diffusivities from local-K theory are computed using the gradient Richardson number, Ri, which is a function of momentum and mass fluxes. The computed Ri is bounded to -100 to prevent unrealistically unstable regimes. Stability functions are found for both unstable and stable regimes, expressed in terms of Ri. Once the local-K theory diffusivities are calculated, the total diffusivities for the entrainment zone is found by taking the geometric mean of K_{ent}, the entrainment diffusivities and K_{loc}, the local-K diffusivities. Above the entrainment zone, only the local-K theory applies, or in other words, $K = K_{loc}$. A small background diffusion is introduced (.001 times the vertical grid length) so that the vertical eddy diffusivity, K_v, is bounded by this and $1000\mathrm{m}^2\mathrm{s}^{-1}$. Now the diffusion equations for all prognostic variables are solved by an implicit numerical method.

2.7.2 Mellor-Yamada-Janjic Parameterization

Janjic (2002) implements a non-singular version of the Mellor and Yamada (1982) level 2.5 closure scheme. Problems have become apparent in the original version of

the closure scheme which this scheme attempted to address. One main problem was the singularity problem in a convective PBL with growing turbulence.

The turbulence kinetic energy, TKE, production and dissipation term in the Mellor and Yamada (1982) scheme can be expressed as

$$l\frac{d\left(\frac{1}{q}\right)}{dt} = \frac{\alpha\left(\frac{l}{q}\right)^4 + \beta\left(\frac{l}{q}\right)^2}{\gamma\left(\frac{l}{q}\right)^4 + \delta\left(\frac{l}{q}\right)^2 + 1} - \frac{1}{B_1}, \tag{2.29}$$

where l is the master length scale, q is the square-root of twice the TKE, and B_1 is a constant. The coefficients denoted by Greek letters only depend on buoyancy and shear of large scale flow. In the case of growing turbulence in a convective PBL, (2.29) has a singularity for

$$\gamma\left(\frac{l}{q}\right)^4 + \delta\left(\frac{l}{q}\right)^2 + 1 = 0. \tag{2.30}$$

Solving (2.30) yields the criterion for avoiding the singularity, given by

$$l < \sqrt{\frac{1}{p_1}}q, \tag{2.31}$$

where p_1 is the relevant root from (2.30).

In the stable regime, an upper limit is imposed on l which states that the ratio $\overline{ww}$/TKE cannot be smaller than that corresponding to the regime of vanishing turbulence. This requirement leads to

$$l < \sqrt{\frac{1}{t_1}}q, \tag{2.32}$$

where t_1 is the relevant root of the bi-quadratic equation. Combining (2.31) and (2.32) yields a unified criterion defined for the entire stability range, given by

$$l < f(B, S)q. \tag{2.33}$$

Note that in (2.33), f is a function of buoyancy and shear parameters B and S, depending only on large scale flow.

When implemented, l is first computed from diagnostic equations and then is adjusted to satisfy (2.33). Once the master length scale is determined, the contribution of production and dissipation are added to the TKE. This is done iteratively with convergence reached after approximately two iterations. The diffusion coefficients are computed using the updated TKE, but without re-computation of l. The vertical diffusion of TKE is taken after the computation of the turbulent exchange coefficients. Due to the linearization of the production/dissipation equation and the iterative nature, roughly the same parameters determine the TKE production/dissipation and vertical diffusion of the large scale variables. The fast convergence of solving the TKE equation makes this a non-issue. The boundary layer depth is defined as the lowest model level above the surface at which the equilibrium turbulent energy becomes negative, or in other words, as the height of the lowest model level at which TKE approaches its prescribed lower bound.

2.7.3 Asymmetrical Convective Model Parameterization

Pleim (2007) offers a revised version of the original asymmetrical convective model (ACM1) described by Pleim and Chang (1992). The ACM1 model represents non-local fluxes through a transilient matrix, which defined the mass flux between any two model layers, given by

$$\frac{\partial \theta_i}{\partial t} = \sum_j M_{ij}\theta_j \ , \tag{2.34}$$

where M_{ij} is the transilient matrix containing the mixing coefficients between model layers i and j. The ACM1 follows Blackadar (1978), which stipulates that convective transport begins at the lowest model layer, representing the atmospheric surface layer, and rising directly to all remaining layers in the convective boundary layer (CBL) with symmetrical return flow from each layer to the lowest model layer. The ACM1 modified this scheme by replacing the symmetrical return flow with an asymmetrical downward transport.

It is noted in Pleim (2007) that a main drawback of ACM1 is the lack of local upward diffusion, which results in an unrealistic step-function between the first two model layers. To correct this, an eddy diffusion component of non-local transport is added to the newly proposed asymmetrical convective model: version 2 (ACM2). The result is a better representation of flux-profile shapes, namely in regards to a steadily decreasing gradient near the surface. This allows ACM2 to similarly represent the potential temperature profile to that of eddy diffusion schemes. However, local and non-local fluxes are explicitly designated, meaning that ACM2 is more germane to other quantities, such as wind or humidity. The paramount tactic of ACM2 is to match the ACM1 and eddy diffusion schemes at the top of the lowest model layer and to allocate the mixing rate of each scheme such that the resultant flux at that level is undifferentiated from either scheme alone. For successful implementation, high vertical grid spacing is required, such that the first model level is contained within the surface layer.

Discrete model equations are presented on a vertically staggered grid in which scalar quantities and horizontal momentum components are centrally located within each layer, denoted by the subscript i. Conversely, eddy diffusivities and vertical fluxes and velocities are established on the layer interfaces $(i + 1/2)$. Combining the ACM1 non-local scheme (Pleim and Chang 1992) with eddy diffusion yields the governing equation of ACM2, which for any scalar C_i (mass mixing ratio) in model layer i is given by

$$\begin{aligned} \frac{\partial C_i}{\partial t} &= M2uC_1 - M2d_iC_i + M2d_{i+1}C_{i+1}\frac{\Delta z_{i+1}}{\Delta z_i} \\ &+ \frac{1}{\Delta z_i}\left[\frac{K_{i+\frac{1}{2}}(C_{i+1} - C_i)}{\Delta z_{i+\frac{1}{2}}} + \frac{K_{i-\frac{1}{2}}(C_i - C_{i-1})}{\Delta z_{i-\frac{1}{2}}}\right], \end{aligned} \tag{2.35}$$

where C_i is the mixing ratio in layer 1 (lowest model layer), and Δz_i is the thickness of layer i. Here, $M2u$ and $M2d$ replace the ACM1 upward convective mixing rate (Mu) and downward mixing rate from layer i to layer $i-1$ (Md_i), where

$$Mu = \frac{K_h(z_{1+\frac{1}{2}})}{\Delta z_{1+\frac{1}{2}}(h - z_{1+\frac{1}{2}})} \quad \text{and} \tag{2.36}$$

$$Md_i = \frac{Mu(h - z_{i-\frac{1}{2}})}{\Delta z_I} \ , \tag{2.37}$$

with h representing the depth of the PBL. Due to the split of total mixing into local and non-local elements by a weighting factor f_{conv}, the new mixing rate and eddy diffusivity are defined as

$$M2u = \frac{f_{conv} K_h(z_{1+\frac{1}{2}})}{\Delta z_{1+\frac{1}{2}}(h - z_{1+\frac{1}{2}})} = f_{conv} Mu \quad \text{and} \tag{2.38a}$$

$$K(z) = K_{m,h}(z)(1 - f_{conv}) \ . \tag{2.38b}$$

Vertical eddy diffusivity $K_{h,m}$ is defined following Holtslag and Boville (1993) as

$$K_{m,h}(z) = \kappa \frac{u_*}{\phi_{m,h}\left(\frac{z_s}{L}\right)} z \left(1 - \frac{z}{h}\right)^2 \ , \tag{2.39}$$

where under stable conditions ($z_s < 0$), $z_s = \min(z, 0.1h)$, and for stable conditions, $z_s = z$. The profile functions under unstable conditions follow that of Dyer and Hicks (1970) as defined by Eq. (2.7).

The essential parameter dictating the proportion of local versus non-local mixing is f_{conv}. For stable or neutral conditions, $f_{conv} = 0$ and the ACM2 scheme defaults to pure eddy diffusion. Once the breadth of convective eddies exceed that of the vertical grid spacing, f_{conv} is allowed to vary from 0 to 1 (ACM1 scheme). Pleim (2007) derives an expression for f_{conv} by taking the ratio of non-local flux to the total flux, yielding

$$f_{conv} = \left[1 + \frac{\kappa^{-\frac{2}{3}}}{0.1a}\left(-\frac{h}{L}\right)^{-\frac{2}{3}}\right]^{-1} \ , \tag{2.40}$$

where a is empirically set to 7.2. Results indicate that as flow features slowly transition from stable and neutral conditions to proliferated instabilities, f_{conv} levels off at a value of 0.5.

When comparing ACM2 with other non-local schemes, such as the Yonsei University scheme (YSU), the eddy diffusion terms are the same while the traditional counter-gradient term ($K_h\gamma_h$) as prescribed in Eq.(2.25) is replaced with the transilient terms involving non-local mixing rates $M2u$ and $M2d$. Herein lies the main difference between ACM2 and other schemes. Parameterizations using the traditional counter-gradient term simply adjusts the local potential temperature gradient to account for surface heat flux driven by large-scale convection. These schemes work well where the surface heat flux is not only the driver of the convective turbulence, but is also the source of the transported quantity. However, the surface heat flux is replaced by the flux of the considered quantity in γ_h as defined in Holtslag and Boville (1993), meaning that non-local effects are proportional to surface flux. In this case, the respective surface flux may be driven by processes unrelated to convective turbulence. Conversely, the ACM2 scheme provides a representation of vertical transport by detraining convective plumes that applies to any modeled quantity.

The depth of the PBL is determined from, R_{crit} for stable conditions as the height where

$$\mathrm{Ri_b} = \left[\frac{\theta_r U(h)^2}{g[\theta_v(h) - \theta_v(z_1)]}\right]^{-1} = \mathrm{Ri_{crit}} \ , \tag{2.41}$$

where z_1 is the height of the lowest model level, θ_v is the virtual potential temperature, θ_r is some reference potential temperature, and $\mathrm{Ri_{crit}} = 0.25$. For unstable conditions, the height of the convectively unstable layer (z_{mix}) is found as the height at which $\theta_v(z_{mix}) = \theta_s$, where

$$\theta_s = \theta_v(z_1) + b\frac{\overline{w'\theta'_{v0}}}{w_m} \ ,$$

where $w_m = u_*/\phi_m$ is the convective velocity scale and b is empirically set to 8.5 as prescribed by Holtslag and Boville (1993). The boundary layer depth is then found as the height where the bulk Richardson number surpasses the critical value, such that the bulk Richardson number is defined for the entrainment zone above z_{mix} as

$$\mathrm{Ri_b} = \frac{g[\theta(h) - \theta_s](h - z_{mix})}{\overline{\theta_v}[U(h) - U(z_{mix})]^2} \ . \tag{2.42}$$

2.8 Explicit Spatial Diffusion

Two formulations for spatial dissipation exist in the ARW physics solver. The first is diffusion along coordinate surfaces and the other is diffusion in physical space (x, y, z). The diffusion operators for these formulations are described here.

2.8.1 Diffusion Along Coordinate Surfaces

For any variable, a, the horizontal and vertical second order spatial filtering can be expressed as

$$\begin{aligned} \partial_t(\mu_d a) &= \ldots + \mu_d[m\partial_x(mK_h\partial_x a) + m\partial_y(mK_h\partial_y a)] \\ &+ g^2(\mu_d\alpha)^{-1}\partial_\eta(K_v\alpha^{-1}\partial_\eta a) \ , \end{aligned} \tag{2.43}$$

where μ_d is the dry hydrostatic pressure difference between the surface and model top, m is the mapscale factor, K_h, K_v are the horizontal and vertical eddy viscosities, g is the acceleration due to gravity, and α is the inverse density of air.

For the horizontal and vertical momentum equations, (2.43) is spatially discretized as

$$\begin{aligned} \delta_t U = \ldots &+ \overline{\mu_d}^x\overline{m}^x[\delta_x(mK_h\delta_x u) + \delta_y(\overline{m}^{xy}\overline{K_h}^{xy}\delta_y u)] \\ &+ g^2(\overline{\mu_d}^x\overline{\alpha}^x)^{-1}\delta_\eta(K_v(\overline{\alpha}^{x\eta})^{-1}\delta_\eta u) \\ \delta_t V = \ldots &+ \overline{\mu_d}^y\overline{m}^y[\delta_x(\overline{m}^{xy}\overline{K_h}^{xy}\delta_x v) + \delta_y(mK_h\delta_y v)] \qquad (2.44a) \\ &+ g^2(\overline{\mu_d}^y\overline{\alpha}^y)^{-1}\delta_\eta(K_v(\overline{\alpha}^{y\eta})^{-1}\delta_\eta v) \\ \delta_t W = \ldots &+ \mu_d m[\delta_x(\overline{m}^x\overline{K_h}^{x\eta}\delta_x w) + \delta_y(\overline{m}^y\overline{K_h}^{y\eta}\delta_y w)] \qquad (2.44b) \\ &+ g^2(\mu_d\overline{\alpha}^\eta)^{-1}\delta_\eta(K_v i\alpha^{-1})\delta_\eta w) \ , \end{aligned}$$

where $\overline{()}^{x,y}$ is a linear interpolation operator, $\overline{()}^{\eta}$ is a vertical interpolation operator, $\overline{()}^{xy} = \overline{\overline{()}^x}^y$ (with similar forms for $\overline{()}^{x\eta}$ and $\overline{()}^{y\eta}$), and $\delta_{x,y,\eta}$ is a discrete operator.

Discretization for scalar fields is of similar form, but K_h is multiplied by Pr^{-1}. In (2.44), K_h is allowed to vary in space, whereas K_v does not. This means that there is no reason to for spatial averaging of K_v.

2.8.2 Diffusion in Physical Space

In the physical space formulation, the geometric height coordinate is employed. The coordinate metrics are computed from the prognostic geopotential and are given by

$$z_x = g^{-1}\delta_x\phi \ , \ z_y = g^{-1}\delta_y\phi \ .$$

The metric terms are defined on w levels and (z_x, z_y) are horizontally coincident with (u, v) points. The vertical diffusion terms are computed directly in terms of geometric height, such that no vertical coordinate metrics are needed.

The continuous equations for evaluating diffusion in physical space are given by

$$\partial_t U = ... \ - m[\partial_x\tau_{11} + \partial_y\tau_{12} - \partial_z(z_x\tau_{11} + z_y\tau_{12})] - \partial_z\tau_{13} \tag{2.45a}$$

$$\partial_t V = ... \ - m[\partial_x\tau_{12} + \partial_y\tau_{22} - \partial_z(z_x\tau_{12} + z_y\tau_{22})] - \partial_z\tau_{23} \tag{2.45b}$$

$$\partial_t W = ... \ - m[\partial_x\tau_{13} + \partial_y\tau_{23} - \partial_z(z_x\tau_{13} + z_y\tau_{23})] - \partial_z\tau_{33} \ , \tag{2.45c}$$

where τ_{ij} is the velocity stress tensor.

For the horizontal and vertical momentum equations, (2.45) is spatially discretized as

$$\delta_t U = ... \ - \overline{m}^x[\delta_x\tau_{11} + \delta_y\tau_{12} - \delta_z(z_x\overline{\tau_{11}}^{x\eta} + \overline{z_y}^{xy}\overline{\tau_{12}}^{y\eta})] - \delta_z\tau_{13} \tag{2.46a}$$

$$\delta_t V = ... \ - \overline{m}^y[\delta_y\tau_{22} + \delta_x\tau_{12} - \delta_z(z_y\overline{\tau_{22}}^{y\eta} + \overline{z_x}^{xy}\overline{\tau_{12}}^{x\eta})] - \delta_z\tau_{23} \tag{2.46b}$$

$$\delta_t W = ... \ - m[\delta_x\tau_{13} + \delta_y\tau_{23} - \delta_z(\overline{z_x}^{x\eta}\overline{\tau_{13}}^{x\eta} + \overline{z_y}^{x\eta}\overline{\tau_{23}}^{y\eta})] - \delta_z\tau_{33} \ , \tag{2.46c}$$

where the discretization for scalars is of similar form.

2.9 Turbulent Mixing

As stated in section (2.7), the PBL scheme handles the vertical diffusion when implemented, meaning that any other vertical diffusion calculations within the model are turned off. Accordingly, horizontal diffusion must be calculated externally to the PBL scheme. In this case there exists two methods to calculate horizontal diffusion; prescribing constant eddy diffusivities or employing a two-dimensional Smagorinsky closure. Alternatively, if no PBL scheme is used, one must prescribe both vertical and horizontal diffusion. In this case, the WRF model provides three turbulent mixing options to handle vertical diffusion in addition to horizontal diffusion; constant eddy diffusivities, three-dimensional Smagorinsky closure, and the 1.5-order prognostic TKE closure.

2.9.1 Constant Eddy Diffusivity Scheme

Constant K_h and K_v can be specified at runtime in the WRF model. Setting both diffusivities to a constant value only makes sense when no PBL scheme is called. If a PBL scheme is implemented, then the user may set K_h alone to a constant value. In this study, setting an arbitrary constant value to these diffusivities made little physical sense, and was subsequently omitted.

2.9.2 Two-Dimensional Smagorinsky Scheme

In this option, K_h is determined from the horizontal deformation using a Smagorinsky (1963) first-order closure approach. According to this formulation, the eddy viscosity is defined and discretized as

$$K_h = C_s^2 l^2 [0.25(D_{11} - D_{22})^2 + \overline{D_{12}^2}^{xy}]^{\frac{1}{2}}, \tag{2.47}$$

where D_{11} and D_{22} are deformation tensors, the length scale $l = (\Delta x \Delta y)^{\frac{1}{2}}$, and C_s is a constant with a typical value of $C_s = 0.25$. For scalar mixing, the eddy viscosity is

divided by the turbulent Prandtl number that typically has a value of $\frac{1}{3}$ (Deardorff 1972). The only implementation of this scheme that makes sense is alongside a PBL parameterization scheme.

2.9.3 Three-Dimensional Smagorinsky Scheme

Both K_h and K_v can be determined using a Smagorinsky (1963) three-dimensional turbulence closure approach. The eddy viscosities are defined as

$$K_{h,v} = C_S^2 l_{h,v}^2 max[0, (D^2 - \mathrm{Pr}^{-1} N^2)^{\frac{1}{2}}] \ , \tag{2.48}$$

where

$$D^2 = \frac{1}{2}[D_{11}^2 + D_{22}^2 + D_{33}^2] + (\overline{D_{12}}^{xy})^2 + (\overline{D_{13}}^{x\eta})^2 + (\overline{D_{23}}^{y\eta})^2 \ ,$$

and N is the Brunt-Väisälä frequency, which is calculated using either the formula for a moist saturated or unsaturated environment. For a moist saturated environment ($q_v \geq q_{vs}$ *or* $q_c \geq 0.01 \mathrm{gkg}^{-1}$)

$$N^2 = g\left[A\frac{\partial \theta_e}{\partial z} - \frac{\partial q_w}{\partial z}\right],$$

and for an unsaturated environment($q_v < q_{vs}$ *or* $q_c < 0.01 \mathrm{gkg}^{-1}$)

$$N^2 = g\left[\frac{1}{\theta}\frac{\partial \theta}{\partial z} + 1.61\frac{\partial q_v}{\partial z} - \frac{\partial q_w}{\partial z}\right] \ ,$$

where q_v represents the water vapor content, q_{vs} represents the saturation water vapor content, q_c represents the cloud water content, and q_w represents the total water and ice content. Additionally, θ_e is the equivalent potential temperature. q_c If Δx is less than the user-specified critical length scale, l_{cr}, then the length scale used in calculating K_h and K_v in (2.48) is $l_{h,v} = (\Delta x \Delta y \Delta z)^{\frac{1}{3}}$ (and $K_h = K_v = K$). Otherwise, the length scale $l_h = \sqrt{\Delta x \Delta y}$ in the calculation of K_h using (2.48), and $l_v = \Delta z$ for the calculation of K_v using (2.48). In addition, the eddy viscosities for scalar mixing are divided by the turbulent Prandtl number, $\mathrm{Pr} = \frac{1}{3}$.

This scheme is employed only if no PBL scheme is chosen. This method is considered LES mode since it is only realistic to do so with a horizontal grid spacing where boundary layer eddies may start to be resolved.

2.9.4 1.5-Order Prognostic TKE Scheme

Here, the eddy viscosities are computed using

$$K_{h,v} = C_k l_{h,v} \sqrt{e} \tag{2.49}$$

where e is the TKE (a prognostic variable in this scheme), C_k is a constant (typically $0.15 < C_k < 0.25$), and l is a length scale. The prognostic equation governing the evolution of TKE, e is

$$\begin{aligned} \partial(\mu_d e) + (\vec{\nabla} \cdot \vec{V_e})_\eta = \mu_d (&shear\ production \\ &+ buoyancy\ +\ dissipation). \end{aligned} \tag{2.50}$$

The time derivative and transports terms in (2.50) are integrated in the same manner as other scalars. The sink and source terms for e are given as, for shear production

$$\begin{aligned} shear\ production = K_h D_{11}^2 + K_h D_{22}^2 + K_v D_{33}^2 \\ + K_h \overline{D_{12}^2}^{xy} + K_v \overline{D_{13}^2}^{x\eta} + \overline{K_v D_{23}^2}^{y\eta}, \end{aligned} \tag{2.51}$$

$$buoyancy = -K_v N^2, \tag{2.52}$$

where N is calculated as in (2.9.3), and

$$dissipation = -\frac{C e^{\frac{3}{2}}}{l}. \tag{2.53}$$

where C is a constant based on mixing length.

This scheme follows with the three-dimensional Smagorinsky approach in that it is only employed when no PBL scheme is used, or in the so-called LES mode.

2.10 Physics Interactions

There are many complicated interactions in the WRF model ARW physics solver. Offered is a quick summary describing these interactions. The microphysics scheme provides precipitation forcing and updates to the atmospheric temperature and moisture states, the cumulus convection scheme produces vertical heating and moisture profiles, the atmospheric radiation scheme offers radiative fluxes, while the surface layer scheme provides friction velocities and exchange coefficients. The LSM ingests the precipitation forcing from the microphysics and cumulus convection schemes, the radiative forcing from the atmospheric radiation schemes, and the information from the surface layer, along with internal knowledge of the land's state variables and land-surface properties, to produce surface heat and moisture fluxes above land and ice points. The PBL takes in the info from the surface layer scheme to calculate the surface stress. The surface heat and moisture fluxes from the LSM acts as a lower boundary condition for the vertical diffusion in the PBL. The PBL then produces sub-grid fluxes due to eddy transports in the entire atmosphere, not just the boundary layer. The PBL scheme provides tendencies for temperature, moisture, and horizontal momentum. Turbulent mixing schemes are then implemented to handle horizontal diffusion. Figure (2.1) depicts the direct physics interactions within the WRF model.

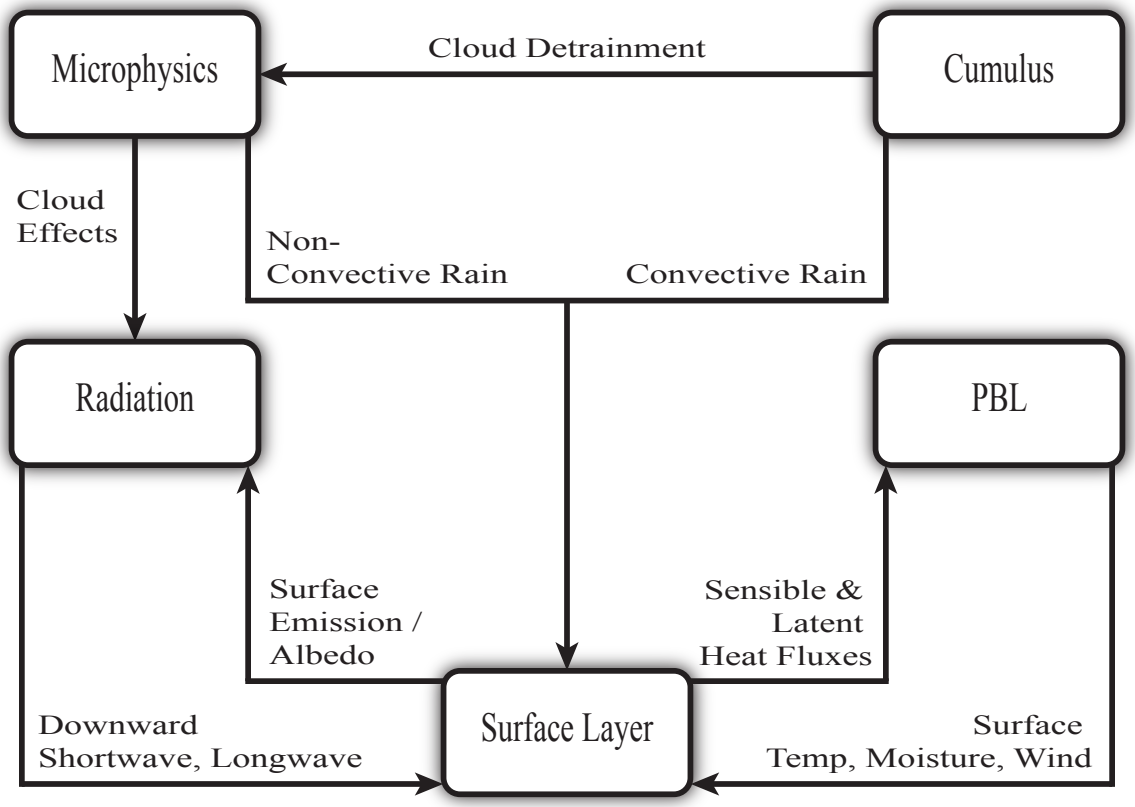

Figure 2.1: Direct interactions of physical parameterizations in the WRF model. The LSM and SL schemes are within the *Surface Layer* heading. Adapted from Dudhia (2008)

Chapter 3

Model Run Arrangements

As mentioned in Chapter (1), this thesis assesses a limited and sensible subset of TTSI physical parameterization schemes. This chapter provides an overview of those configurations along with details of the comparison domain, the method of prescribing lateral boundary conditions (LBC), and the process for finding stable model solutions.

3.1 Lateral Boundary Conditions

The WRF model generates a file containing the lateral boundary conditions (LBC) for times in which the model receives analyses from the North American Regional Reanalysis (NARR) data-set. The NARR data-set is located on a grid with 32km uniform horizontal grid spacing. The WRF pre-processing system (WPS) interpolates that data to the domain of interest. In this study, LBC data were generated in 3h intervals. The LBC data contains information for $u, v, \theta, q_v, \phi^{'}$, and $\mu_d^{'}$, where u and v are the horizontal wind components, θ is potential temperature, q_v is water vapor mass concentration (specific humidity), $\phi^{'}$ is the perturbation of geopotential, and $\mu_d^{'}$ is the perturbation of the dry air column mass. Each variable is represented by both a current value for a given boundary time (the starting moment of the 3h interval) and a tendency toward its value three hours later. The LBC data for wind is stored in terms of the so-called coupled wind, in which horizontal velocity components are corrected for the map scale factor $\overline{m}$, and the dry air column mass μ_d. This correction is additionally supplemented by interpolating $\overline{m}$ and μ_d to the velocity component position on a staggered-grid cell.

For example, the 0h data for the x-component of wind in the LBC contains both the coupled u, that is

$$U_{0\mathrm{h}} = \frac{\overline{\mu}_d u}{\overline{m}}\Big|_{0\mathrm{h}} , \tag{3.1}$$

and a tendency value defined as

$$U_t = \frac{U_{3\mathrm{h}} - U_{0\mathrm{h}}}{3\mathrm{h}} , \tag{3.2}$$

which represents the evolution of the velocity field at a given grid point (cell) over the 3h interval between two moments when the model is supplied with the NARR data. Other meteorological variables are coupled (scaled) with μ_d only. For the $\mu_d^{'}$ field, coupling is not used.

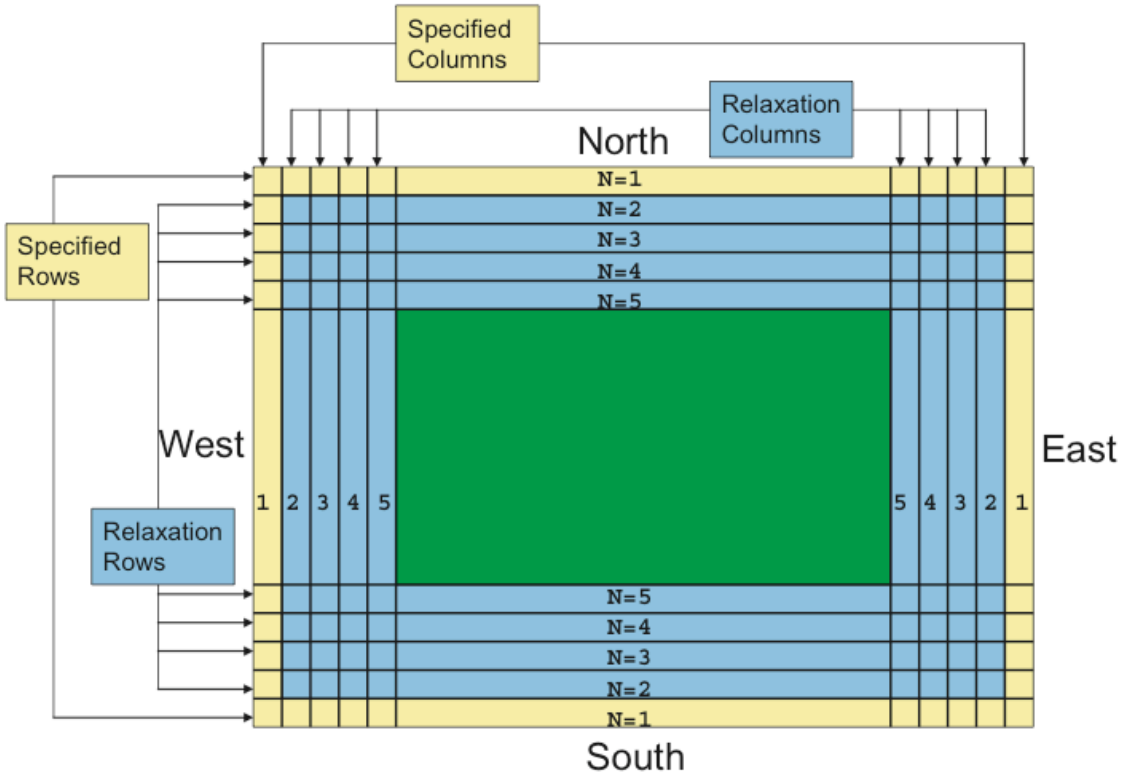

Figure 3.1: Specified and relaxation zones defined for typical WRF specified LBC.

The LBC constrain variability of meteorological fields in the vicinity of the domain boundaries and act to relax predicted values in the simulation domain toward large-scale exterior fields. This method of adjustment of mesoscale meteorological fields in the vicinity of domain boundaries is commonly referred to as the nudging or relaxation boundary condition (Skamarock et al. 2008). The LBC adjustment takes place in two domain areas (zones) adjacent to the boundaries, the so-called specified zone (SZ) and relaxation zone (RZ), schematically shown in Figure (3.1).

The default width of the SZ in terms of the number of column and rows involved is one, or in other words, the default SZ includes the outer rows/columns of the domain. Generally, the SZ width is run-time configurable and determined by the interval of time between two subsequent analyses ingestions. The RZ is the domain region in which the model is nudged towards the large-scale forecast. The RZ width is also run-time configurable with a default value of 4, or rows/columns two through five, as illustrated in Figure (3.1).

Let Ψ be any prognostic variable within the model that is represented in the LBC. Its evolution is described by the following equation from Davies and Turner (1977).

$$\frac{\Delta\Psi}{\Delta t} = F_1(\Psi_{LS} - \Psi) - F_2\Delta^2(\Psi_{LS} - \Psi) \ , \tag{3.3}$$

$$F_1 = \frac{1}{10\Delta t}\frac{SZ + RZ - n}{RZ - 1} \ , \tag{3.4}$$

$$F_2 = \frac{1}{50\Delta t}\frac{SZ + RZ - n}{RZ - 1}, \ , \tag{3.5}$$

where n is the number of grid points constrained by $(SZ + 1 \leq n \leq SZ + RZ - 1)$ as seen in Figure (3.1), Ψ_{LS} is the large-scale value of Ψ from the analyses fields, and Δ^2 is a 5-point horizontal smoother applied along η-surfaces. The weighting functions F_1 and F_2 are linear ramping functions with a maximum located at the first relaxation row or column nearest to the SZ. Microphysical variables, except water vapor, and all other scalars have flow-dependent boundary conditions applied in the SZ. Since

these boundary conditions require only information from the interior of the grid, the microphysical variables are not included in the LBC.

When defining a domain, one must carefully consider the appropriate number of grid points to implement. As stated before, the LBC comprise 5 rows/columns on each side of the model domain by default. The user must ensure that the LBC do not compose too great a percentage of the domain's total size. For example, if one were to choose a model domain in which the grid comprised 20×20 points in the horizontal, the LBC would constitute seventy-five percent of the total number of grid points. Such a scenario would likely yield unphysical representation of atmospheric flow features. While the acceptable percentage of LBC coverage is enigmatic, a model grid consisting of 100×100 points has shown adequate during this study, where the LBC extent is roughly twenty-one percent. It is not only important to consider the LBC fractional extent, but to also appraise where the physical area of interest lies within the domain and how that area is affected by the boundaries. In all cases here, the location of interest was centrally located, ensuring sufficient distance from the lateral boundaries.

3.2 Model Domain Specifications

The WRF model utilized a simulation domain of $100 \times 100\text{km}^2$ in the horizontal, extending to 100hPa in the vertical, or approximately 16km. Equations were solved on a $101 \times 101 \times 41$ staggered computational grid with horizontal grid spacing of $\Delta x = \Delta y = 1\text{km}$ and stretched grid in the vertical as discussed in (1.2). Figure (3.2) depicts the vertical model levels in relation to terrain in the lower portion of the WRF computational grid. The stretching of vertical levels by the terrain following, pressure normalized η-coordinate is clearly evident.

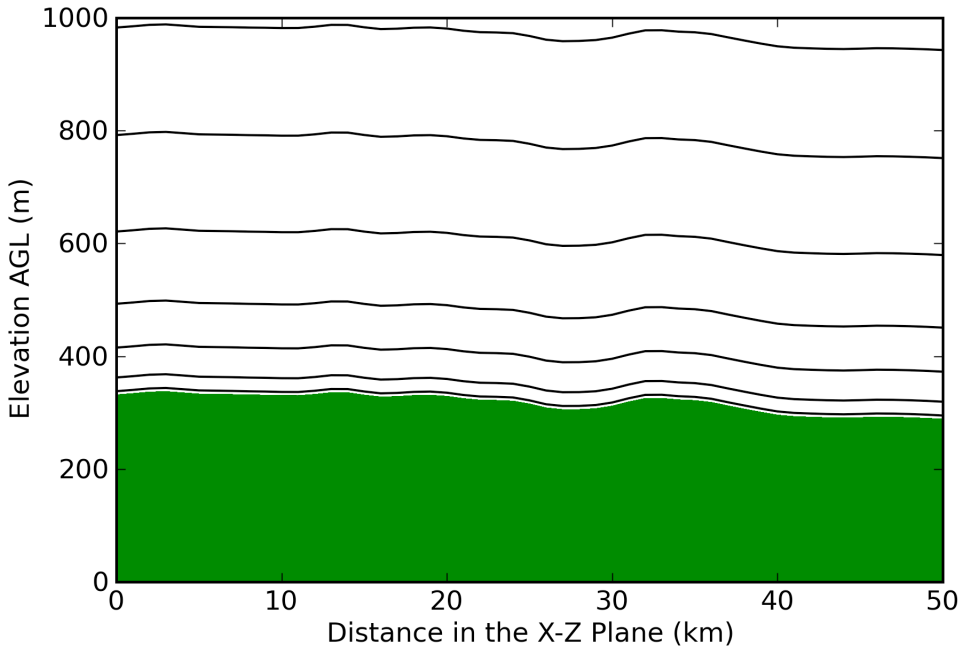

Figure 3.2: Vertical levels in the WRF model computational grid juxtaposed with geographic domain terrain elevation.

WRF model predictions were examined in part by comparison with fine-scale LES data. The LES employed a simulation domain of $51.2 \times 51.2 \times 4\text{km}^3$. Finite difference atmospheric equations were solved on a $512 \times 512 \times 80$ staggered computational grid with horizontal spacing of $\Delta x = \Delta y = 100\text{m}$ and vertical spacing of $\Delta z = 50\text{m}$. Although at the coarse end of LES applications, the simulation data is still considered "truth" since it directly computes quantities and processes considered sub-grid scale in WRF model calculations.

The LES and WRF model domains were similarly centered over the LMN ARM profiler site, located at 97.5° W, 36.6° N, as shown in Figure (3.3). The terrain in this geographic region is considered nearly uniform, with an approximate elevation of 310m above sea level (ASL) as represented in Figure (3.2). The LES domain was used for all comparison exercises. Figure (3.4) depicts the dominant land use distribution for the comparison domain. Descriptions of each category is given in Table (3.1).

Table 3.1: 24-Category USGS Land Use Properties

Code	**Category**	**Albedo**	**Emissivity**	$\mathbf{z_o}$ **(m)**
1	Urban and Built-Up Land	0.15	0.88	0.80
2	Dryland Cropland and Pasture	0.17	0.985	0.15
3	Irr. Cropland and Pasture	0.18	0.985	0.10
4	Dryland/Irr. Cropland/Pasture	0.18	0.985	0.15
5	Cropland/Grassland Mosaic	0.18	0.98	0.14
6	Cropland/Woodland Mosaic	0.16	0.985	0.20
7	Grassland	0.19	0.96	0.12
8	Shrubland	0.22	0.93	0.05
9	Shrubland/Grassland	0.20	0.95	0.06
10	Savanna	0.20	0.92	0.15
11	Deciduous Broadleaf Forest	0.16	0.93	0.50
12	Deciduous Needleleaf Forest	0.14	0.94	0.50
13	Evergreen Broadleaf Forest	0.12	0.95	0.50
14	Evergreen Needleleaf Forest	0.12	0.95	0.50
15	Mixed Forest	0.13	0.97	0.50
16	Water Bodies	0.80	0.98	0.0001
17	Herbaceous Wetland	0.14	0.95	0.20
18	Wooded Wetland	0.14	0.95	0.40
19	Barren or Sparsely Vegetated	0.25	0.90	0.10
20	Herbaceous Tundra	0.15	0.92	0.10
21	Wooded Tundra	0.15	0.93	0.30
22	Mixed Tundra	0.15	0.92	0.15
23	Bare Ground Tundra	0.25	0.90	0.10
24	Snow or Ice	0.55	0.95	0.05

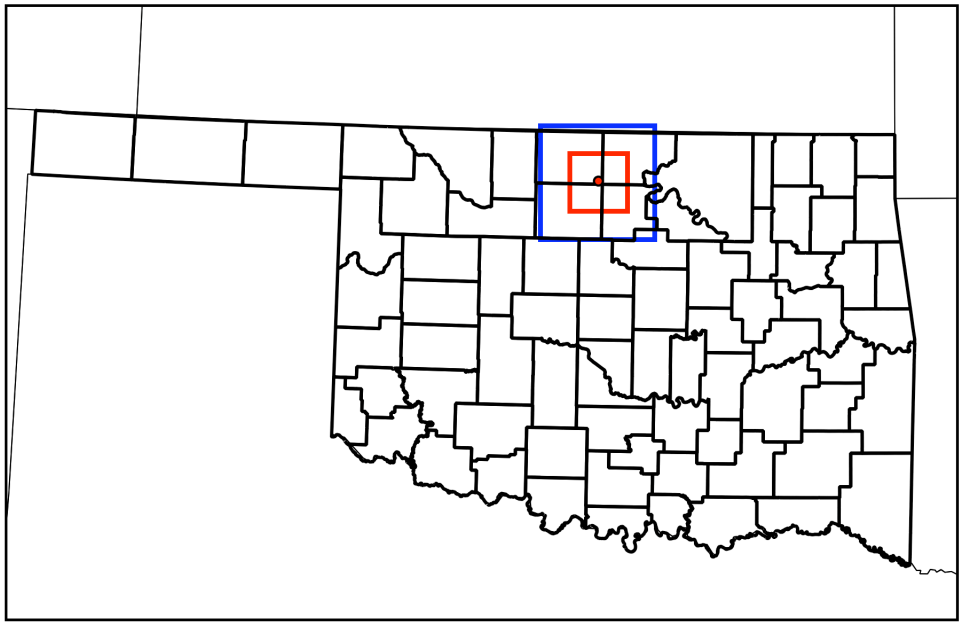

Figure 3.3: Locations of domains employed in the WRF model (blue) and LES (red). The red center point is the site of the LMN ARM profiler.

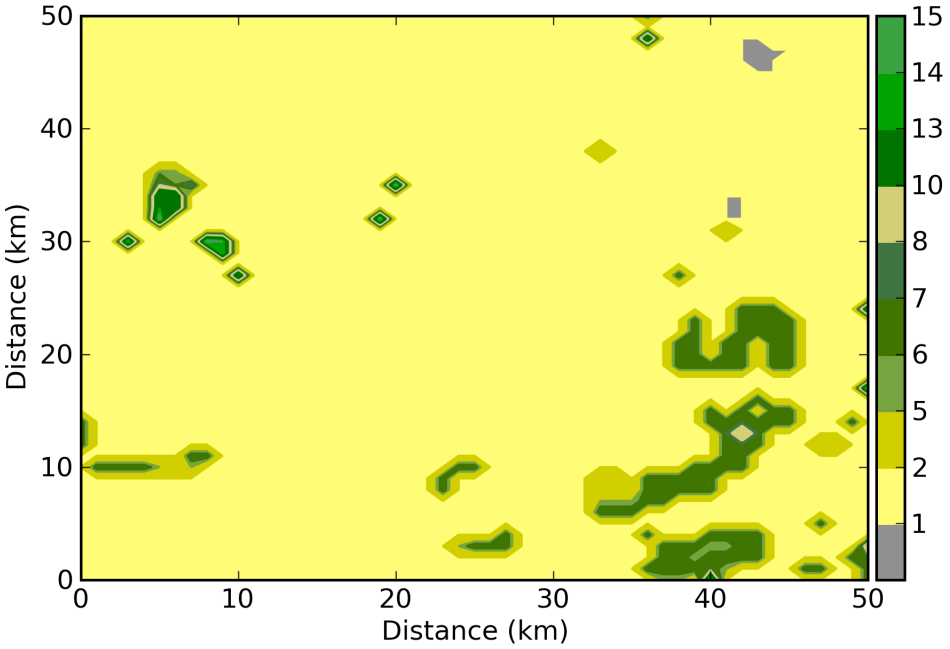

Figure 3.4: Land use distribution within the central comparison domain.

3.3 Model Configurations

As stated in Chapter (2), the WRF model offers physical parameterization schemes within seven categories: MP, CC, AR, LSM, SL, PBL, and turbulent mixing. The MP, CC, AR, and LSM were set constant for all model experiments. These baseline options include the WSM6 microphysics scheme, no cumulus parameterization, the RRTM longwave and Dudhia shortwave atmospheric radiation schemes, and the Noah land-surface model. The remaining categories are described as the TTSI parameterizations.

It is important to carefully select sensible combinations of TTSI schemes in order to investigate sensitivities of WRF model solutions. The SL and PBL parameterizations are tied to each other in the WRF model, meaning that three different combinations of these schemes exist. Since the PBL scheme acts to mix atmospheric quantities in the vertical, a two-dimensional horizontal turbulent mixing scheme is the only option that makes sense. There are two such types of turbulent mixing parameterizations; the stipulation of constant horizontal eddy diffusivity and the two-dimensional Smagorinsky closure scheme. Defining constant eddy diffusivity carries little physical sense, leaving the two-dimensional Smagorinsky closure as the only logical mixing scheme to combine when a PBL parameterization is implemented. For this configuration, there are two available combinations: calculating second-order diffusion either on model levels (coordinate space) or on terrain-following surfaces (physical space). When a PBL scheme is omitted and vertical mixing is explicitly calculated in all three dimensions, only two pertinent turbulence closures exist: the 1.5-order prognostic TKE or three-dimensional Smagorinsky closure schemes. Full three-dimensional mixing is only recommended when diffusion is calculated in physical space. Table (3.2) lists all applicable combinations of TTSI parameterizations used in this study. Abbreviations by which these configurations will be referred to from hereafter are also listed.

Table 3.2: TTSI Configurations for WRF model runs

SL/PBL	Diffusion	Turbulence	Abbrev
MM5/YSU	Coordinate	2D Smagorinsky	YC2S
	Physical	2D Smagorinsky	YP2S
Janjic/MYJ	Coordinate	2D Smagorinsky	MC2S
	Physical	2D Smagorinsky	MP2S
Pleim/ACM2	Coordinate	2D Smagorinsky	PC2S
	Physical	2D Smagorinsky	PP2S
MM5/None	Physical	1.5-Order TKE	NP15
	Physical	3D Smagorinsky	NP3S

3.4 Methods to Obtain Stable Solutions

The so-called "model spin-up problem" describes the effect of downscaling global gridded model analysis to the fine-scale grids used in mesoscale NWP systems. The interpolation schemes used for this downscaling results in smooth, meteorologically unrealistic fields on the mesoscale. Mesoscale models such as the WRF model, slowly evolve solutions originating from these initial fields on an appropriate scale. Thus, a certain period of time is needed to obtain realistic atmospheric fields. Model results are coupled strongly with initial conditions, thus the time spent in the beginning of a model simulation can potentially influence the final solution greatly. In an attempt to alleviate the model spin-up problem, two methods are prescribed to obtain stable solutions of atmospheric fields. The results are investigated to determine if either method is required, and if so, which one is more suitable for the conditions present in this study.

The first procedure is referred to as the warmstart method. The model is initialized at a sufficiently long period of time prior to the desired simulation window. This allows the fields to become adjusted and meteorologically balanced on the appropriate

grid scale. Essentially, at the beginning of the preferred simulation time period, the model will have access to more representative fields, in a physical sense.

The second method is referred to as cycling. This procedure forces a stable diurnal periodic regime by applying the same boundary conditions for subsequent runs. A normal coldstart model run is made for day N. The final output at day $N+1$ is then input as initial conditions for day N, leaving the boundary conditions untouched. This process is repeated until the differences in meteorological quantities between each cycle is sufficiently small. This method assumes that a diurnal regime exists in nature.

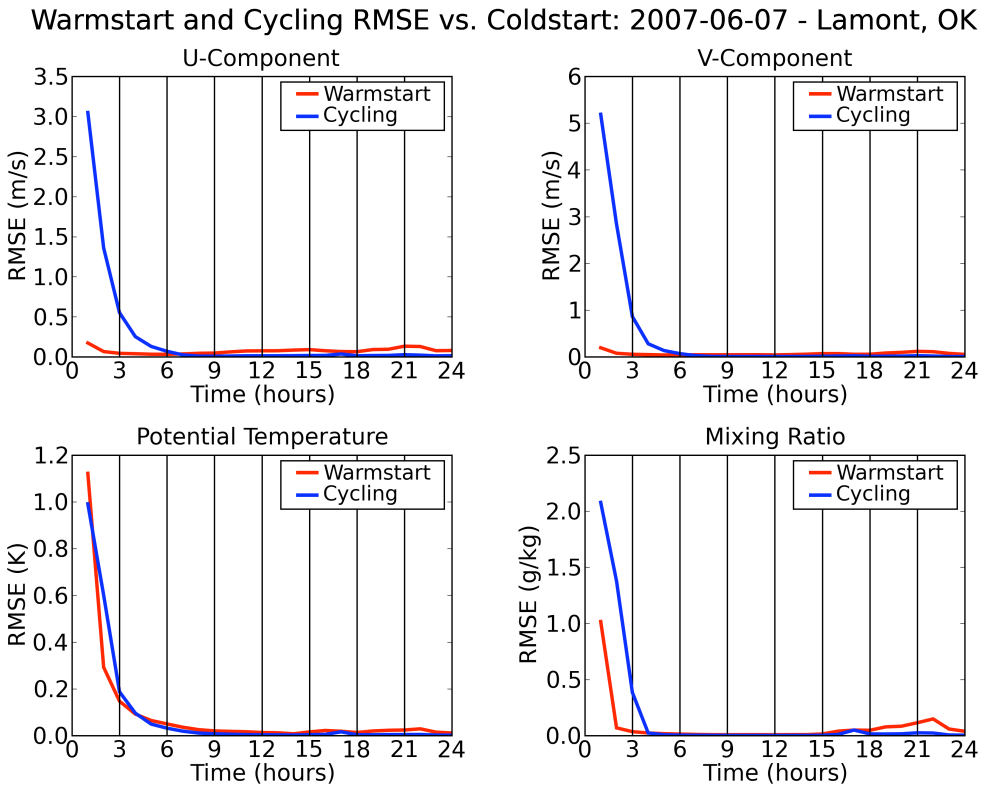

Figure 3.5: RMSE of Warmstart and Cycling versus Coldstart taken at the first model level on June 7, 2007.

These methods were investigated for the Lamont, Oklahoma domain. The dates of interest are June 7, 2008 and June 8, 2007. A warmstart model run was initialized at

$00Z$ June 5, 2007 and lasted for a simulation time period of 96 hours. Additionally, cycling was performed for three iterations on June 7, 2008. The results from the warmstart and cycling methods were then compared to those of a traditional coldstart simulation for the day of June 7, 2007. For each method, hourly horizontal temporal averages were taken at the first model level. The root mean squared error (RMSE) of the resulting fields were taken between the warmstart and cycling methods with those from the normal mode. Figure (3.5) illustrates the time evolution of these differences.

It is clear that both methods illustrate a model spin-up time ranging from three to six hours. Beyond that time, RMSE between either method and the normal cold-start mode approach sufficiently small differences. Furthermore, results indicate that a warmstart period of only 6 to 12 hours would prove sufficient instead of the prescribed 48 hours. In this study, the time period from 12 hours to 24 hours is investigated. Subsequently, either warmstart or cycling methods would be appropriate since solutions converged within the window of interest. However, cycling is heavily dependent on the assumption that a clear diurnal pattern exists and should accordingly be used under greater scrutiny. This flexibility, coupled with the computational cost of cycling, lends the warmstart method as the preferred technique to obtain stable solutions in this study.

3.5 Nudging in LES

LES offers a method in which to nudge solutions toward larger-scale atmospheric conditions. This method is employed because LES has no internal knowledge of such conditions. The lack of such knowledge may lead to LES solutions growing unbounded from observational data. The nudging procedure is referred to as a force-restore method. Horizontal averages are taken of LES solutions and objective analyses (OA) at the previous time-step. Those averages are differenced and a nudging factor is applied to those differences. The result is a nudging force applied locally at every

vertical level to LES solutions at the current time-step. Eq. (3.6) describes the nudging method.

$$\mathrm{F}_{\mathrm{nudge}} = (\overline{LES^{t-1}} - \overline{OA^{t-1}})\Delta \ , \tag{3.6}$$

where $\Delta = 3600^{-1}\mathrm{s}^{-1}$ is the nudging factor.

It is important to note that OA are only used to bound the LES solutions to physically reasonable magnitudes based on observational data. In this study, OA from the Rapid Update Cycle (RUC) model were used. The nudging procedure was newly implemented in LES during this study and the RUC data represented a first attempt at employing a larger-scale data-set. The use of RUC data does not imply a preference, rather the limited scope of the newly implemented nudging procedure dictated their use.

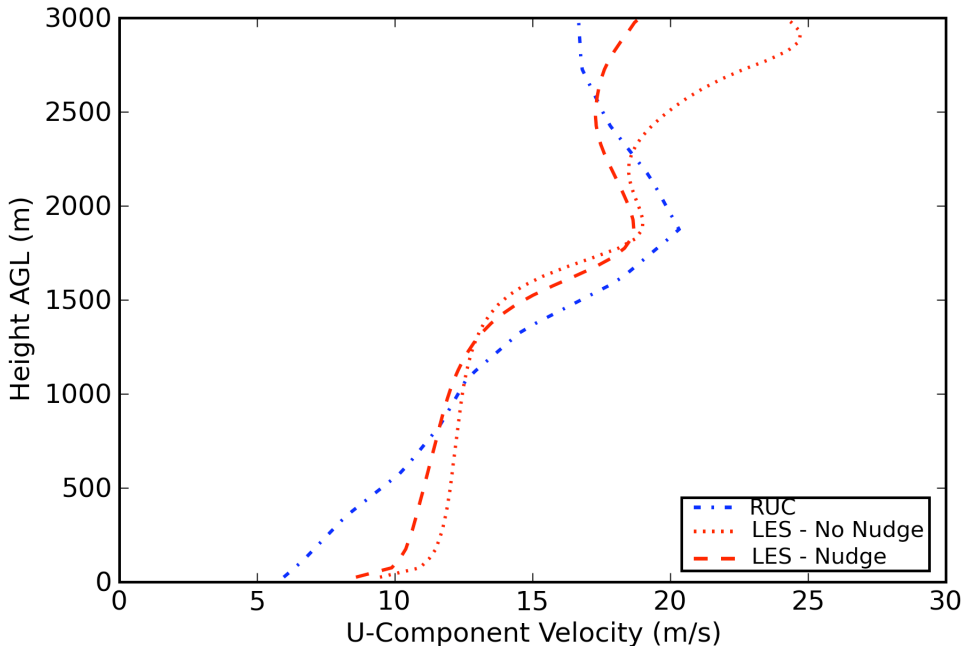

Figure 3.6: Vertical profile of u-component velocity (m/s) for June 7, 2007 18UTC. Values at each level represent the horizontal planar average taken across the comparison domain. The nudging effects are evident in the nudged and non-nudged LES solutions.

Obviously, larger-scale objective analyses reproduce much more coarse near-surface profiles, so it is important that the nudging procedure only effects the magnitudes of the LES solutions and not the general structure. Figure (3.6) illustrates that the nudging procedure utilizing RUC analyses guides LES solutions towards the observed values, but does not appreciably alter their vertical structure. Subsequently, the nudged LES solutions were considered "truth" for all comparisons, as they offered the best combination of high-resolution simulation data and larger-scale compliance.

Chapter 4

Verification in Conjunction with LES

Two cases from June 2007 were chosen based on their meteorological representativeness of late spring conditions in Oklahoma. The Dryline Case of June 7th included strong warming, wind shifts, and moisture changes associated with the passage of a dryline. The Postfrontal Case of June 8th was preceded by the passage of a cold front in the overnight hours and included the associated cooler temperatures, northerly winds, and stronger static stability. Sensitivity of model predictions is investigated in this chapter by employing different and sensible configurations of TTSI schemes. Additionally, the model representation of TTSI sub-grid scale processes is examined by studying the comparability of WRF model predictions with observational and fine-scale numerical simulation data.

Table (3.2) lists eight separate configurations utilized in the comparative study. This is reduced to six by removing NP3S and NP15 from consideration. The reason for this is evident in Figure (4.1), as the absence of a PBL scheme clearly results in far too little mixing. This behavior is consistent across all results, meaning that any additional discussion is simply redundant. It is important to note that the omission of NP3S and NP15 is specific to the cases presented in this thesis. Further studies are required to make a statement about the generality of this behavior. Accordingly, those two configurations are not discussed further. The remaining six model configurations are further reduced to three by removing YC2S, MC2S, and PC2S. Due to the relatively uniform nature of the comparison domain terrain, as seen in Figure (3.2), solutions are indiscernible when comparing those configurations which

calculated diffusion in coordinate space versus physical space. The configurations employing physical space diffusion calculations were arbitrarily chosen over those using such calculations in coordinate space. Subsequently, the three remaining configurations considered in the comparison study are YP2S, MP2S, and PP2S.

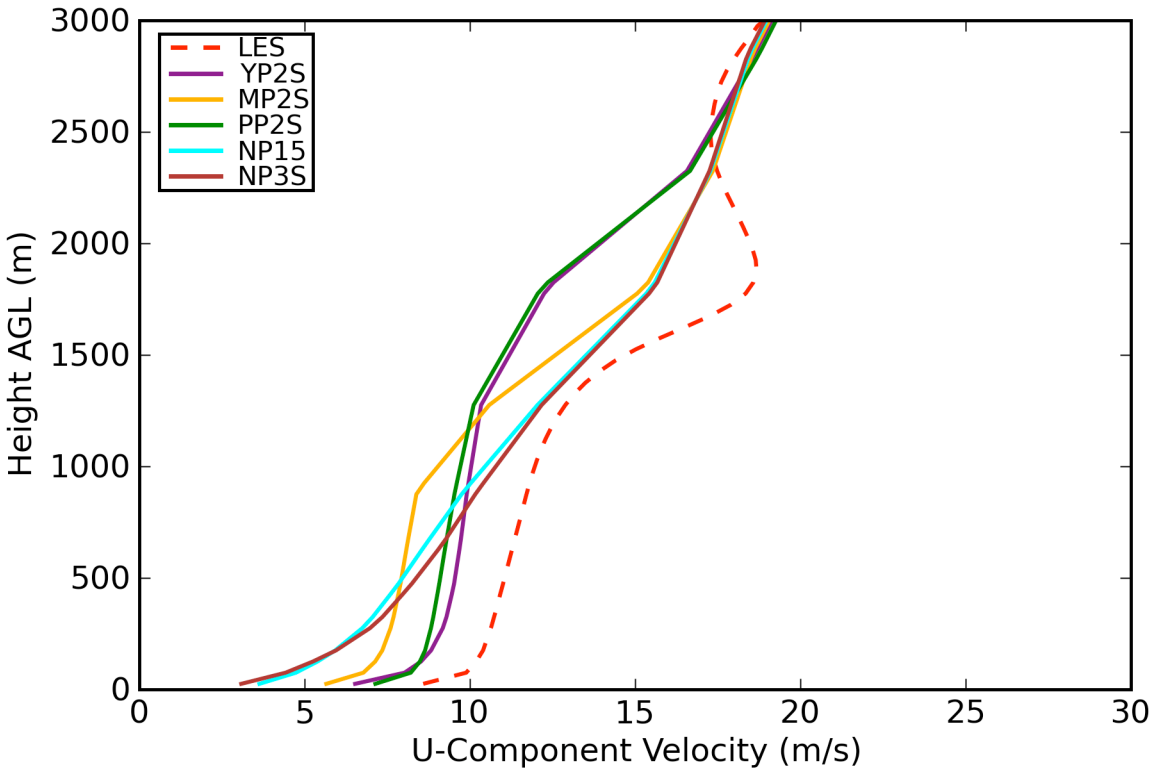

Figure 4.1: Vertical profile of u-component velocity (m/s) for June 7, 2007 14UTC. Values at each level represent the horizontal planar average taken across the comparison domain. Lack of mixing is evident in the NP3S and NP15 configurations.

4.1 Statistical Methods for Comparisons

While the idea of comparing model solutions on disparately spaced grids with differing temporal resolutions may seem straightforward, the method to go about such comparisons is not. Great care must be given to ensure that the best spatial and temporal representation of atmospheric quantities are produced for each respective

set of solutions. The first main procedure for collating model solutions is time series analysis of a particular meteorological field at a prescribed level. A second is creating vertical profiles of such fields.

Time series analysis requires several conditions to successfully demonstrate temporal changes in an atmospheric quantity at a prescribed model level. First, meteorological fields must be averaged in the horizontal plane associated with the chosen vertical level. This allows for a spatially averaged sense of what is physically occurring at a given height. To ensure similitude between grids with differing vertical spacing, spatial averages must be interpolated to a congruous level. Generally, a level from one particular model is chosen as the default and the remaining solutions are then interpolated to the physical height corresponding to the default level. Once all spatial averages are interpolated to a common level, results are then carried forward in time.

To adequately compare each model's vertical representation of the atmosphere, similar procedures to those used in time series analysis are implemented. Again, horizontal planar averages are taken, this time at each respective model level. In essence, each model has a vertical profile of horizontal planar averages located at its particular levels. Values are then vertically interpolated to consistent physical heights associated with the levels of the model chosen to be default.

It is important to realize that even carefully constructed comparisons are no proxy for evaluating forecast ability. Alternatively, these collations act to offer insight, strictly in a statistical sense, into the physical behavior of each model. Since no perfect solution exists, it is perfectly reasonable to approach comparisons in this way. Such a strategy holds for this study, as the main objective is to determine the capacity of numerical weather prediction models to reproduce TTSI characteristics that are physical in nature, rather than determining how close one grid point was to a single observation in time.

4.2 Dryline Case

The first experimental case was taken from June 7, 2007 12UTC - June 8, 2007 00UTC. Synoptic conditions present on this date are described in detail within (4.2.1). This date was chosen based on strong warming, wind shifts, and moisture changes associated with the passage of a dryline and is subsequently referred to as the Dryline Case hereinafter. Comparability of common atmospheric quantities and TTSI parameters in the WRF model with observational and fine-scale numerical simulation data are described and discussed in (4.2.2).

4.2.1 Synoptic Conditions

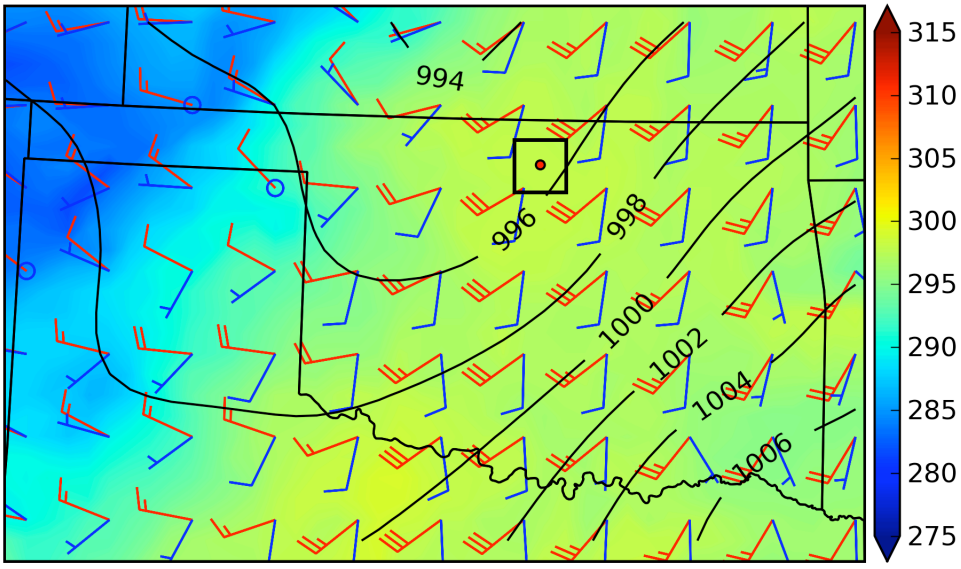

Figure 4.2: Synoptic conditions taken from RUC analyses for June 7, 2007 12UTC. Surface pressure (hPa) is the contoured quantity, surface temperature (K) is the shaded quantity, and surface winds and 850hPa winds (m/s) are the blue and red wind barbs, respectively. The black square represents the comparison domain, while the red dot depicts the location of the Lamont, Oklahoma ARM profiler site.

The beginning of the simulation period was marked by a surface low-pressure system in South Dakota. A cold front extended from South Dakota southwestward into New Mexico. The cold front intersected Oklahoma in the central portion of the panhandle. Extending from this cold front southward into the Texas panhandle was a dryline. Surface winds were from the south at 10ms^{-1}. Throughout the depth of the boundary layer, winds veered with increasing height as 850hPa winds were from the southwest at 30ms^{-1}. Accordingly, there existed pronounced wind shear in the boundary layer as seen in Figure (4.2).

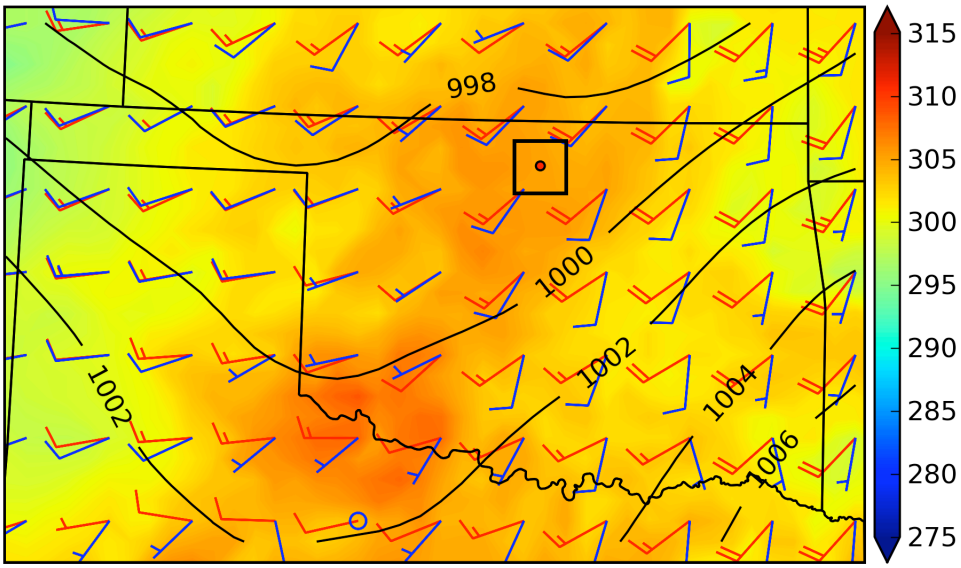

Figure 4.3: Same as Figure (4.2) but for June 7, 2007 18UTC.

As the day progressed, the surface low moved eastward into Minnesota. In Oklahoma, the dryline propagated eastward, allowing dry air to the west to rapidly heat. The temperature gradient associated with the surface cold front became more diffuse and the cold front retreated westward, as seen in Figure (4.3). By 18UTC, the dryline passed through the comparison domain and skies became clear. Surface winds shifted to southwesterly behind the dryline and became slightly weaker. Ahead of the dryline, winds remained southerly at 10ms^{-1}. 850hPa winds remained southwesterly but reduced in magnitude.

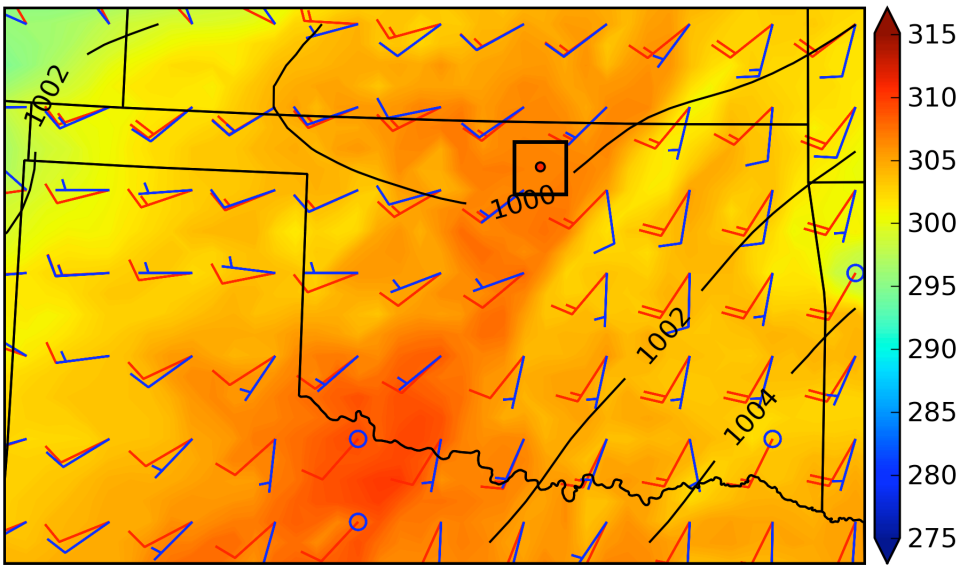

Figure 4.4: Same as Figure (4.2) but for June 8, 2007 00UTC.

By the end of the simulation period at 00UTC on June 8, 2008, the surface low-pressure system had propagated into Canada. The southern appendage of the cold front no longer existed due to mixing effects throughout the day. The dryline remained east of the comparison domain. Surface winds were westerly behind the dryline and southerly preceding the dryline, with speeds remaining between 5 and 10ms^{-1} as seen in Figure (4.4). Throughout the depth of the boundary layer, little shear existed behind the dryline with pronounced directional shear in front of the dryline and skies remained clear.

Strong mixing existed in this case as dry air left in the wake of the dryline warmed rapidly. Winds were fairly strong throughout the depth of the boundary layer with marked shear present in the beginning of the simulation. Both directional and speed shear reduced as the dryline propagated through the comparison domain, turning surface winds from the southwest. It is clear that the dryline affected the temporal evolution of meteorological fields beyond what the normal late springtime diurnal regime would produce in Oklahoma. Based on this, it is fair to categorize the Dryline Case as an inhomogeneous atmospheric environment.

4.2.2 Results

To gauge the spread of the LES and WRF model predictions in a general sense, timeline series of basic atmospheric quantities were examined. These time series give a sense of how each model diurnally progressed the atmosphere. As described in (4.1), careful consideration must be given in terms of comparing data that originate from different model grids, both spatially and temporally. Horizontal averages were taken at each model level in time. After comparing where the lowest model existed in physical space for each model, it was determined that LES provided the ideal comparison height of 25m. Accordingly, values from the WRF model were linearly interpolated in the vertical to coincide with 25m. Results were then plotted over the entire simulation window, from June 7, 2007 12UTC to June 8, 2007 00Z.

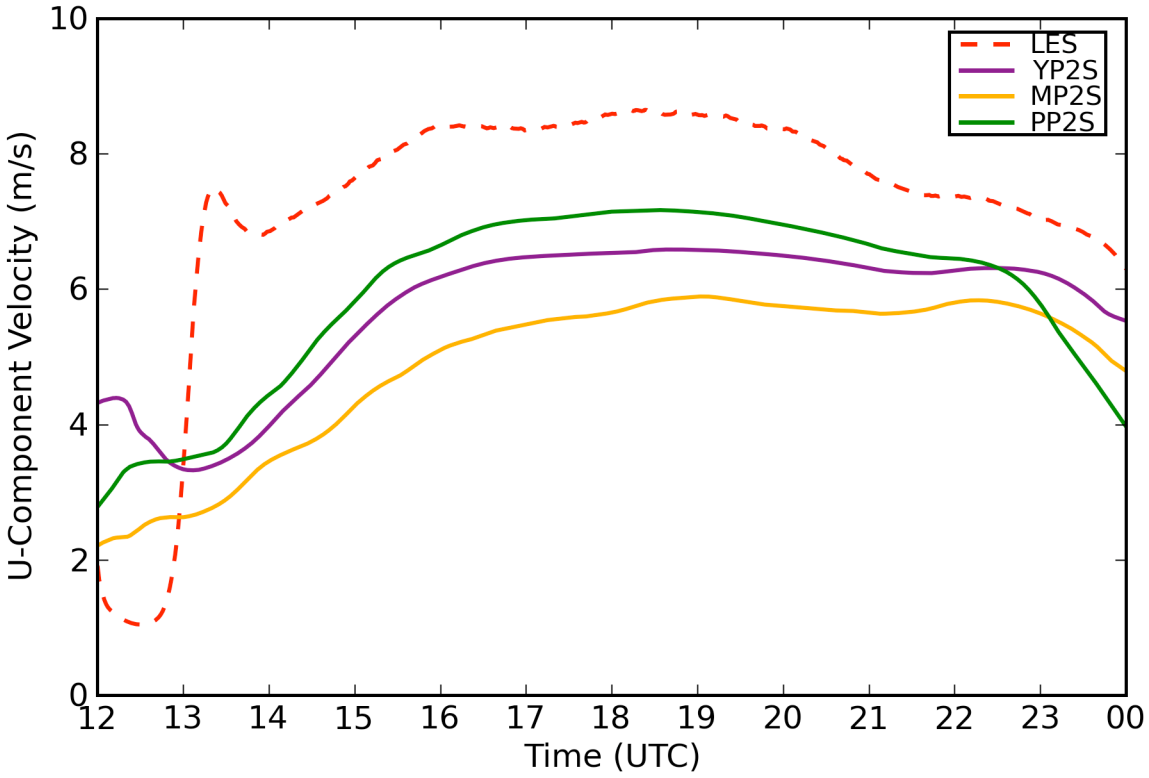

Figure 4.5: Time series of 25m u-component velocity (m/s) for the entire simulation window. Values represent the horizontal planar average taken across the comparison domain.

The first quantity compared was u-component velocity (ms^{-1}), as illustrated in Figure (4.5). Initially, LES predicted wind speeds spiked within and just past the first hour. It is possible that LES entered into the turbulence regime and thusly acted to mix the lower portion of the atmosphere more aggressively. As the day progressed, all WRF model configurations followed the general trend of LES, with PP2S being the closest and MP2S being the furthest away. LES remained above the magnitude of all WRF model configurations, meaning that there was larger surface layer shear effects present in LES. A note of interest was the rapid drop in wind speed at 22UTC, as predicted by PP2S. This may indicate that PP2S approached stable conditions faster than the other configurations.

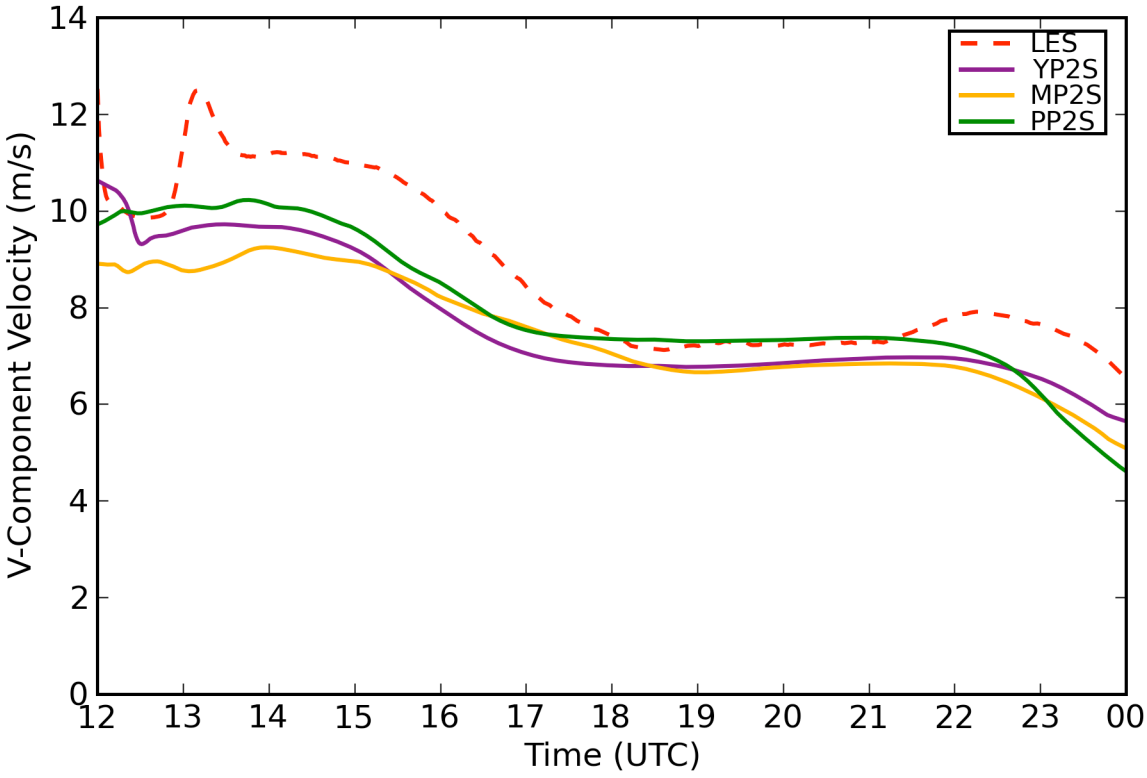

Figure 4.6: Time series of 25m v-component velocity (m/s) for the entire simulation window. Values represent the horizontal planar average taken across the comparison domain.

The next quantity compared was v-component velocity (ms^{-1}), shown in Figure (4.6). LES solutions again spiked within the first few hours, well away from the WRF model predictions. After this spike, LES and WRF model predictions followed the same trend. Again, LES simulated higher wind speeds than did any WRF model configuration, meaning that larger surface layer shear effects were present in LES. PP2S remained closest to LES for a majority of the day, with MP2S and YP2S slightly lower in magnitude. As seen in Figure (4.5), PP2S dropped rapidly at 22UTC, indicating a faster entrance into stable conditions.

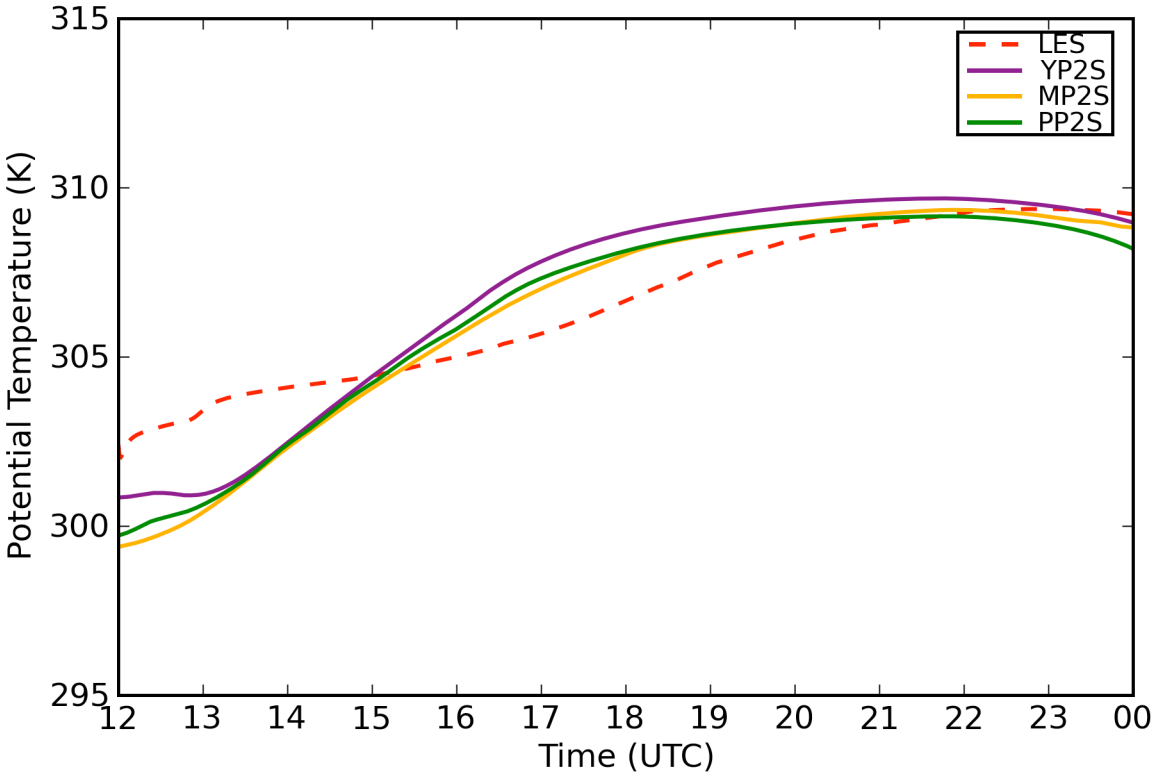

Figure 4.7: Time series of 25m potential temperature (K) for the entire simulation window. Values represent the horizontal planar average taken across the comparison domain.

Additionally, potential temperature (K) was compared, as illustrated in Figure (4.7). It is immediately evident that all WRF model predictions overestimated cooling effects during the overnight hours. It took three hours for every WRF model

configuration to match the values predicted by LES. After 15UTC, all WRF model predictions for potential temperature surpassed values prescribed by LES, indicating stronger warming effects by the WRF model. By the end of the simulation window, WRF model predictions closely followed those from LES. PP2S remained closest to LES for a majority of the day, with YP2S being the furthest in magnitude. PP2S again exhibited a reduction in magnitude at 22UTC as described previously.

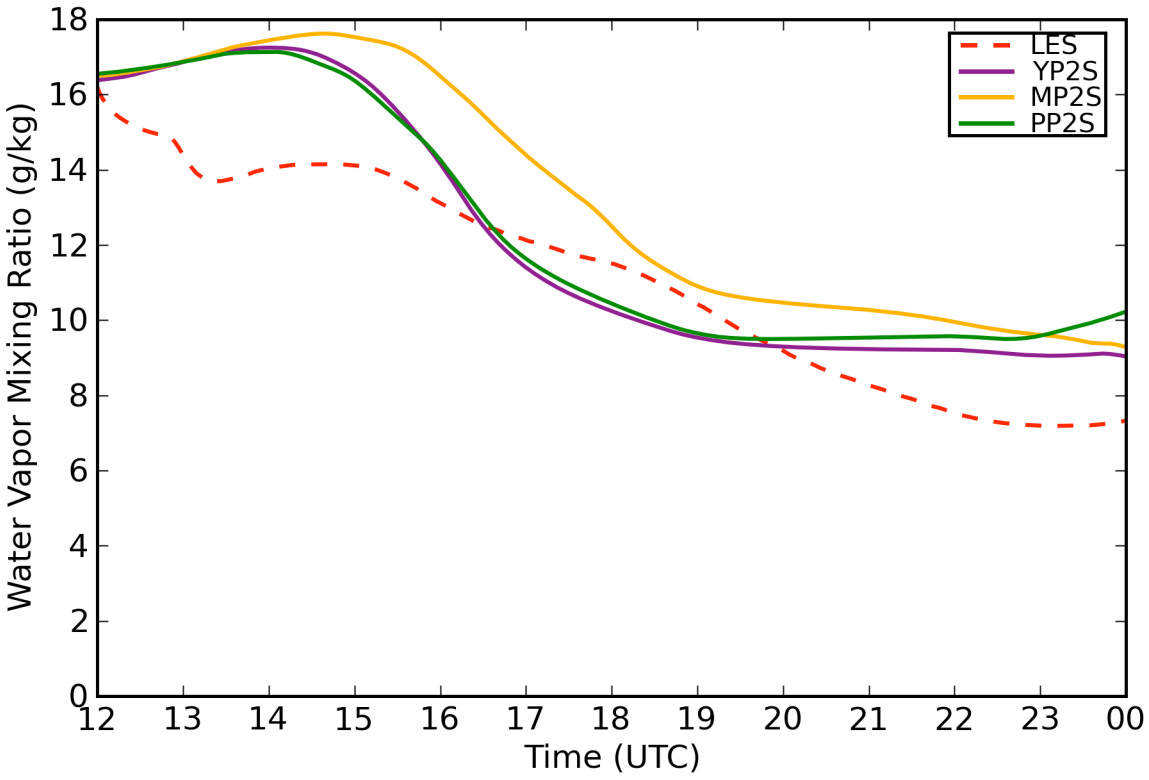

Figure 4.8: Time series of 25m water vapor mixing ratio (g/kg) for the entire simulation window. Values represent the horizontal planar average taken across the comparison domain.

Finally, water vapor mixing ratio (gkg^{-1}), was compared. As illustrated in Figure (4.8), for the first five hours of the simulation, all WRF model configurations modeled larger moisture values than that prescribed by LES. In the following three hours, from 17UTC to 20UTC, PP2S and YP2S dropped below the LES predicted moisture values,

with MP2S remaining slightly larger. After 20UTC, every WRF model configuration overpredicted moisture when compared to LES. Throughout the day, PP2S and YP2S generally followed LES the closest and MP2S the furthest.

Another important comparison is that of the vertical representation of atmospheric quantities. Horizontal averages were taken at each model level in time. Here, WRF model planar averages were linearly interpolated in the vertical to coincide with the physical levels contained within LES. Consequently, such comparisons are only appraised in a statistical sense and offers no spatially exact determination of forecasting skill. Nonetheless, these comparisons allow for an understanding of how each model configuration diurnally evolves the vertical structure of the atmosphere.

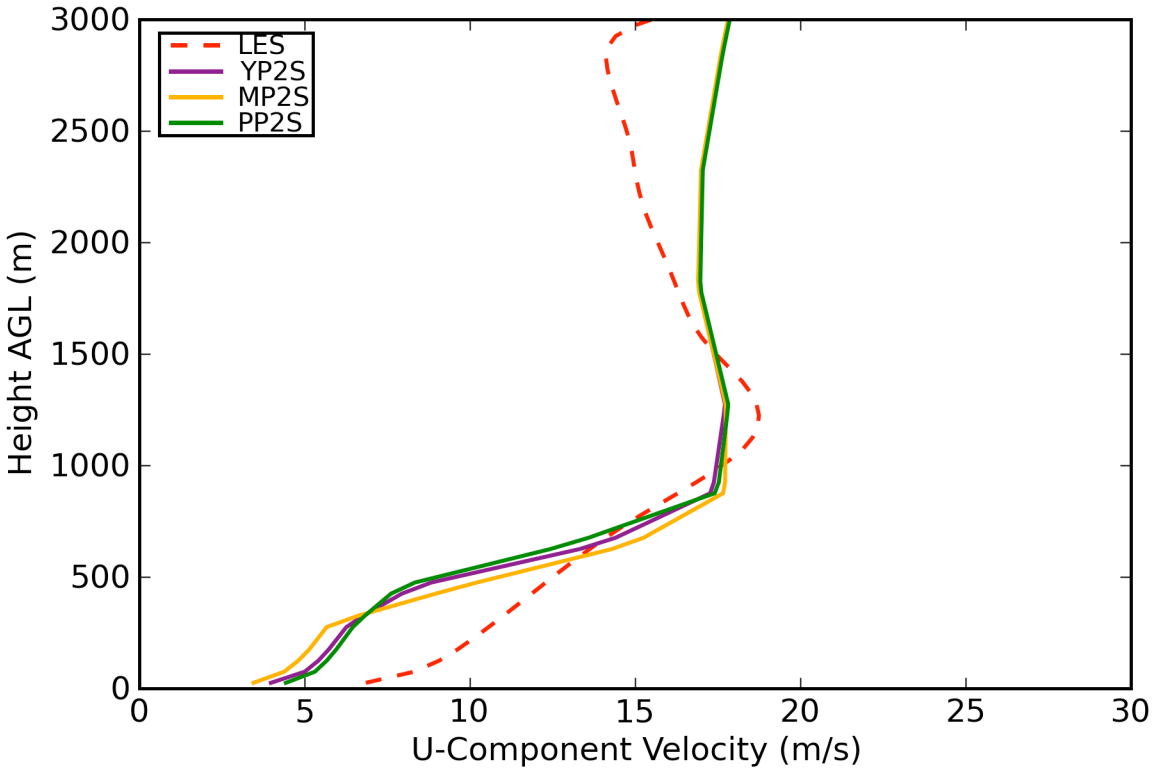

Figure 4.9: Vertical profile of u-component velocity (m/s) for June 7, 2007 14UTC. Values at each level represent the horizontal planar average taken across the comparison domain.

Figure (4.9) depicts the vertical structure of u-component velocity at 14UTC. It is evident that LES predicted larger surface layer shear effects than did any WRF model configuration. Every WRF model configuration failed to produce the same amount of mixing as LES, which is shown in the sharper slope of momentum below the low-level jet. All WRF model predictions depicted a more vertically uniform wind field above the low-level jet than prescribed by LES. The placement of the low-level jet was slightly higher in LES than in the WRF model. PP2S solutions were generally closest to LES predictions and MP2S solutions were the furthest away, although the differences were not significant.

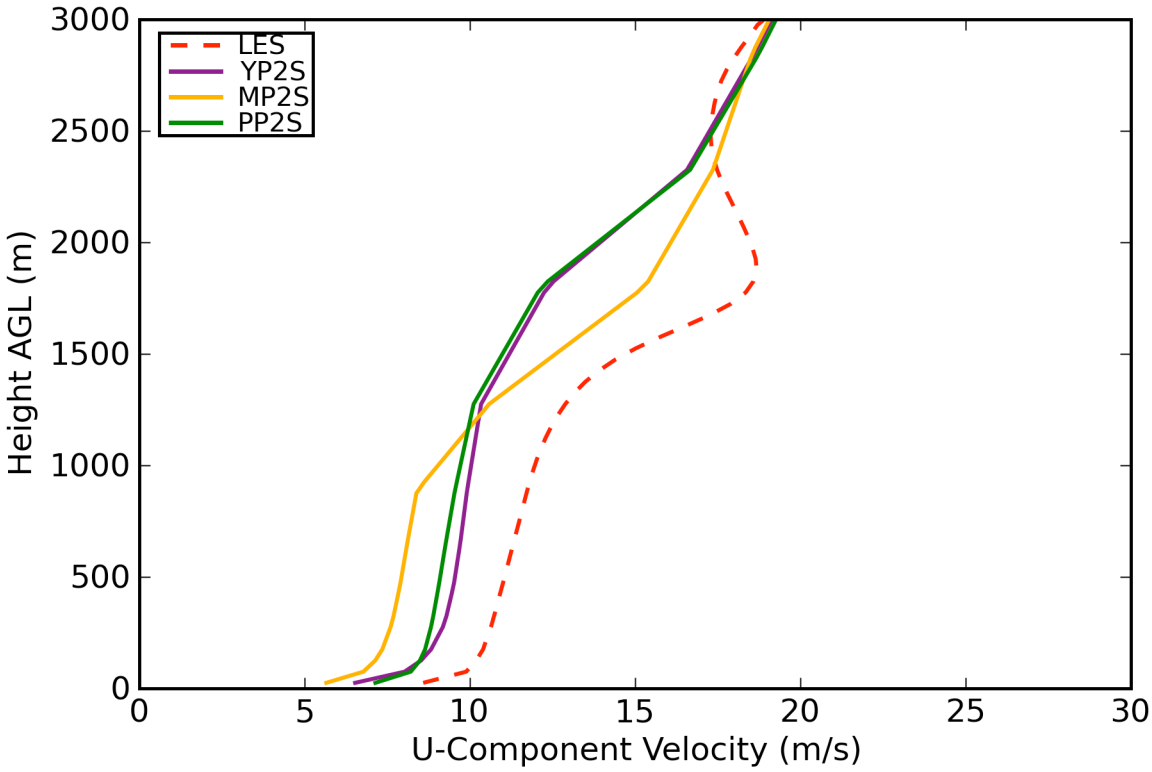

Figure 4.10: Same as Figure (4.9) but for June 7, 2007 18UTC.

In the middle of the simulation window, as seen in Figure (4.10), the 18UTC u-component velocity depicted far greater mixing than at 14UTC. Surface layer shear

effects remained greatest in LES. PP2S and YP2S predictions were closest to LES solutions, closely matching the mixed layer depth. MP2S produced the weakest mixing of the three WRF model solutions. Above the depth of the boundary layer, all WRF model solutions failed to reproduce the structure seen in LES.

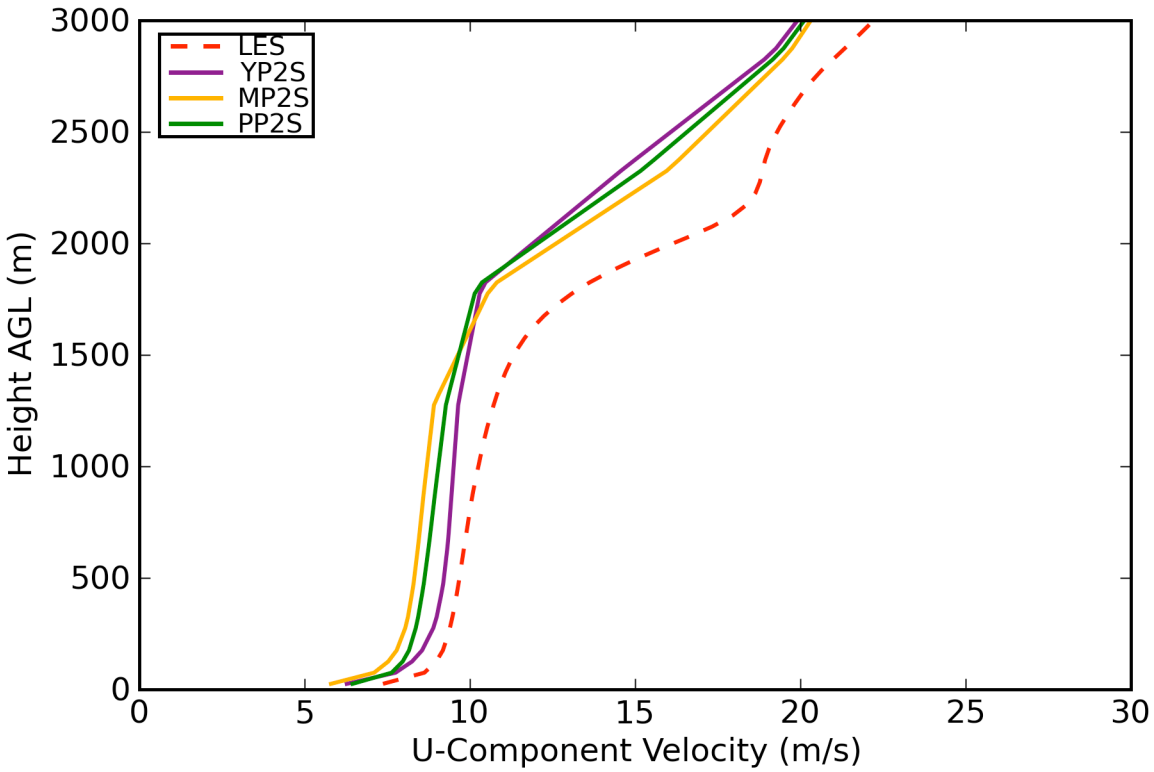

Figure 4.11: Same as Figure (4.9) but for June 7, 2008 22UTC.

Toward the end of the simulation window, the differences present at 18UTC were greatly reduced, as seen in Figure (4.11). Differences in near-surface magnitudes of u-component wind velocity were close for all WRF model solutions. The YP2S configuration was nearest in magnitude, while PP2S and MP2S did not greatly differ. For all WRF model solutions, the low-level shear was adequately reproduced but smaller than LES. The depth of the mixed layer was also closely matched. Below the depth of the boundary, all solutions remained close, but when moving above this level, LES solutions produced overestimated velocities on the order of 10ms^{-1}. Since LES

is initialized by a particular sounding, and then acts to mix that profile throughout the day, the differences seen at higher elevations may simply be residual effects from the initial profile.

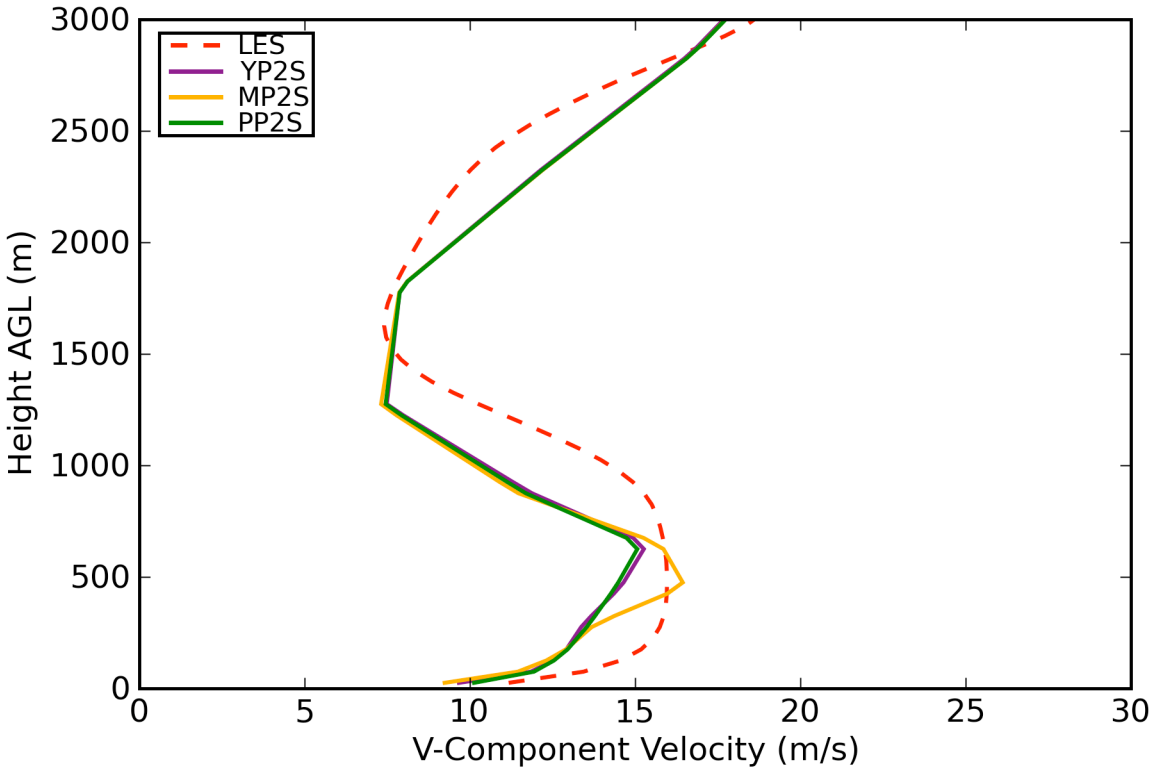

Figure 4.12: Vertical profile of v-component velocity (m/s) for June 7, 2007 14UTC. Values at each level represent the horizontal planar average taken across the comparison domain.

Secondly, the vertical structure of v-component wind velocity was examined. Figure (4.12) illustrates the vertical structure of v-component velocity at 14UTC. It is evident that LES predicted larger surface layer shear effects than did any WRF model configuration, as was seen in the vertical profile of u-component velocity. Every WRF model configuration failed to produce the same amount of mixing as LES, which is shown in the sharper slope of momentum below the low-level jet. All WRF model predictions closely followed the wind field above the low-level jet prescribed by LES. The placement of the low-level jet was nearly equivalent for WRF model solutions

and LES. PP2S solutions were generally closest to LES, but the other configurations did not differ greatly.

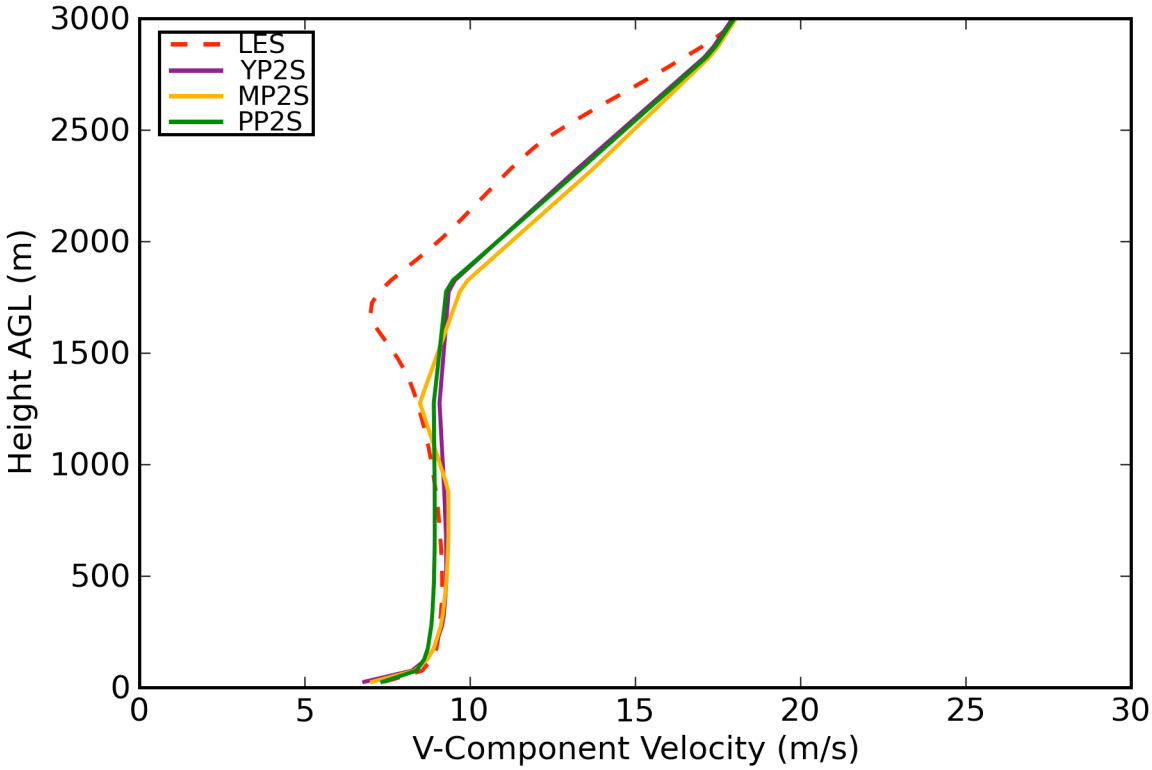

Figure 4.13: Same as Figure (4.12) but for June 7, 2007 18UTC.

At 18UTC, as seen in Figure (4.13), near-surface v-component wind velocities amongst separate model solutions were very close. Surface layer shear effects were slightly greater in LES predictions. WRF model solutions closely followed the vertical structure prescribed by LES, in which higher momentum values were mixed downwards resulting in a well-mixed layer. PP2S and YP2S solutions more closely represented the depth of the well-mixed layer as simulated by LES, while MP2S produced a much more shallow layer. These WRF model solutions bifurcated from LES predictions once above the depth of the boundary layer, in which they continued the well-mixed layer while LES solutions produced winds that weakened with height. This difference is likely the aforementioned residual effects of the initial profile used in

LES. Essentially, one profile is given and LES will act to mix that profile throughout the day. However, it does not have updated information regarding the actual state of the atmosphere outside of the nudging force. This means that LES had yet to mix far enough in the vertical to greatly change the initial structure prescribed by the RUC analyses.

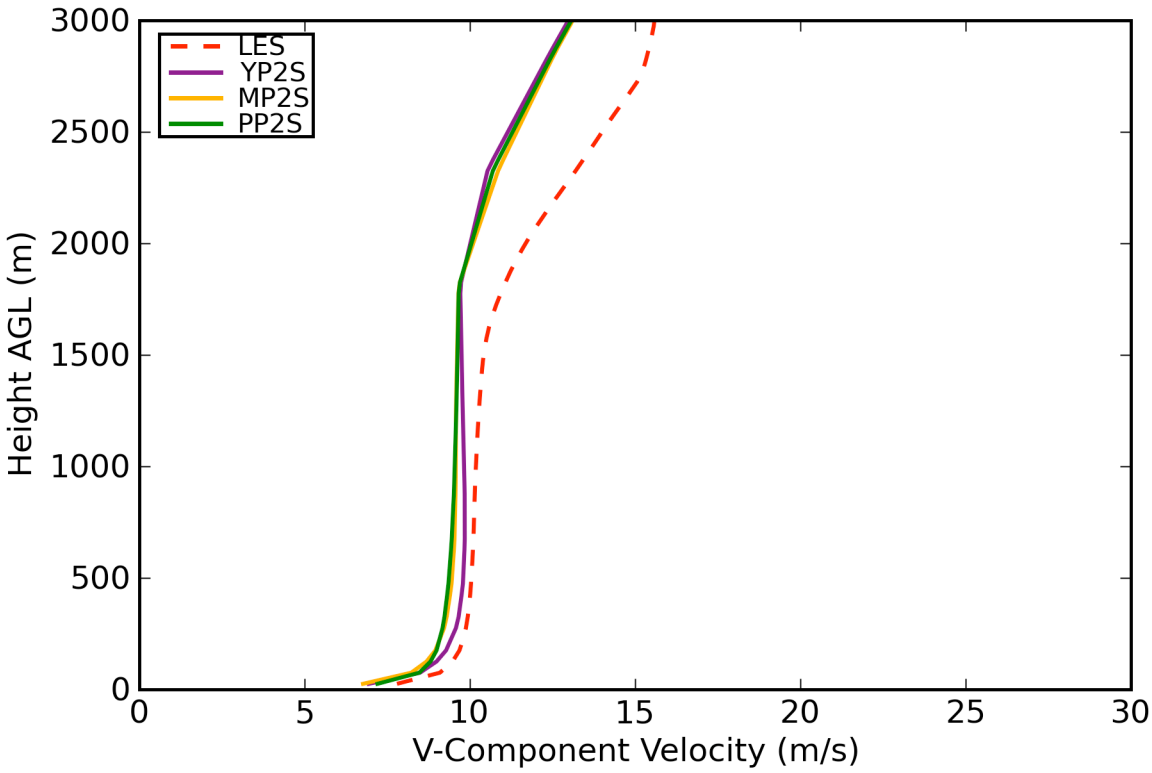

Figure 4.14: Same as Figure (4.12) but for June 7, 2007 22UTC.

Vertical profiles of v-component wind velocity taken near the end of the simulation window, as depicted in Figure (4.14), were consistent. Behavior in the surface layer and throughout the well-mixed layer was consistent between WRF model and LES predictions, with LES indicating slightly higher surface layer shear effects. Above the depth of the boundary layer, the LES profile reproduced larger wind shear, while the WRF model solutions indicated weaker increase in velocity with height. This may

indicate shear effects associated with entrainment processes, in which it appears that LES better reproduced such effects.

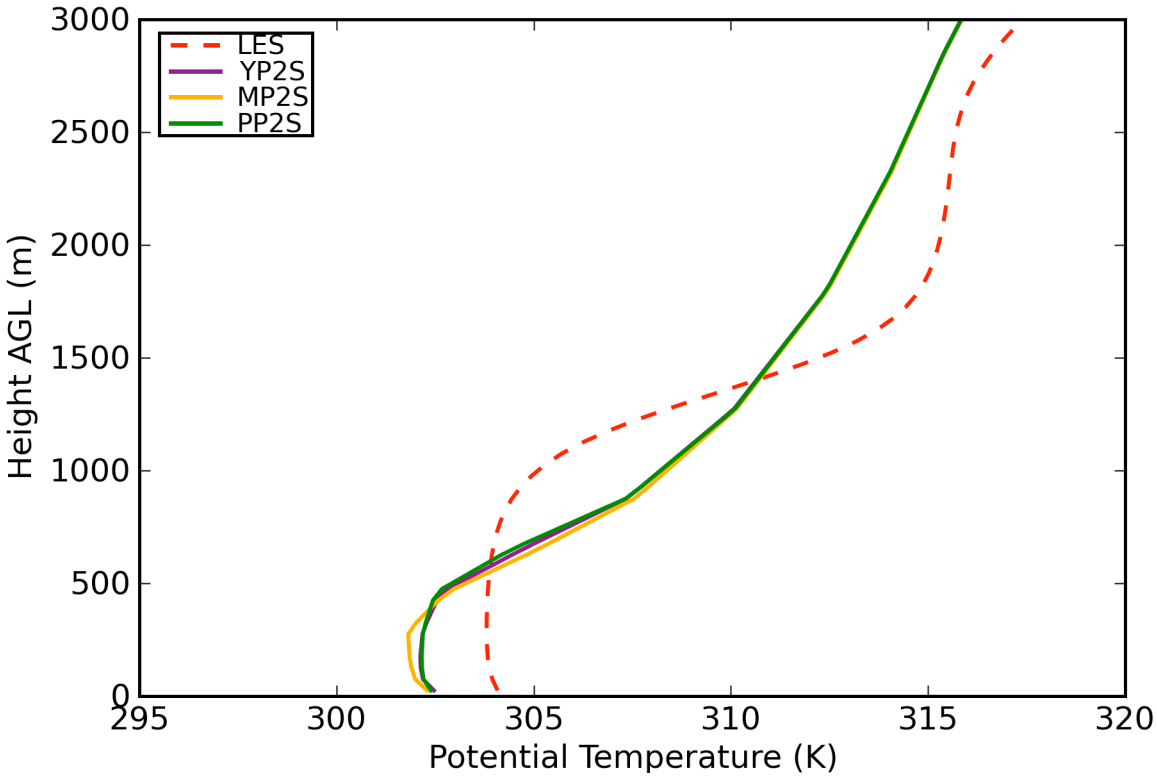

Figure 4.15: Vertical profile of potential temperature (K) for June 7, 2007 14UTC. Values at each level represent the horizontal planar average taken across the comparison domain.

Additionally, the vertical nature of potential temperature was investigated. Figure (4.15) represents the vertical profiles of potential temperature at 14UTC. As seen in Figure (4.7), the 12h predictions from the WRF model were consistently cooler in the near-surface regions for the first few hours in the simulation window. Consistent with momentum profiles, weaker mixing existed for the WRF model solutions when compared with LES. LES indicated a neutral near-surface atmosphere, with a stronger stable layer, indicated by a large positive gradient of potential temperature, extending from 1100m to 1600m above ground level (AGL). Above this layer, the atmosphere returns to nearly isothermal. All WRF model configurations reproduced a much

shallower neutral layer than LES, with MP2S modeling the smallest mixing of the three configurations. Above the well-mixed layer, all WRF model solutions followed closely with each other, but were 2K cooler than LES predictions.

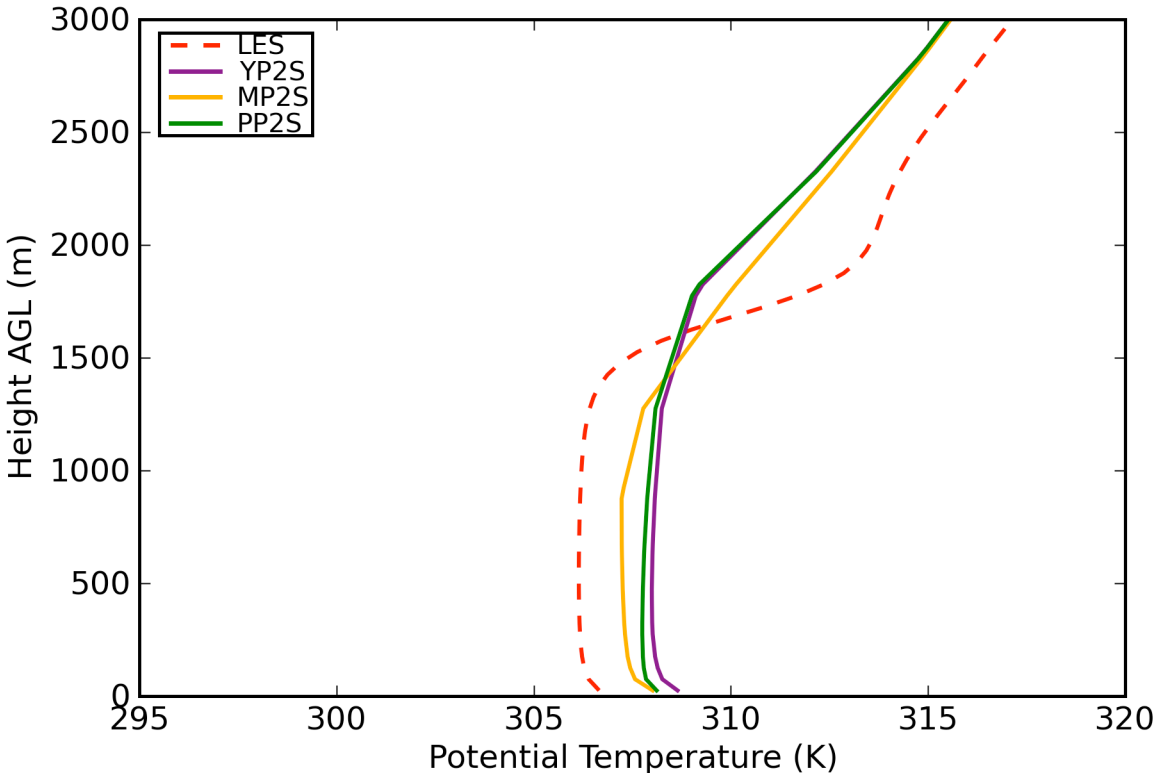

Figure 4.16: Same as Figure (4.15) but for June 7, 2007 18UTC.

As illustrated in Figure (4.16), the WRF model predictions for potential temperature warmed beyond LES solutions. While magnitudes between LES and WRF model predictions differed by upwards of 3K, the SL structure of both solution sets were similar. The MP2S configurations reproduced a much shallower well-mixed layer than is present in LES solutions. Conversely, the YP2S and PP2S configurations reproduced an equally deeper well-mixed layer compared to the LES predictions. Above this well-mixed layer, LES solutions depict a layer with strong vertical gradient of potential temperature, spanning approximately 500m. Entrainment effects and the previously mentioned residual effect are logical reasons for this behavior. All WRF

model configurations produced a much weaker vertical gradient in potential temperature above the well-mixed layer. Above the level of notable vertical gradient, all WRF model solutions reproduced similar behavior to that of LES predictions, represented by a linear increase in potential temperature with height.

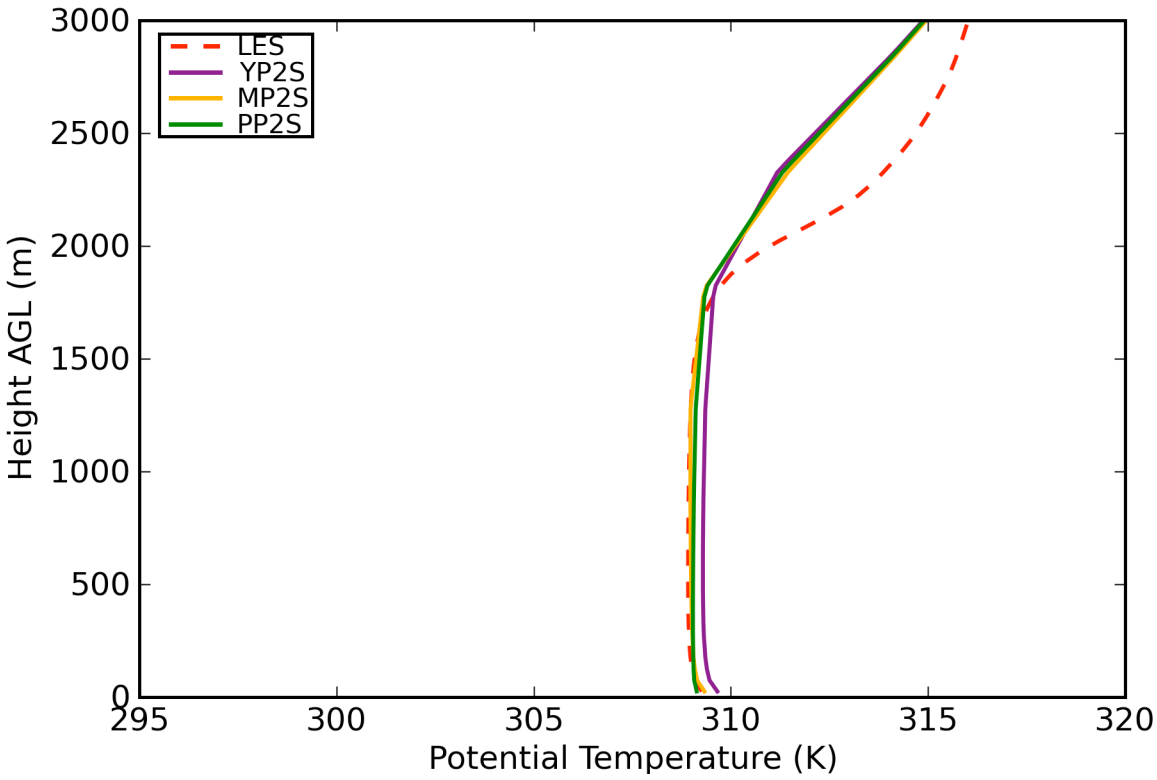

Figure 4.17: Same as Figure (4.15) but for June 7, 2007 22UTC.

Toward the end of the simulation window, all of the WRF model configurations reproduced nearly identical vertical structure of potential temperature to that of the LES predictions as seen in Figure (4.17), with the exception of the PP2S configuration. The PP2S combination depicted a stronger stably-stratified SL than any other configuration. This seems to indicate that PP2S enters stable conditions before other schemes. For all model solutions, the atmosphere was represented as nearly isothermal extending to 2000m AGL. The depth of the well-mixed layer is consistent

amongst all model solutions, with similar behavior above such layer as seen in the previous vertical profiles.

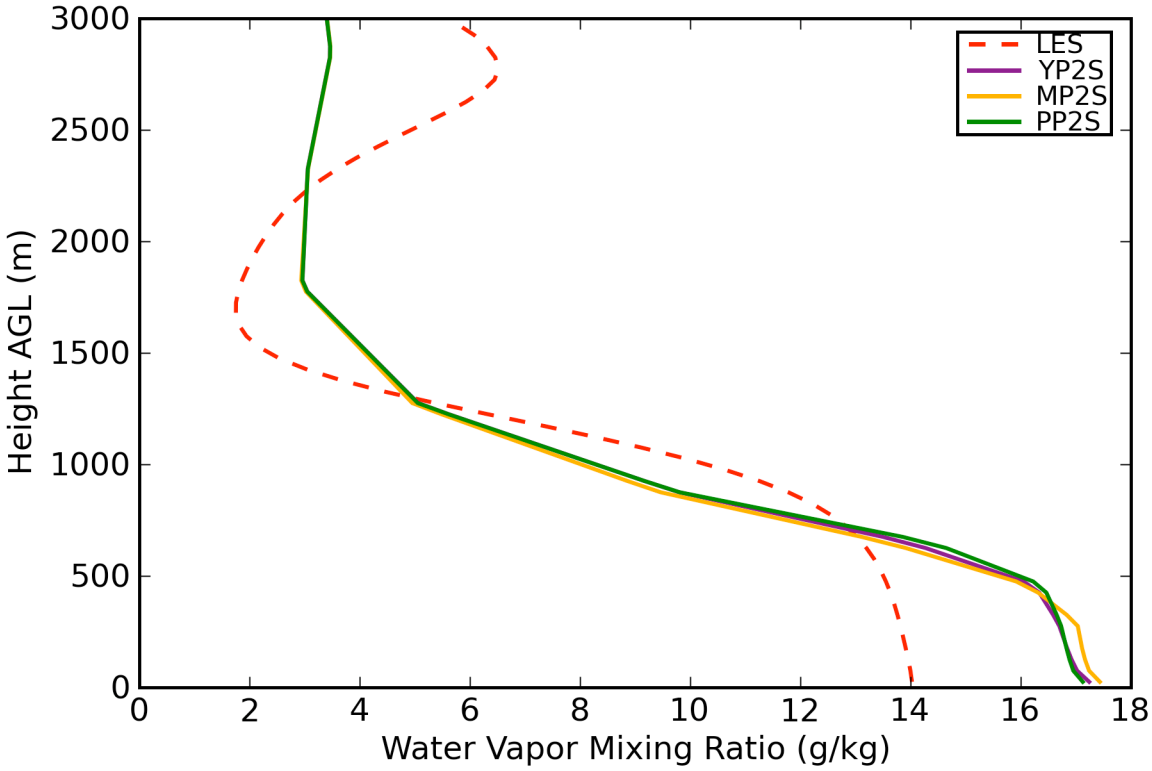

Figure 4.18: Vertical profile of water vapor mixing ratio (g/kg) for June 7, 2007 14UTC. Values at each level represent the horizontal planar average taken across the comparison domain.

Finally, water vapor mixing ratio was examined in the vertical, as illustrated in Figure (4.18). Within the well-mixed layer, all WRF model configurations depicted a considerably more moist atmosphere. Vertical mixing effects were deeper in LES. Both PP2S and YP2S solutions were similar to each other, with MP2S reproducing weaker mixing. Above the well-mixed layer, the vertical gradient of moisture was nearly identically produced by both the WRF model and LES. Above this strong gradient, it appears that LES once again reproduced entrainment effects. While the WRF model profiles showed a nearly uniform shape, the LES profile became drier,

then switched to more moist with height. This elevated positive moisture gradient may represent the overturning associated with entrainment processes.

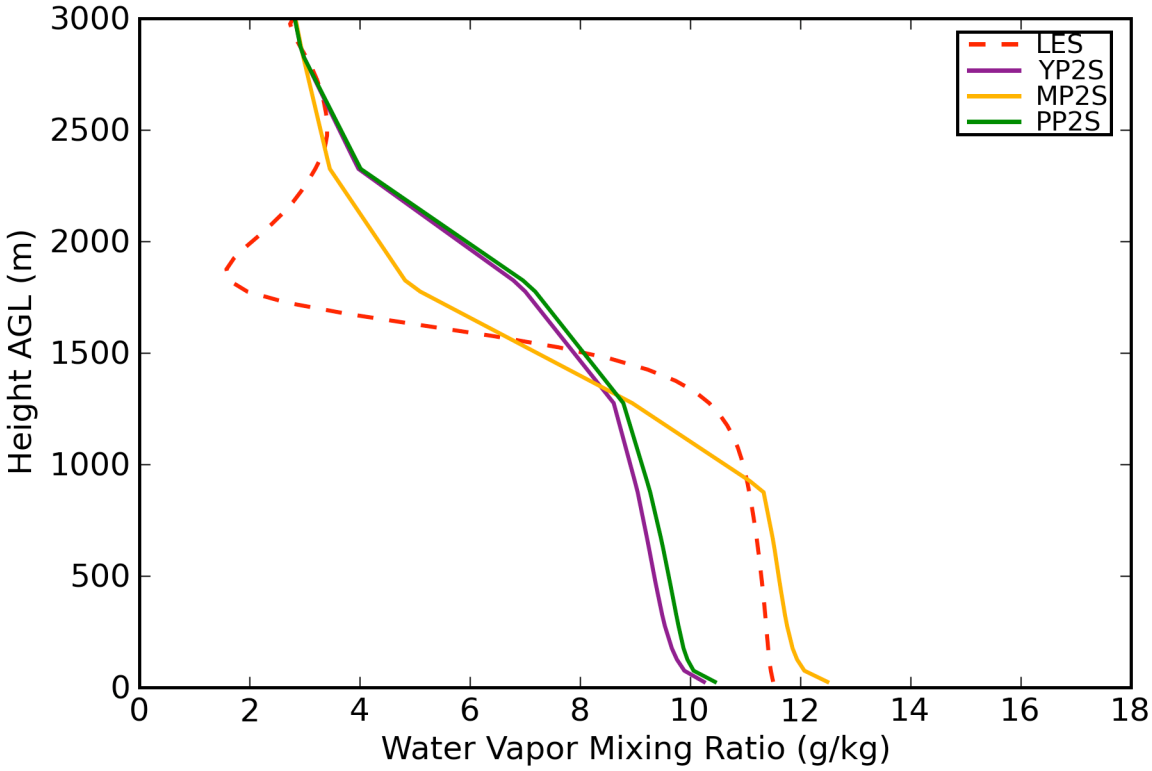

Figure 4.19: Same as Figure (4.18) but for June 7, 2007 18UTC.

Figure (4.19) illustrates the vertical profile of moisture at 18UTC. At this time, further mixing resulted in drier surface moisture values. MP2S reproduced a more shallow well-mixed layer, but was closer in magnitude to LES. PP2S and YP2S modeled drier conditions than LES, but represented stronger vertical mixing effects than MP2S. Above the strong negative moisture gradient, LES again reproduced a positive vertical gradient, possibly from entrainment processes. This behavior may also be a result of the aforementioned residual effect.

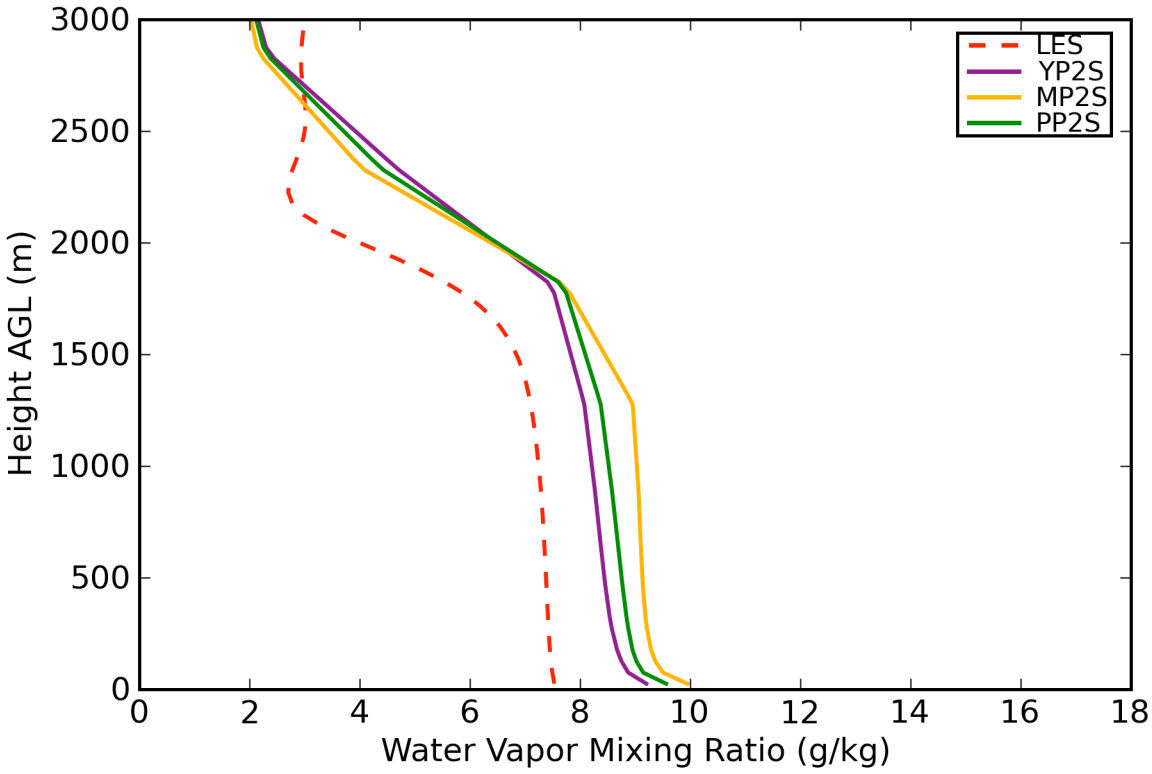

Figure 4.20: Same as Figure (4.20) but for June 7, 2007 22UTC.

At 22UTC, WRF model solutions closely followed the vertical structure of the LES predictions, as seen in Figure (4.20). All WRF model configurations represented a more moist near-surface layer. While MP2S reproduced the weakest vertical mixing, the depth of the well-mixed layer was nearly equivalently represented by all WRF model predictions. Above this layer, both WRF model and LES solutions followed the same general negative gradient with height. However, the LES profile again indicated an elevated positive moisture gradient which be a result of entrainment processes or residual effects above the boundary layer, while none of the WRF predictions did so.

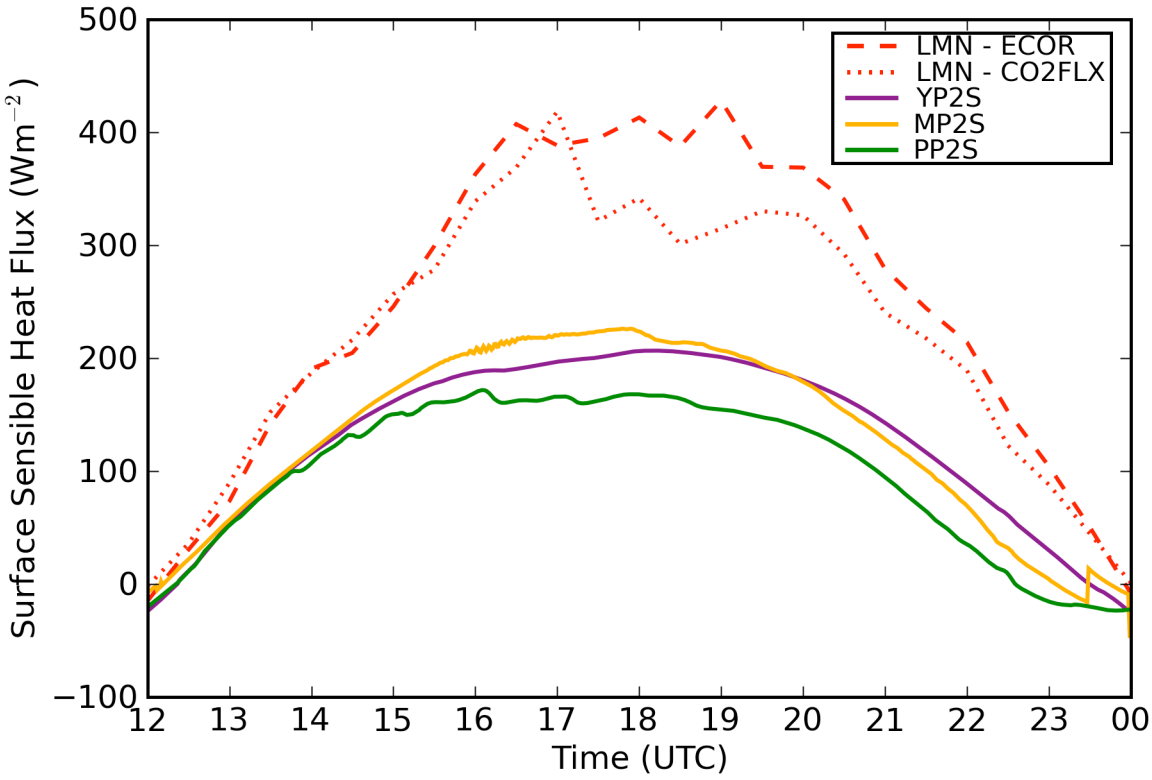

Figure 4.21: Time series of surface sensible heat flux (Wm^{-2}) for the entire simulation window. Values represent the horizontal planar average taken across the comparison domain.

Once basic first-order atmospheric quantities were examined, higher-order turbulence statistics were compared between LES and the WRF model configurations. The first such higher-order turbulence term inspected was the surface sensible heat flux (Wm^{-2}). The surface sensible heat flux is given by

$$H = \rho c_p \overline{w'\theta'} \ , \tag{4.1}$$

where ρ is density, $c_p = 1004 \text{Jkg}^{-1}\text{K}^{-1}$ is the specific heat of air at constant pressure, and $\overline{w'\theta'}$ is the kinematic heat flux. It is important to note that the surface sensible heat flux in LES represents prescribed values at a single point in space and time from the LMN ARM site, which are uniformly applied across the entire comparison domain. Oppositely, WRF model fluxes represent predicted values at each grid point averaged

in the horizontal plane. The ARM site calculates surface sensible heat flux with three different instruments. They are as follows: energy balance Bowen ratio station (EBBR), eddy correlation flux measurement system (ECOR), and carbon dioxide flux measurement system (CO2FLX). There existed substantial differences amongst each instrument. ECOR and CO2FLX were closest to each other, while something was clearly wrong with the EBBR sensor on this day. Accordingly, only the ECOR and CO2FLX measurements were used for comparison with the WRF model. The ECOR measurements were used to drive the internal equations in LES, while the CO2FLX measurements acted as independent validation source. Further discussion about each of the measurement devices is described in (4.4). In this case, WRF model predictions were underrepresented compared to ECOR and CO2FLX measurements. The WRF model contains internal knowledge of geographic land use through static geographic data and the LSM, whereas LES relies on a single point measurement. In this particular comparison domain, a river runs through the center portion and several smaller bodies of water exist. Surface heat flux values at these locations are much smaller than those on normal terrain. Thusly, if one takes a horizontal mean across the entire domain, the resultant value may be diluted compared to a single point measurement over land. However, choosing the grid-cell closest to the LMN measurement site resulted in similar values, as seen in Figure (4.21).

Magnitudes between LES and WRF model solutions were consistently within two orders of magnitude. WRF model solutions prescribed a lower surface heat flux than did any of the LMN measurements. The WRF model adequately predicted the diurnal parabolic pattern of surface heat flux. While most WRF model configurations remained very close in magnitude, PP2S reproduced smaller values for most of the day into the end of the simulation window. This is consistent with the potential temperature behavior described previously, in which the PP2S configuration underestimates

temperature towards the end of the day. This may indicate an early transition into the stable regime by the PP2S configuration.

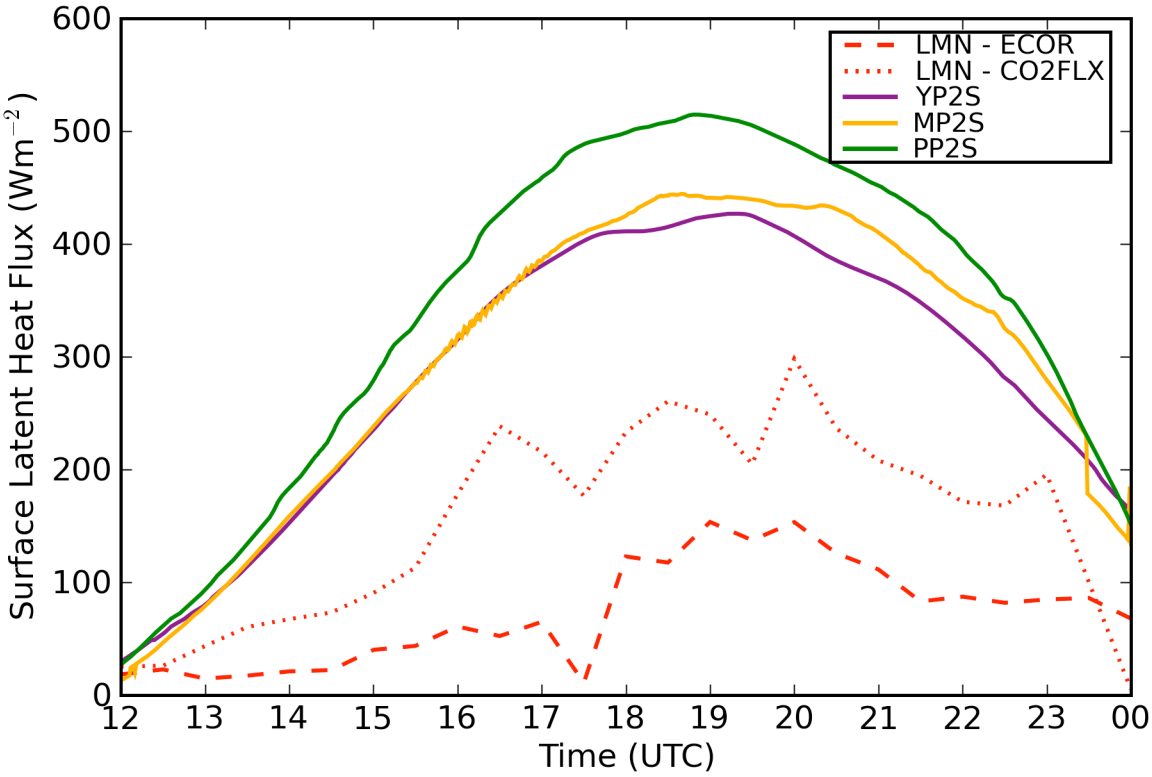

Figure 4.22: Time series of surface latent heat flux (Wm^{-2}) for the entire simulation window. Values represent the horizontal planar average taken across the comparison domain.

Time series analysis was also performed for the surface latent heat flux (Wm^{-2}), which is given by

$$LE = \rho L_v \overline{w'q'} \ , \tag{4.2}$$

where ρ is density, $L_v = 2.5 \times 10^6 \mathrm{Jkg}^{-1}$ is the latent heat of vaporization, and $\overline{w'q'}$ is the kinematic moisture flux. Again, surface flux values in LES represent a prescribed value from a single point observations applied uniformly across the entire domain and WRF model values represent the horizontal planar average across the comparison domain. Surface latent heat fluxes are presented in Figure (4.22).

The WRF model solutions depicted the parabolic shape of the diurnal pattern for surface latent heat flux as seen in the measurements. Magnitudes were close at the beginning of the simulation window. However, during the course of the day all WRF model predictions were notably overestimated. The peak value prescribed by CO2FLX and ECOR ranged between 150 and 300Wm^{-2}. The YP2S and MP2S configurations were the closest with surface latent heat flux values of roughly 400Wm^{-2}. PP2S was the furthest from the LMN measurements, with a peak value just over 500Wm^{-2}. It is unclear why the WRF model solutions are so appreciably overpredicted, but the behavior is consistent. When considering the fact that a dryline passed through the simulation domain, one would expect relatively larger sensible heat flux values and lower latent heat flux values. Accordingly, one would surmise that the LMN measurements should be trusted on this particular day. Subsequently, WRF model solutions appear to poorly partition surface fluxes.

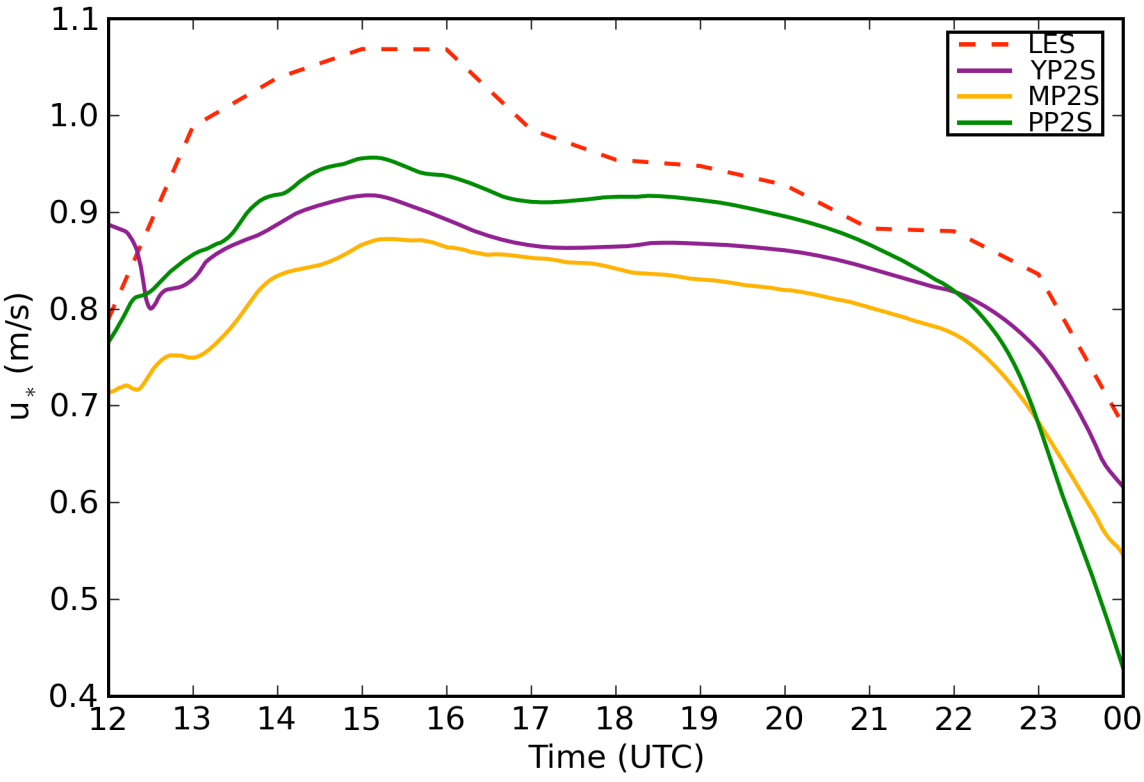

Figure 4.23: Time series of u_* (m/s) for the entire simulation window.

An important parameter from similarity theory is the turbulence velocity scale, or friction velocity (u_*), as defined by Eq. (2.1a). Figure (4.23) illustrates the horizontally averaged friction velocity for both LES and WRF model predictions. Both exhibit a gradual increase in the early portion of the simulation window as turbulence began to drive the boundary layer, followed by a gradual decrease for the remainder of the simulation window. PP2S and YP2S best represented the diurnal changes in friction velocity over the course of the entire simulation window. At 22UTC, the PP2S solution reduced dramatically from all other predictions. This response seems consistent with PP2S behavior of near-surface horizontal wind components, potential temperature, and surface sensible heat flux. Every WRF model configuration resulted in underestimated friction velocity. This means that shear production was greater in LES than in the WRF model.

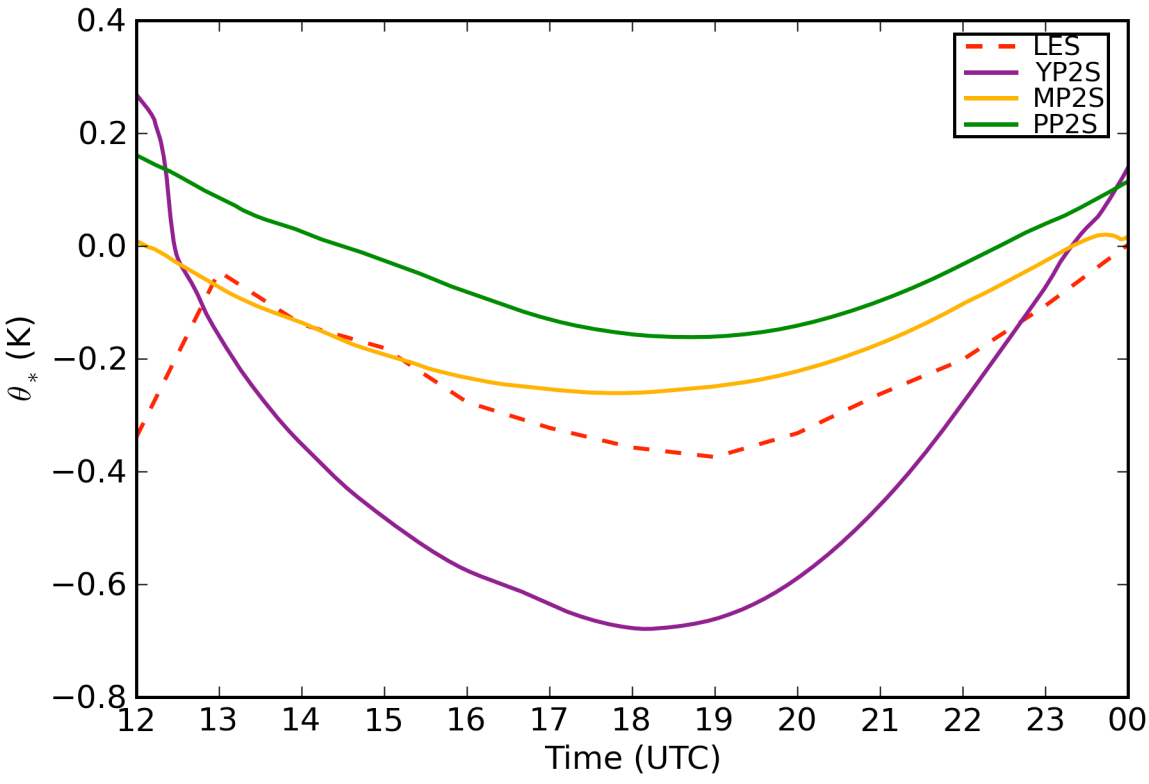

Figure 4.24: Time series of θ_* (K) for the entire simulation window.

Another parameter from similarity theory is the turbulence temperature scale (θ_*), as defined by Eq. (2.1b). Figure (4.24) illustrates the horizontally averaged turbulence temperature scale for both LES and WRF model solutions. With the exception of YP2S, every WRF model configuration predicted smaller negative values than did LES. This is directly explained from Eq. (2.1b), which indicates that the turbulence temperature scale is proportional to the surface sensible heat flux, which was underpredicted by the WRF model when compared to LES. The behavior of the turbulence temperature scale is not consistent with YP2S. There is an apparent error in the way that the scheme calculates θ_*, as it does not follow the requirement that $H = |u_*\theta_*|$. For YP2S $|\theta_*|$ is large beyond reason.

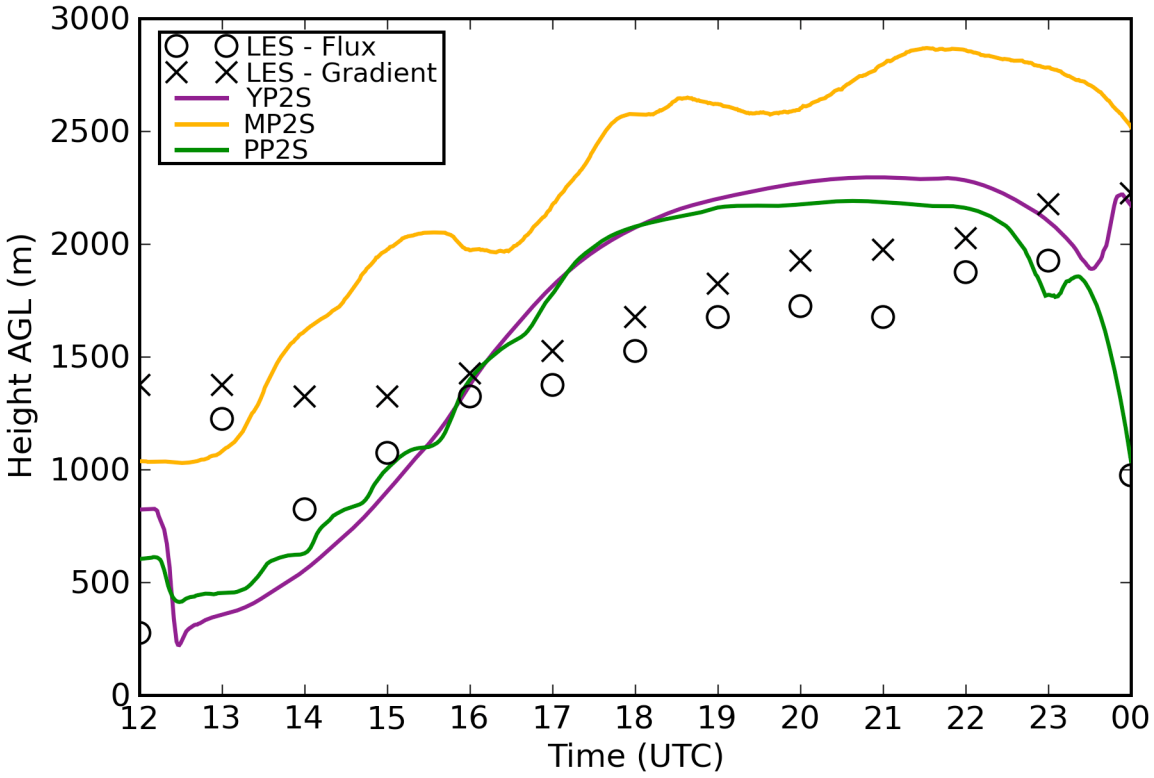

Figure 4.25: Time series of boundary layer depth (m) estimates for the entire simulation window. The flux method refers to finding the height in which virtual temperature flux reaches a minimum. The gradient method refers to finding the height in which the vertical gradient of virtual temperature reaches a maximum

Additionally, estimates of the boundary layer depth were compared in time. Owing to the noisy nature of the LES solutions in time, hourly estimates were extracted, as seen in Figure (4.25). Values represent the horizontal mean of boundary layer height estimates across the comparison domain in time. Two methods were employed to determine boundary layer depth estimates for LES solutions. The first method, hereafter the flux method, designates the boundary layer depth as the height at which the flux of virtual potential temperature reaches a minimum. For this method, horizontal averages of virtual potential temperature flux were taken at each model level. The level where these averages reached a minimum was then found. The second method, hereafter the gradient method, prescribes the boundary layer depth as the level at which the vertical gradient of virtual potential temperature becomes a maximum. For this method, horizontal averages of virtual potential temperature were taken at each model level. A simple two-point gradient approximation was employed to determine the vertical gradient at each level. The level where these estimated gradients reached a maximum was then determined. As described in (2.7.1), the YP2S configuration determines the boundary layer depth similarly to the flux method, whereas the PP2S configuration follows the gradient method, as outlined in (2.7.3). The MP2S employs a different method to determine the boundary layer depth, as summarized in (2.7.2), which is defined as the level at which the equilibrium TKE approaches a prescribed lower bound.

At the beginning of the simulation window, every WRF model solution for boundary layer depth estimations fell between the flux and gradient methods of LES. As the day continued, MP2S greatly overprescribed the boundary layer depth compared to all other solutions. This is apparently due to an internal error in the aforementioned TKE method. Until 16UTC, before turbulent motions dominated, all other configurations produced lower height estimates for the boundary layer depth as compared to the LES models. Beyond this time, WRF model solutions generally prescribed

higher boundary layer depth estimates than did LES. For all times, the flux method produced lower boundary layer heights than the gradient method. YP2S and PP2S remained fairly close until 22UTC, at which point PP2S boundary layer heights fell off dramatically. This again follows behavior mentioned previously, in which PP2S enters the stable regime at the end of the day. Overall, WRF model predictions of the boundary layer top can be summarized as being close to LES solutions at the beginning and end of the day, when more stable conditions persisted, and overestimated during the middle part of the simulation window, when turbulent motions persisted. It is important to understand the boundary layer height estimation differences at the beginning and end of the simulation window among the two methods. Generally, during these times marked with stable conditions, the flux method represents lower boundary layer height estimates than the gradient method. This is due to the fact that in the absence of strong turbulent motions, the vertical flux of virtual potential temperature will not extend as far into the vertical. During the convectively driven portion of the day, the two methods closely correlate because the vertical flux of virtual potential temperature directly affects the virtual potential temperature gradient. As the day ends, the flux is reduced, yet the gradient resulting from the turbulence driven flux remains unchanged.

Next, the quantity $-zi/L$ was investigated, where zi was taken as the depth of the boundary layer. This quantity effectively compares the contributions of shear production and buoyancy production within the depth of the boundary layer. If $|-zi/L|$ is large, then L is small, meaning that buoyancy production is dominant. Conversely, if $|-zi/L|$ is small, then L is large, meaning that shear production is dominant. In the stably stratified surface layer, if there exists non-zero turbulent shear stress, L is positive and $-zi/L$ is negative. For the unstably stratified surface layer with non-zero turbulent shear stress, L is negative and $-zi/L$ is positive.

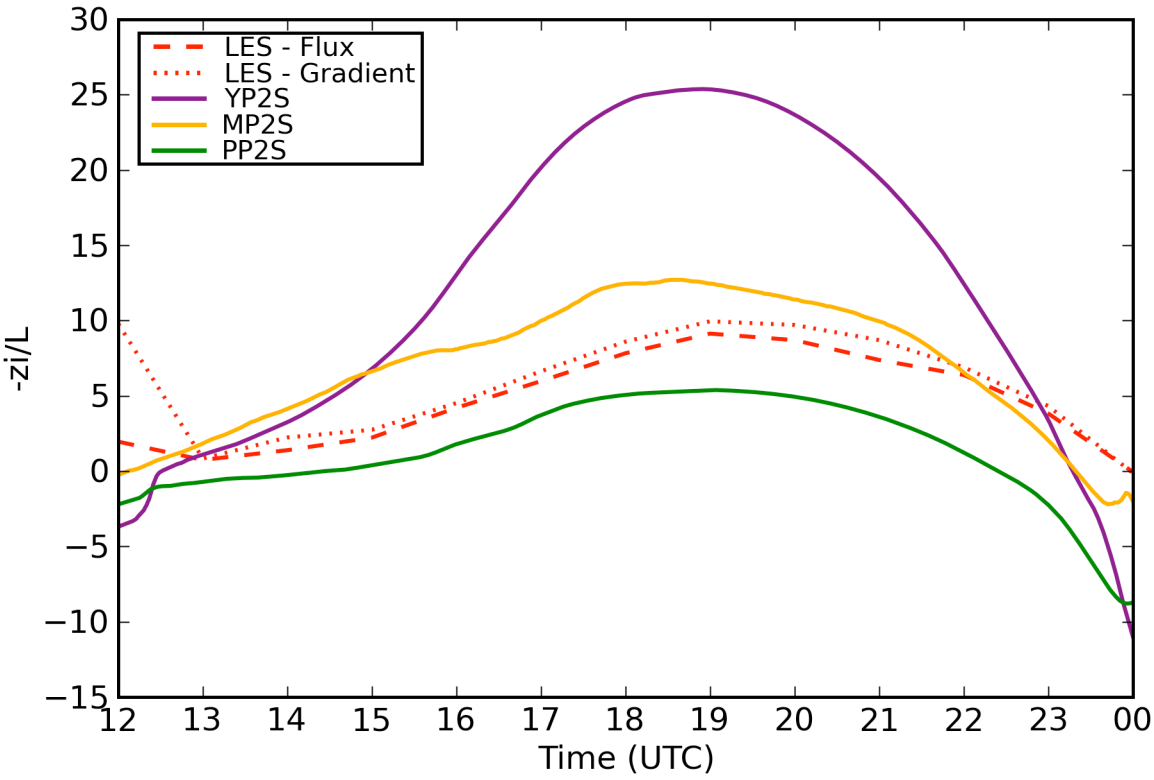

Figure 4.26: Time series of $(-zi/L)$ estimates for the entire simulation window.

Figure (4.26) illustrates the timeline evolution of $-zi/L$. All solutions remained relatively small and positive throughout the day. This indicates that shear production dominated the boundary layer evolution. PP2S predictions were consistently smaller than the LES solutions, while MP2S solutions were consistently larger, owing to it reproducing the smallest u_*. YP2S was by far the largest due to its unrealistically large θ_*. The boundary layer height overestimations by YP2S seems to confirm this behavior. As the day ended, both PP2S and YP2S dramatically reduced to negative values, which confirms the earlier supposition that PP2S produced stably stratified conditions faster than the other schemes.

4.3 Postfrontal Case

The second experimental case was taken from June 8, 2007 12UTC - June 9, 2007 00UTC. Synoptic conditions present on this date are described in detail within (4.3.1). This date was chosen based on cooler temperatures, northerly winds, and stronger static stability associated with the passage of a cold front in the overnight hours prior to the start of the simulation. Accordingly, this day is referred to as the Postfrontal Case hereinafter. Comparability of common atmospheric quantities and TTSI parameters in the WRF model with observational and fine-scale numerical simulation data are described and discussed in discussed in (4.3.2).

4.3.1 Synoptic Conditions

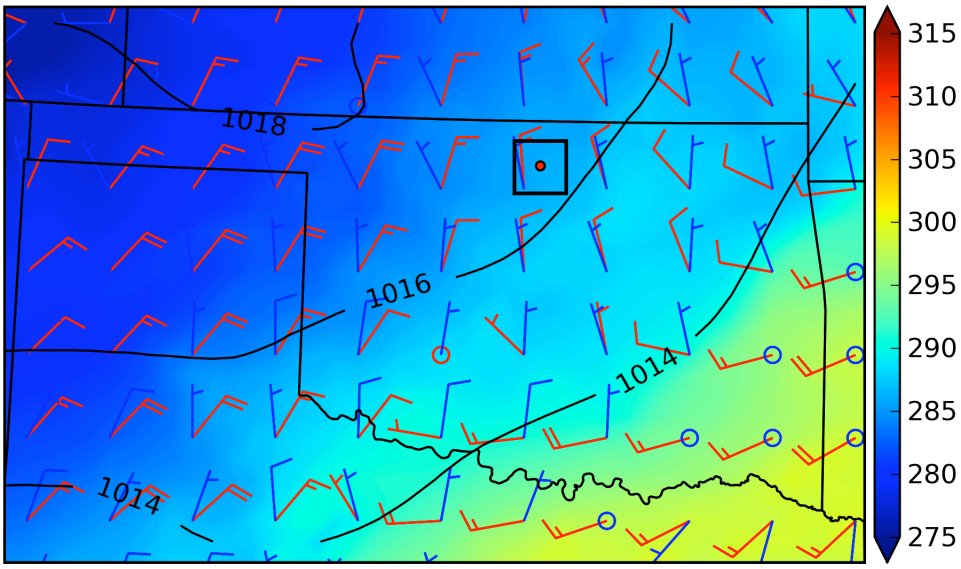

Figure 4.27: Synoptic conditions taken from RUC analyses for June 8, 2007 12UTC. Surface pressure (hPa) is the contoured quantity, surface temperature (K) is the shaded quantity, and surface winds and 850hPa winds (m/s) are the blue and red wind barbs, respectively. The black square represents the comparison domain, while the red dot depicts the location of the Lamont, Oklahoma ARM profiler site.

In the overnight hours prior to the start of the simulation, a surface high-pressure system developed in the west as the surface low-pressure system (from Dryline Case) moved northeast. As this high-pressure system progressed further southeast into Colorado, the surface cold front strengthened and began descending into Oklahoma. The winds behind the cold front shifted to northerly and storms were initiated along the leading edge. The cold front propagated beyond the comparison domain by 10UTC. By the beginning of the simulation period at 12UTC, surface winds were north northeasterly at $5 - 10\text{ms}^{-1}$. 850hPa winds were from the north at 15ms^{-1}. Subsequently, there was little directional wind shear present in the boundary layer, but speed shear was notable. Figure (4.27) depicts the synoptic conditions present at the start of the simulation window.

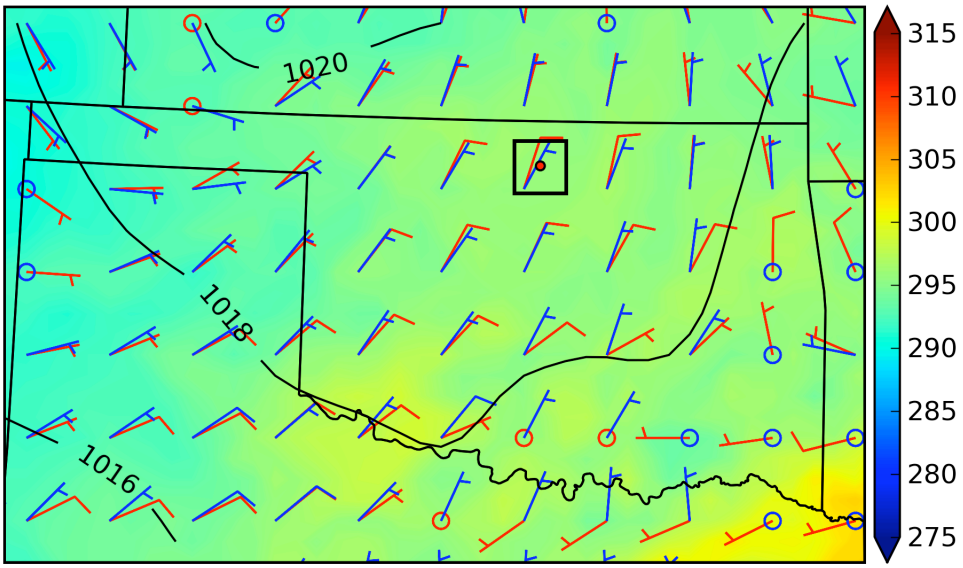

Figure 4.28: Same as Figure (4.27) but for June 8, 2007 18UTC

The surface high-pressure system continued its movement to the southeast, and by 18UTC, settled in western Kansas. The resulting surface wind field flowed from the northeast in the domain of interest,with speeds variable around 5ms^{-1}. 850hPa winds remained directionally stacked with the surface wind field, with magnitudes of 10ms^{-1}, as depicted in Figure (4.28). Accordingly, shear within the boundary layer

was very weak. Temperatures slowly warmed in the clear dry air behind the cold front, as the cold front remained southeast of the model domain.

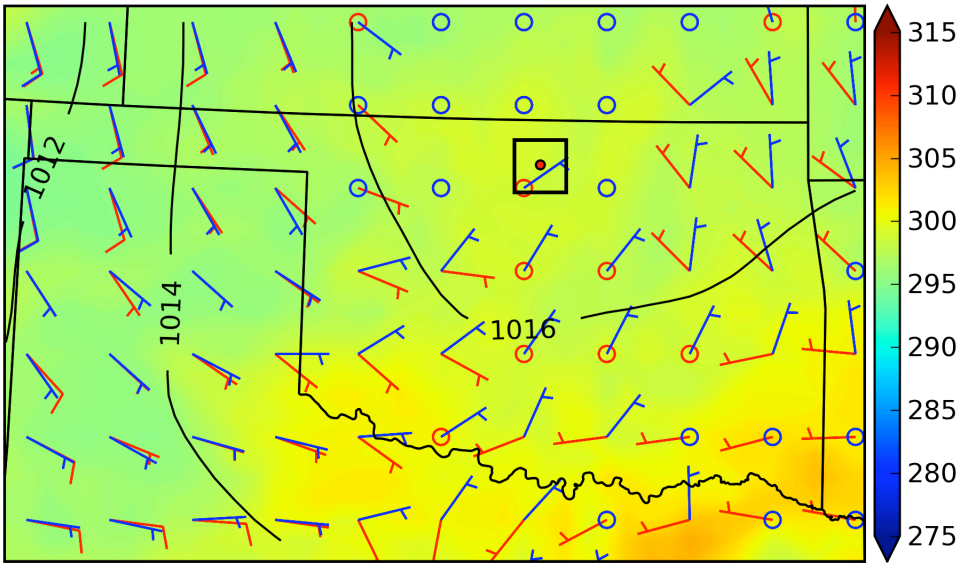

Figure 4.29: Same as Figure (4.27) but for June 9, 2007 00UTC

By the end of the simulation window at 00UTC on June 9, 2007, the surface high-pressure system expanded and encompassed the domain of interest. Subsequently, both surface and 850hPa winds were calm to 5ms^{-1} with northeasterly direction. The boundary layer was accordingly free of shear, as seen in Figure (4.29). Temperatures slowly rebounded from frontal effects and stable conditions persisted. Surface pressure decreased slightly to between 1016 and 1018hPa.

This case date was appropriate as the simulation window encompassed a post cold front environment, in which dry, stable conditions persisted and winds weakened throughout the day. This provides a good study of the model's ability to depict a postfrontal environment and its evolution throughout the day in terms of the wind field and heating. The conditions present in the case are classified as temporally inhomogeneous.

4.3.2 Results

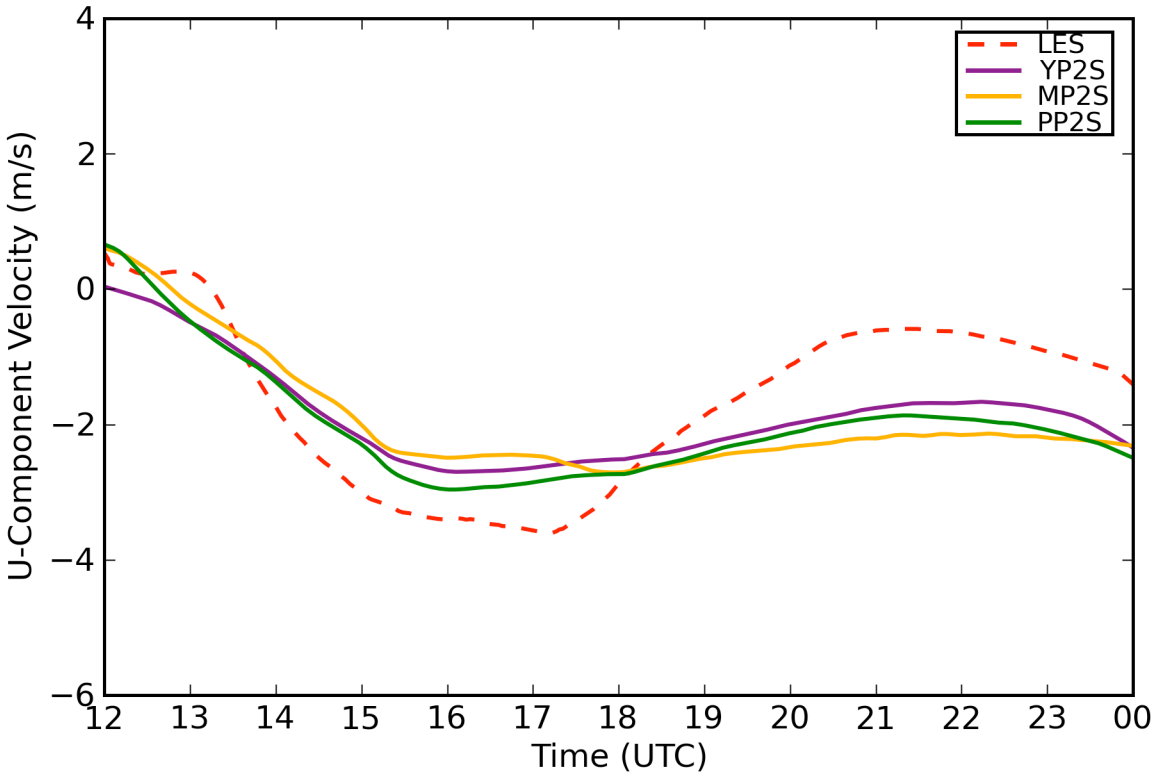

Figure 4.30: Time series of 25m u-component velocity (m/s) for the entire simulation window. Values represent the horizontal planar average taken across the comparison domain.

Following comparisons in the Dryline case, as outlined in (4.2.2), timeline series of basic atmospheric quantities were contrasted for the Postfrontal Case. Results were then plotted over the entire simulation window, from June 8, 2007 12UTC to June 9, 2007 00Z. The first quantity compared was u-component velocity (ms^{-1}), as illustrated in Figure (4.30). Initially, the 12h forecast from all WRF model configurations matched well with LES. As expected, based on the synoptic conditions present during the simulation window, winds gained a easterly component following the passage of the cold front. As the day progressed, u-component wind velocity steadily grew

stronger from the east as the high pressure system approached the comparison domain from the west, reaching a maximum near 17UTC. Every WRF model configuration followed nicely with the LES solutions, although the magnitude of the peak u-component velocity was underrepresented. Further in the simulation window, LES solutions predicted weakening and variable wind as the surface high pressure system moved directly over the comparison domain. Every WRF model solution set failed to reproduce such weakening to the extent seen in the analyses, but all were close in magnitude to each other. The YP2S and PP2S configurations followed closest throughout the simulation window. MP2S generally differed the greatest from the LES predictions.

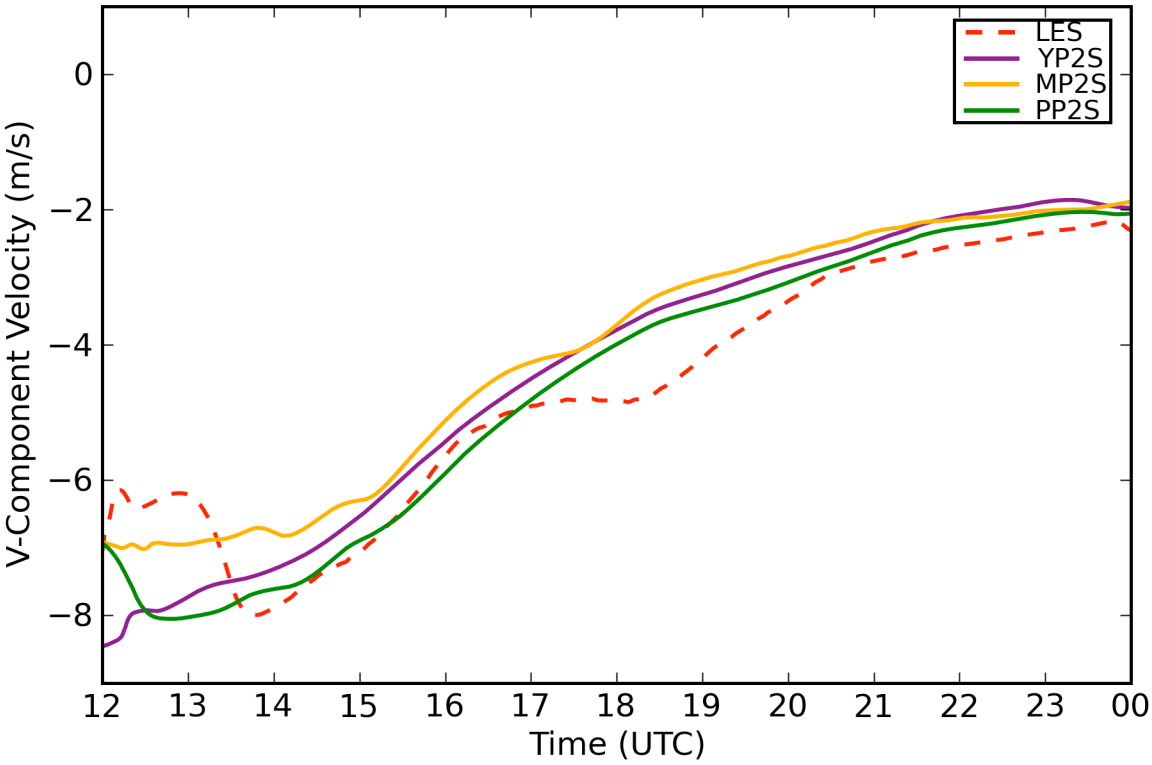

Figure 4.31: Time series of 25m v-component velocity (m/s) for the entire simulation window. Values represent the horizontal planar average taken across the comparison domain.

The next quantity compared was v-component velocity (ms^{-1}), shown in Figure (4.31). Initially, MP2S and PP2S configurations provided the best 12h forecast as compared against the LES initial fields. As expected, the v-component wind velocity was from the north. The LES solutions again experienced model spin-up issues in the first hour or two. After 14UTC, all solutions matched closely with the LES predictions, exhibiting a gradual decrease in magnitude throughout the day, as the surface high pressure system moved into the comparison domain from the west. YP2S and PP2S configurations reproduced the smallest deviations from LES, while MP2S underestimated the v-component velocity by the largest margin throughout the entire simulation window.

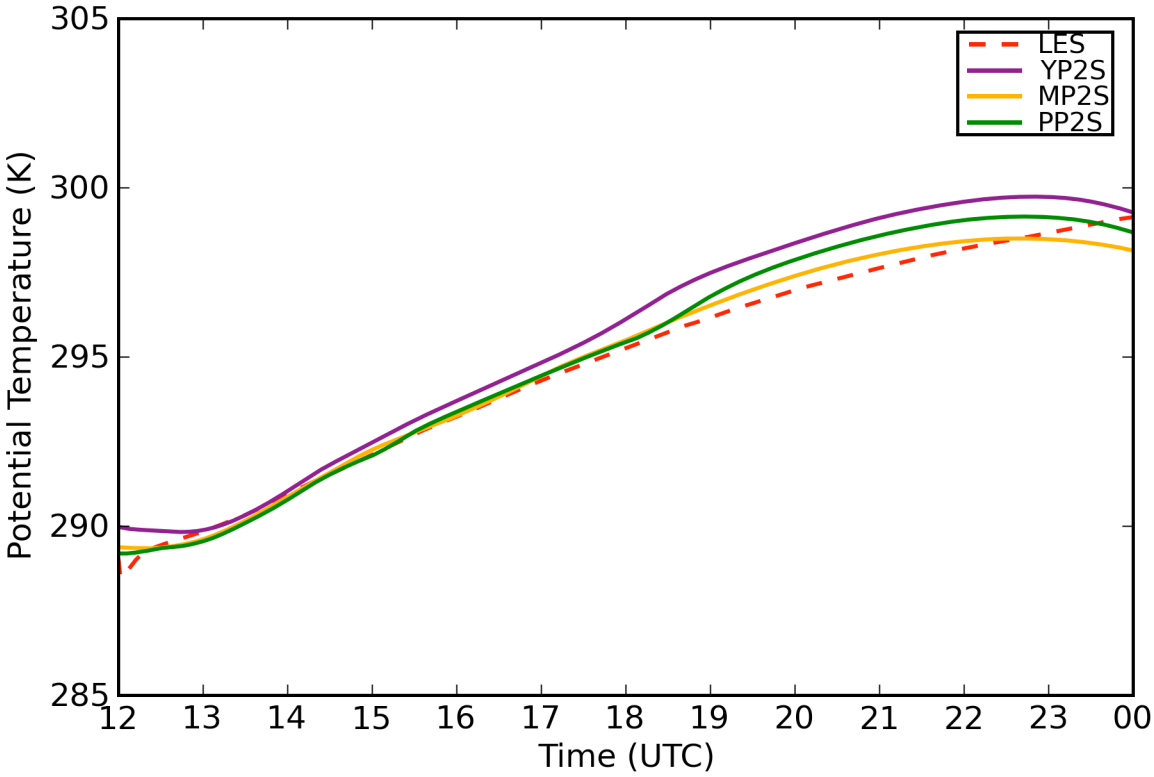

Figure 4.32: Time series of 25m potential temperature (K) for the entire simulation window. Values represent the horizontal planar average taken across the comparison domain.

Additionally, potential temperature (K) was compared. The 12h forecast for every WRF model option was within 1K of LES, with MP2S and PP2S being the closest. When comparing potential temperature to that observed in the Dryline Case, Figure (4.7), it is evident that the cold front resulted in a 24h decrease on the order of 10K. Every WRF model configuration warmed compared to LES between 17UTC and 22UTC, after which WRF model predictions cooled faster than LES. Generally, MP2S and PP2S followed the closest to LES solutions, with YP2S the furthest away.

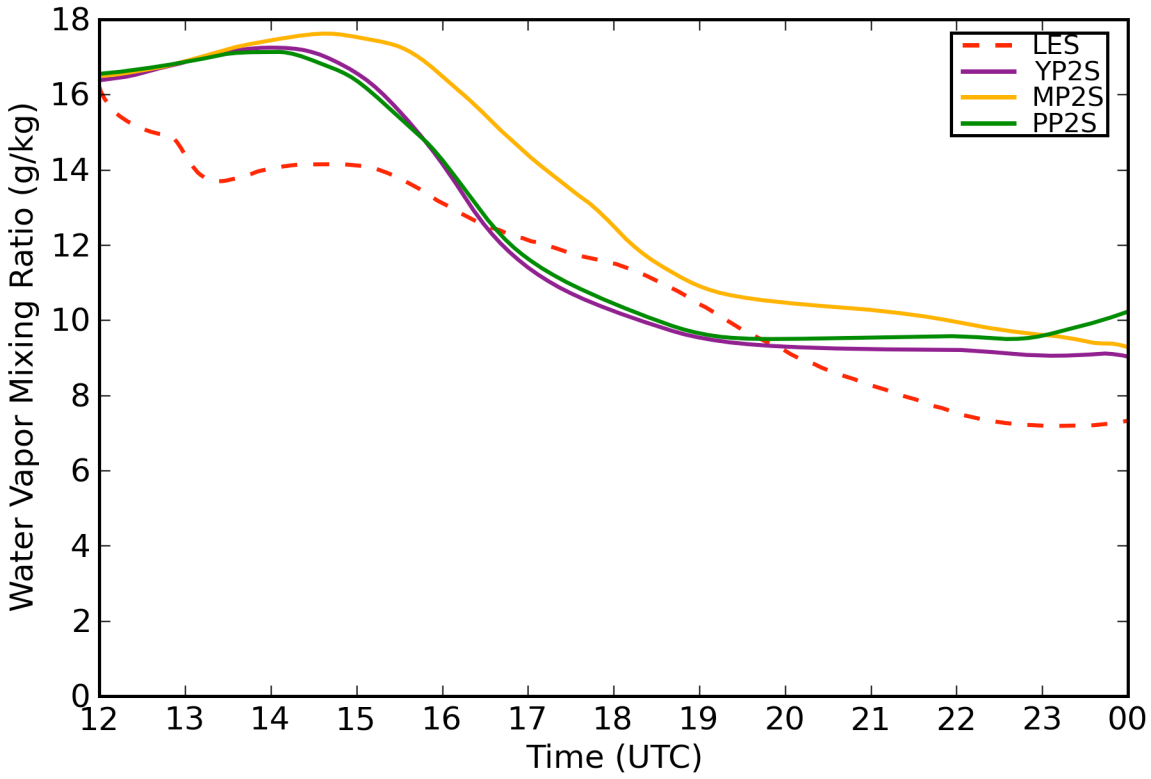

Figure 4.33: Time series of 25m water vapor mixing ratio (g/kg) for the entire simulation window. Values represent the horizontal planar average taken across the comparison domain.

Finally, water vapor mixing ratio (gkg^{-1}) was compared. As illustrated in Figure (4.33), after the first hour all WRF model predictions produce greater moisture values than did LES, except for YP2S, which matched LES solutions from 19UTC to the

end of the simulation window. MP2S differed the greatest from LES throughout the entire simulation window. This behavior would seem to indicate the potential for larger latent heat effects in the WRF model solutions, although not by as much as was seen in the Dryline Case. Overall, YP2S and PP2S best match the LES predictions for water vapor mixing ratio.

Again, following (4.2.2), vertical representations of atmospheric quantities were investigated by taking horizontal planar averages at each respective model level, with such means for the WRF model being vertically interpolated to the physical levels contained within LES. It is important to understand that the method used for comparison restricts the interpretation of results to that which is statistical in nature, offering no spatial determination of forecast skill.

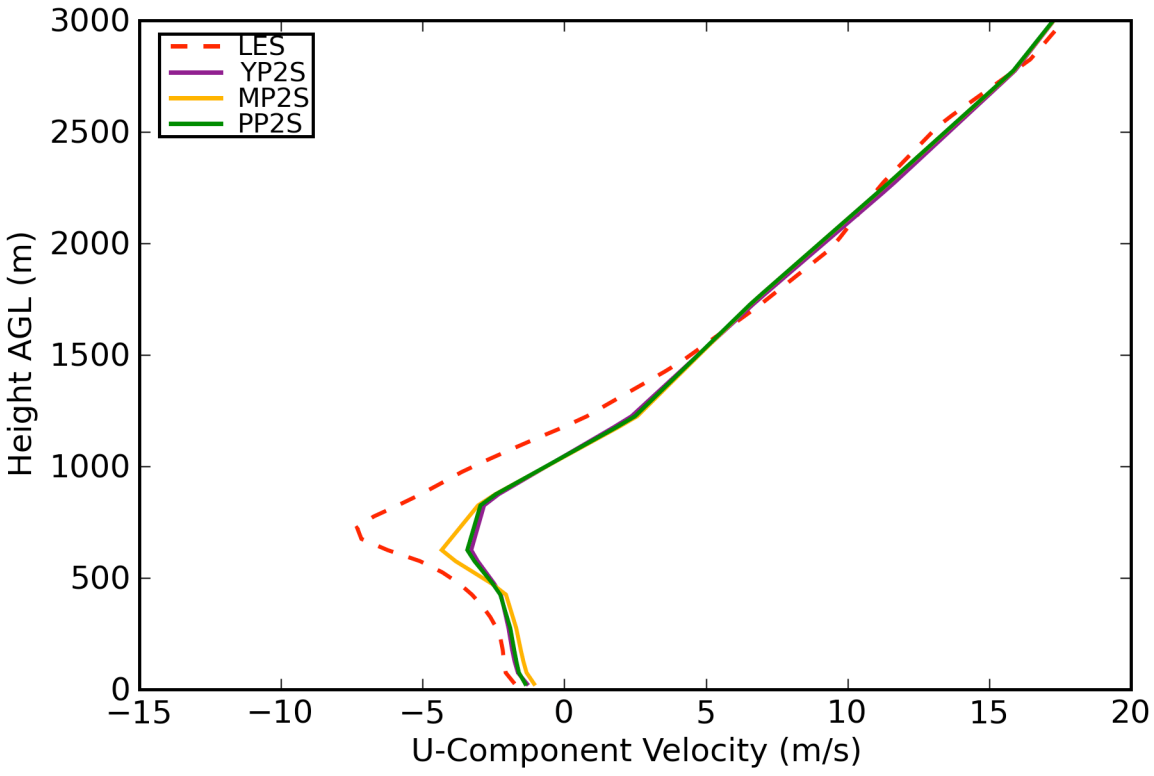

Figure 4.34: Vertical profile of u-component velocity (m/s) for June 8, 2007 14UTC. Values at each level represent the horizontal planar average taken across the comparison domain.

Firstly, the vertical structure of u-component velocity was examined. Figure (4.34) depicts such structure for 14UTC. Near-surface u-component velocity was nearly equivalent for all WRF model configurations, indicating that the model had a good handle on the wind field morphology following the frontal passage during the overnight hours. Solutions from all WRF model configurations represented smaller vertical wind shear in the surface layer when compared with LES predictions. While the vertical placement of the low-level jet was accurately approximated by the WRF model, the magnitude was underpredicted. MP2S came closest to matching the magnitude of the low-level jet prescribed in LES. Above the low-level jet, WRF model solutions were nearly equivalent and followed closely with LES. Overall, each solution was in general good agreement with the LES predictions for u-component velocity.

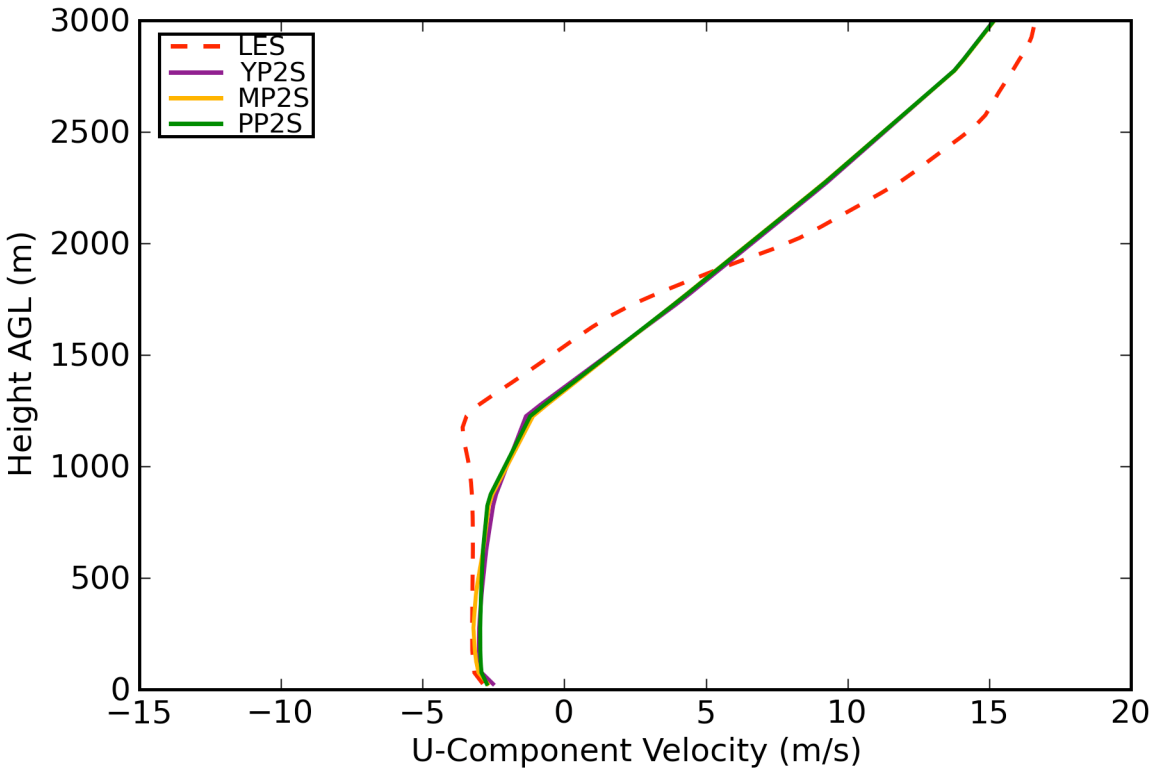

Figure 4.35: Same as Figure (4.34) but for June 8, 2007 18UTC.

In the middle of the simulation window, as seen in Figure (4.35), the 18UTC u-component wind speed profiles offered a few more differences than those found at 12UTC. LES solutions represent greater vertical mixing than seen in the WRF model predictions. Near-surface values follow closely with that of the LES solutions, with WRF model predictions offering slightly smaller surface layer shear. Every WRF model configuration reproduced a slightly shallower well-mixed layer, although the general behavior matched well with LES solutions. Above the well-mixed layer, LES simulated a slightly larger vertical gradient of u-component velocity than any of the WRF model predictions. Overall, the differences among WRF model predictions were not easily discernible. Both models demonstrate a linear increase in u-component velocity with height.

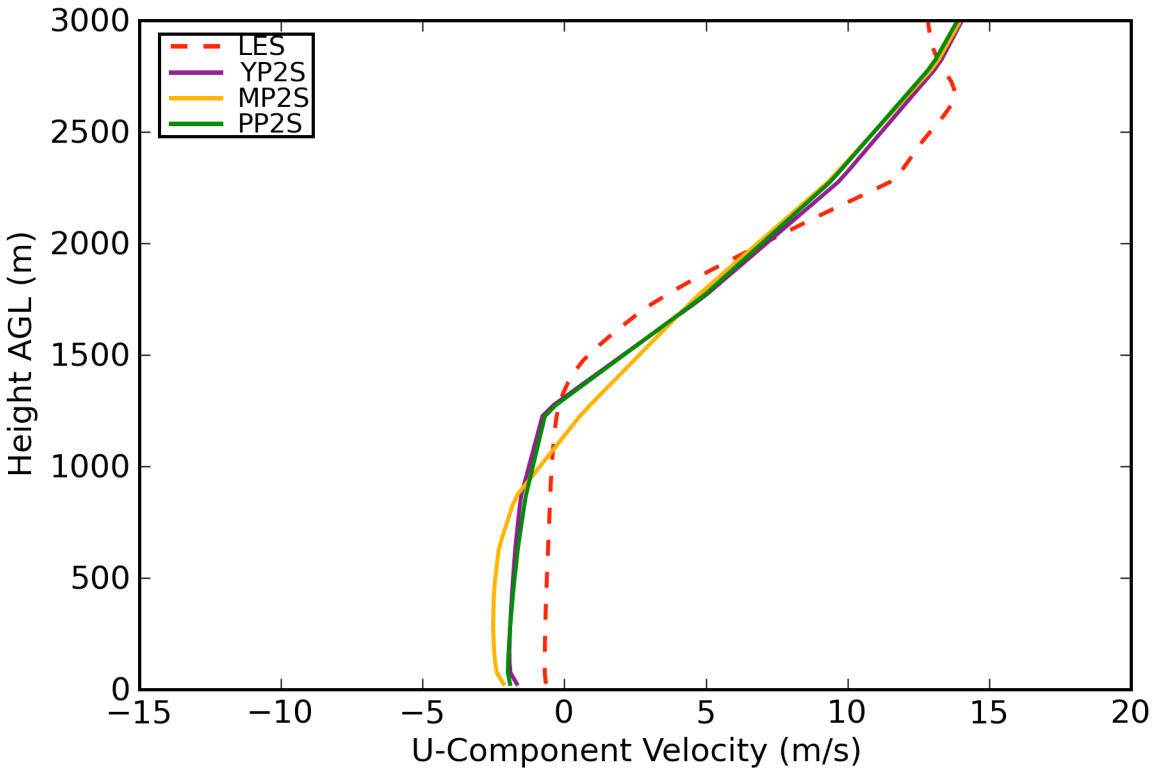

Figure 4.36: Same as Figure (4.34) but for June 8, 2007 22UTC.

Toward the end of the simulation window, notable differences existed in the vertical structure of the u-component velocity, as seen in Figure (4.36). WRF model predictions did not exhibit the reduction of wind speed as did LES. The MP2S configuration offered the shallowest well-mixed layer and largest magnitude of u-component velocity. YP2S and PP2S were not easily distinguishable from each other and produced a more realistic well-mixed layer depth to that prescribed by LES. Again, WRF model configurations did not reproduce as strong a vertical gradient in u-component velocity above the well-mixes layer as that in the LES profile, although they converged to consistent predictions.

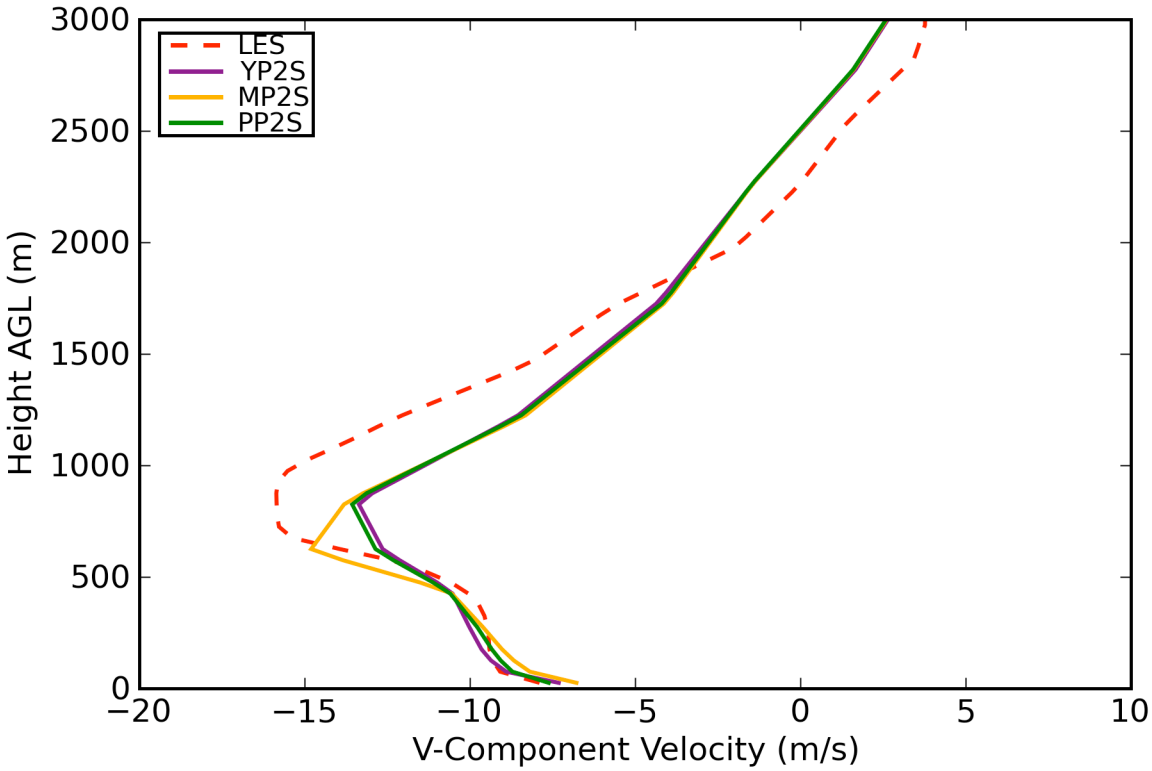

Figure 4.37: Vertical profile of v-component velocity (m/s) for June 8, 2007 14UTC. Values at each level represent the horizontal planar average taken across the comparison domain.

Secondly, the vertical structure of v-component wind velocity was examined. Figure (4.37) illustrates this structure for 14UTC. Near-surface values were very close

between each model, with the LES profile exhibiting stronger surface layer shear. The WRF model solutions realistically predicted the level of the the low-level jet, but underprescribed the magnitude of the jet. MP2S again was the closest in predicting the magnitude of the low-level jet. Above the jet, WRF model predictions successfully replicated the behavior demonstrated in the LES solutions, but with a smaller vertical gradient.

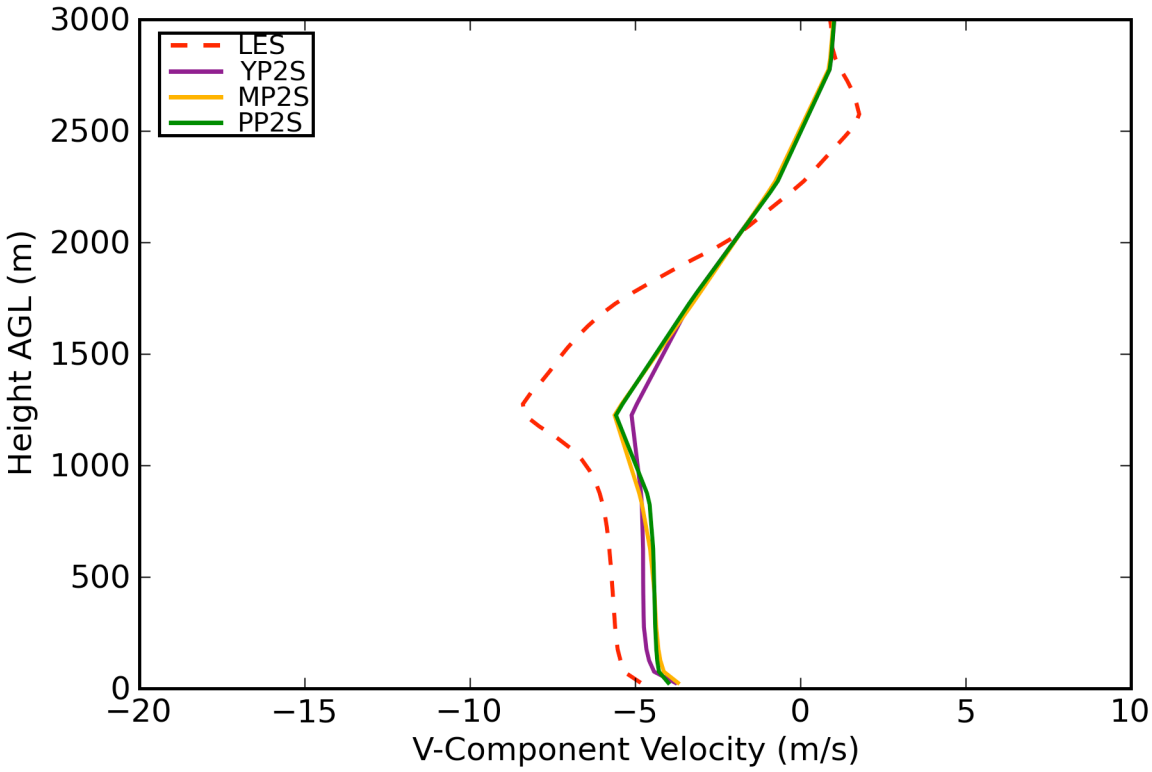

Figure 4.38: Same as Figure (4.37) but for June 8, 2007 18UTC.

At 18UTC, as seen in Figure (4.38), near-surface v-component wind velocities amongst separate model solutions were smaller in the WRF model. All WRF model predictions accurately demonstrated the depth of the well-mixed layer. While the level of the v-component velocity maximum was realistically predicted in each WRF

model configuration, the magnitude was underrepresented. While the general behavior above the wind maximum is consistent amongst all WRF model solutions, the LES predictions illustrate a larger vertical gradient in v-component wind velocity.

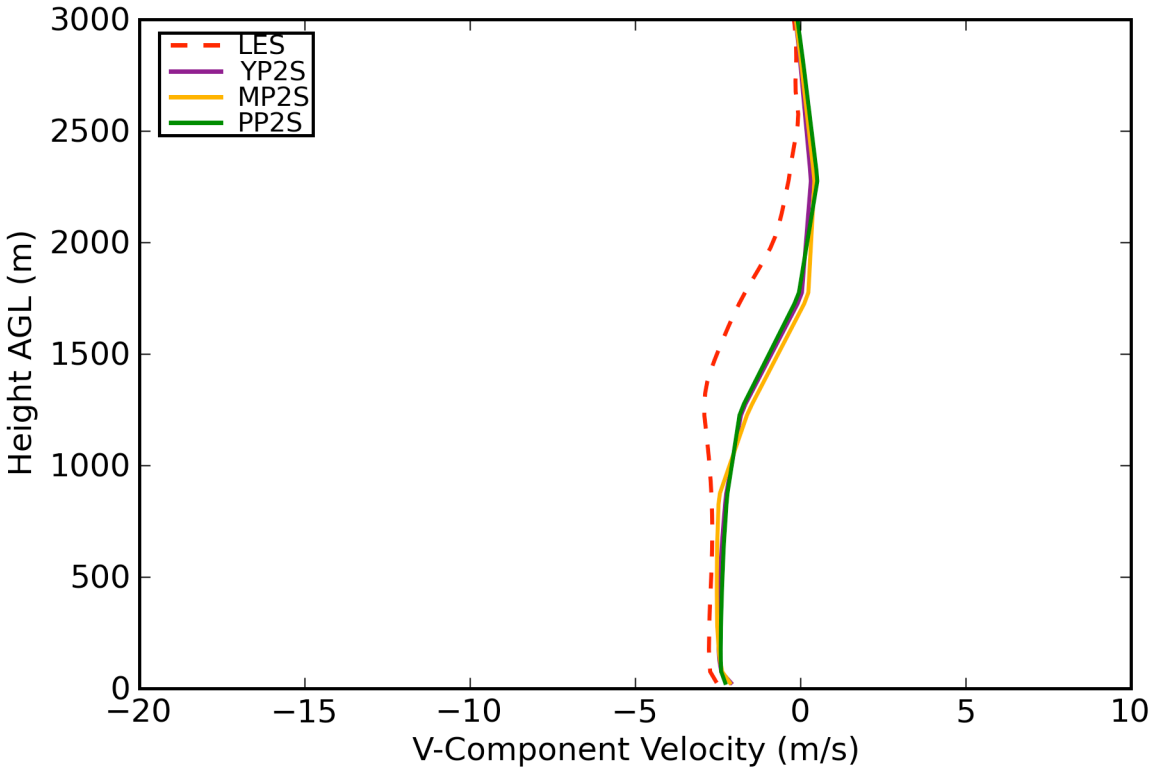

Figure 4.39: Same as Figure (4.37) but for June 8, 2007 22UTC.

Vertical profiles of v-component wind velocity taken near the end of the simulation window, as depicted in Figure (4.39), were consistent among all WRF model predictions, but produced a shallower well-mixed layer than did LES. While generally reproducing the same vertical flow features above this layer, the WRF model solutions did not adequately reproduce the vertical gradient changes evident in the LES solutions. Again, it appears that LES is more adept at reproducing atmospheric flow features associated with the top of the boundary layer and entrainment zone than the parameterization schemes present in the WRF model.

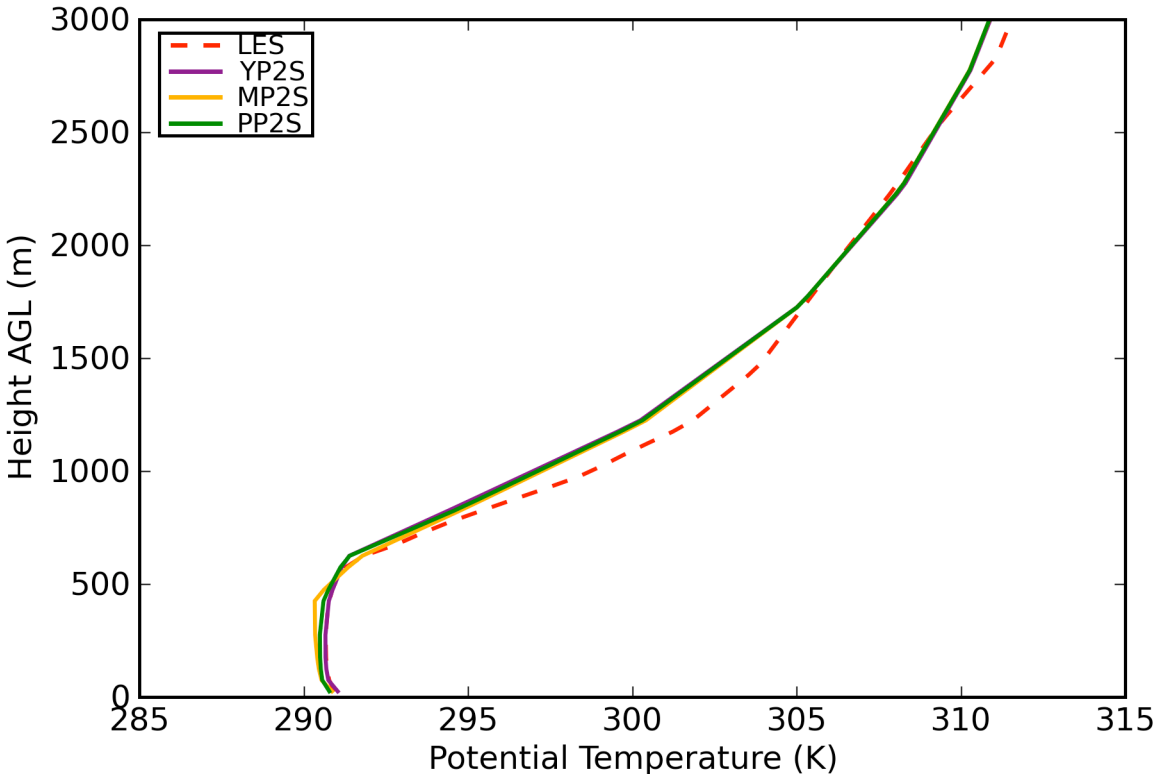

Figure 4.40: Vertical profile of potential temperature (K) for June 8, 2007 14UTC. Values at each level represent the horizontal planar average taken across the comparison domain.

Additionally, the vertical nature of potential temperature was investigated. Figure (4.40) represents the vertical profiles of potential temperature at 14UTC. As seen in Figure (4.32), the predictions from the WRF model were within 1K in the SL for the initial few hours of the simulation window, Above the SL, behavior was nearly consistent between all WRF model solutions, except MP2S, which produced slightly less vertical mixing. Above the well-mixed layer, an initially strong capping inversion existed as would be expected following a cold frontal passage. In general, all WRF model predictions closely followed the LES solutions.

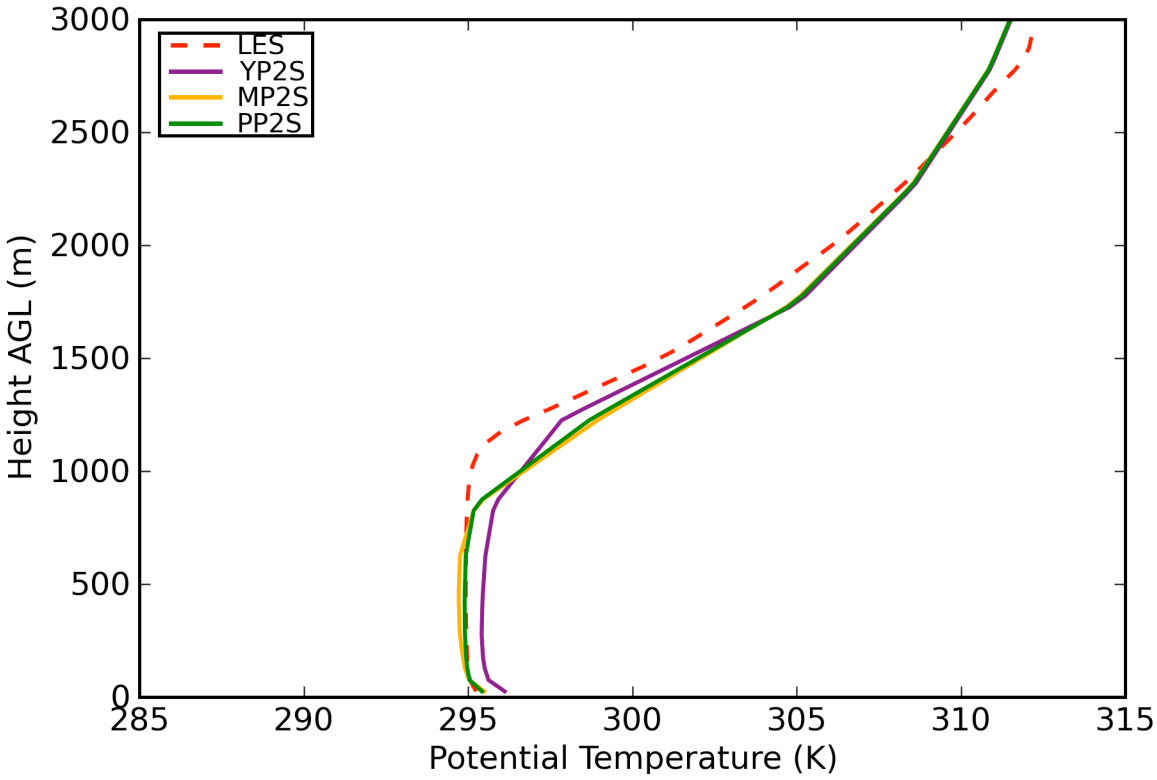

Figure 4.41: Same as Figure (4.40) but for June 8, 2007 18UTC.

As illustrated in Figure (4.41), the WRF model predictions for potential temperature remained close to the LES solutions. MP2S and PP2S configurations were closest near-surface in magnitude, with YP2S being the furthest away. Every WRF model prediction demonstrated a shallower well-mixed layer compared to the LES solutions. While magnitudes differed, the height of the well-mixed level matched closely between each WRF model configuration. Above the well-mixed layer, behavior was nearly equivalent in nature among all model solutions.

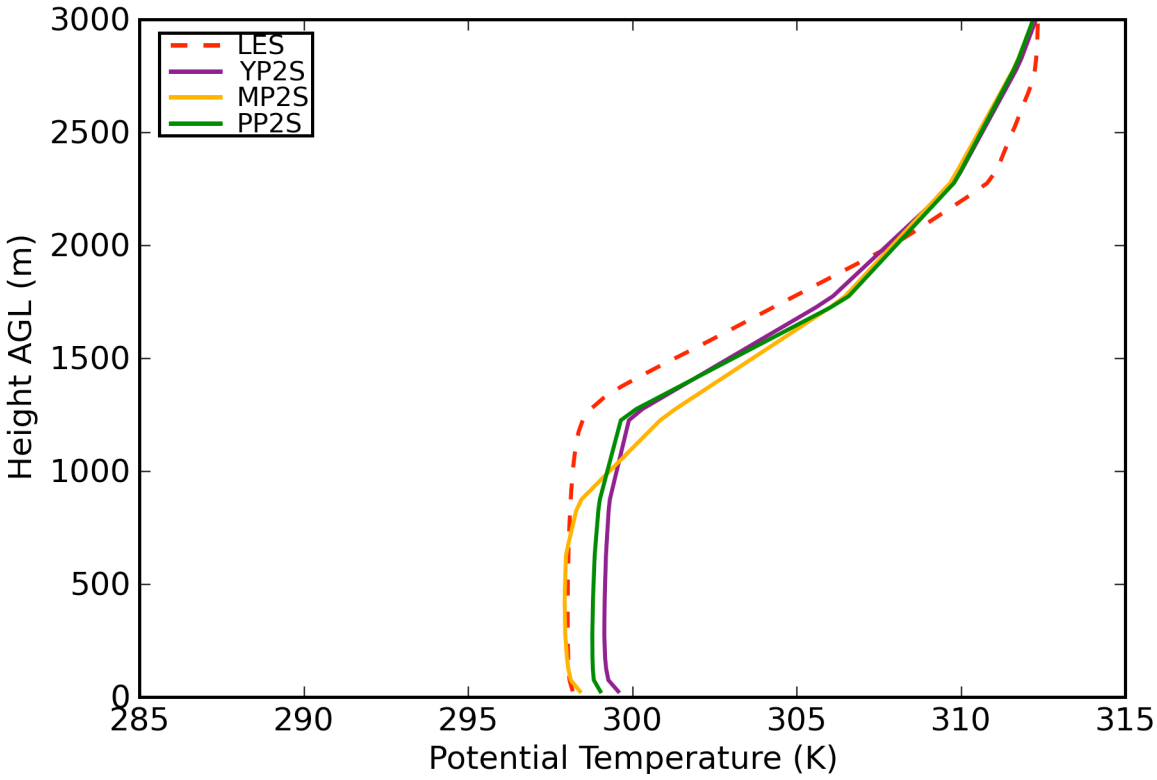

Figure 4.42: Same as Figure (4.40) but for June 8, 2007 22UTC.

Toward the end of the simulation window, nearly all of the WRF model configurations reproduced overestimated values of near-surface potential temperature, with the exception of the MP2S configuration, as seen in Figure (4.42). However, MP2S reproduced the shallowest well-mixed layer of any WRF model prediction. While magnitudes were slightly larger, the YP2S and PP2S configurations were nearly identical in nature to the LES solutions throughout the extent of the well-mixed layer, even accurately reproducing the depth of the mixed layer. Above the well-mixed layer, behavior was consistent between both models, although LES produced a stronger vertical gradient.

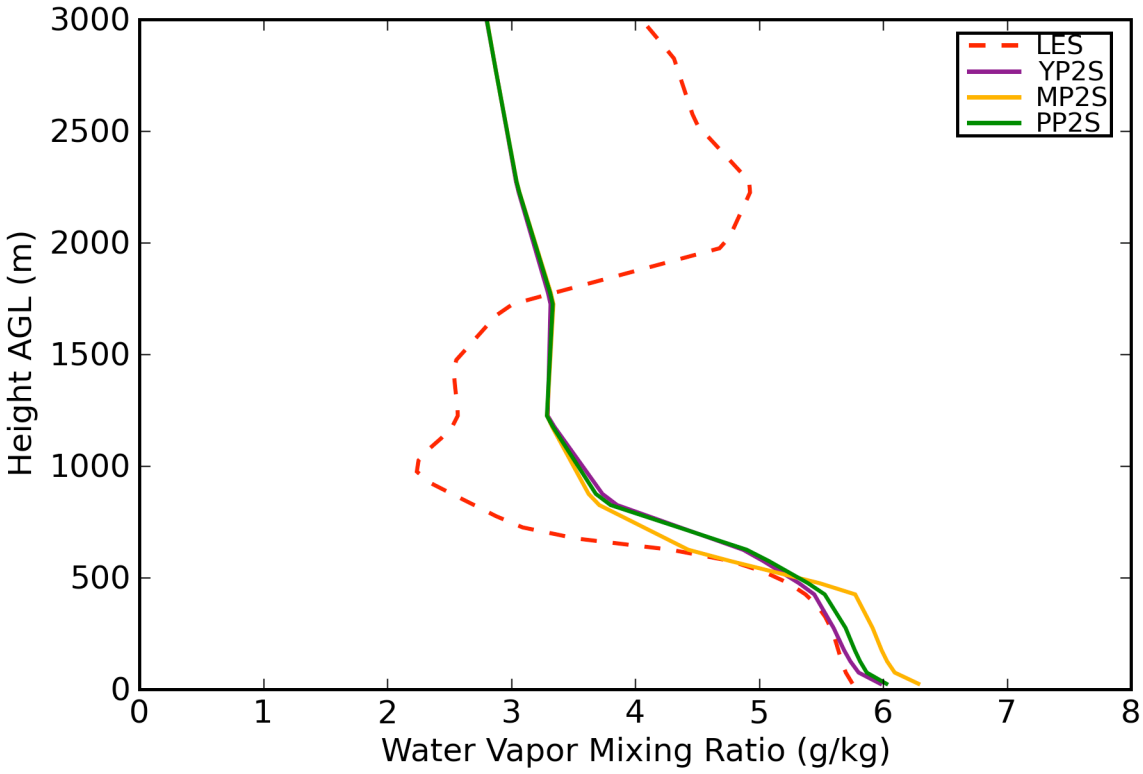

Figure 4.43: Vertical profile of water vapor mixing ratio (g/kg) for June 8, 2007 14UTC. Values at each level represent the horizontal planar average taken across the comparison domain.

Finally, water vapor mixing ratio was examined in the vertical, as illustrated in Figure (4.43). Within the well-mixed layer, all WRF model configurations depicted a considerably more moist atmosphere. Vertical mixing effects were equivalent between both models. Both PP2S and YP2S solutions were similar to LES, with MP2S reproducing more moisture. Above the well-mixed layer, the vertical gradient of moisture was nearly identically produced by both the WRF model and LES. Above this strong gradient, it appears that LES once again reproduced entrainment effects. While the WRF model profiles showed a nearly gradual and uniform shape, the LES profile

became sharply drier, then switched to more moist with height. This elevated positive moisture gradient may represent the overturning associated with entrainment processes.

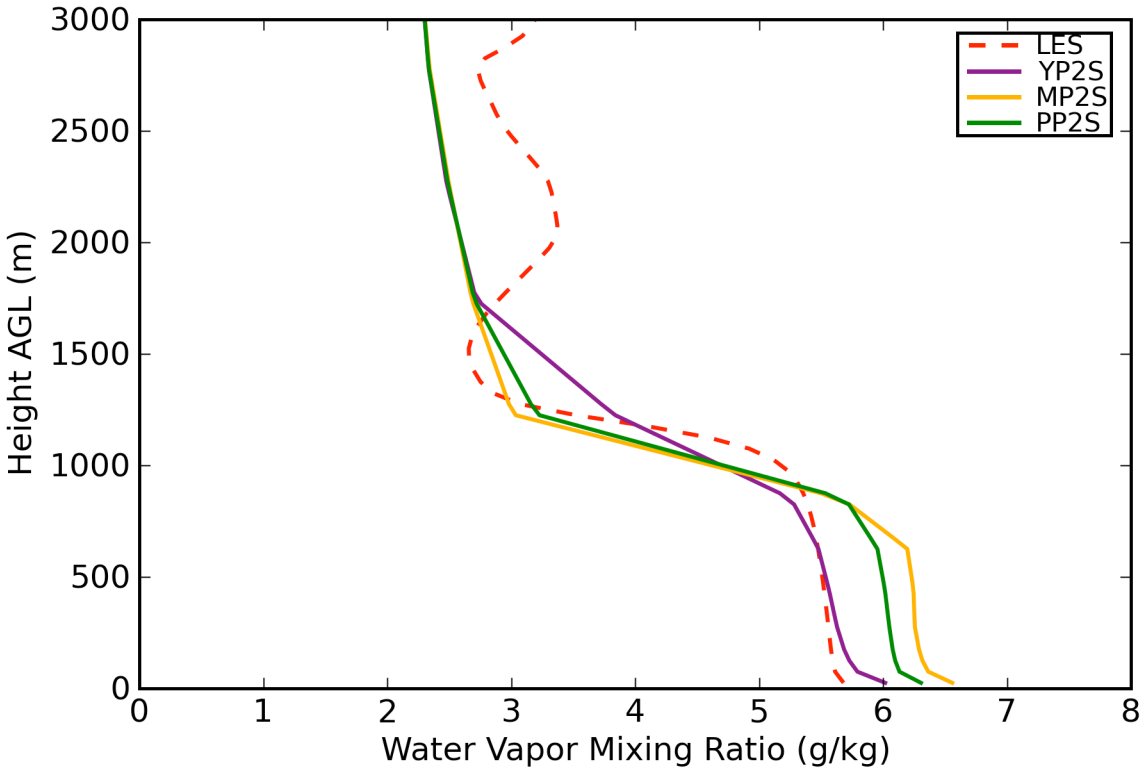

Figure 4.44: Same as Figure (4.43) but for June 8, 2007 18UTC.

Figure (4.44) illustrates the vertical profile of moisture at 18UTC. At this time, further mixing resulted in drier surface moisture values. All WRF model predictions reproduced a weaker well-mixed layer. YP2S was closer in magnitude to LES, while PP2S and MP2S modeled slightly more moist conditions than LES. Above the strong negative moisture gradient, LES again reproduced a positive vertical gradient, most likely from entrainment processes. Oppositely, WRF model predictions reproduced a gradual decrease in moisture with height. Stronger latent heat effects in the WRF model predictions should be expected based on these profiles

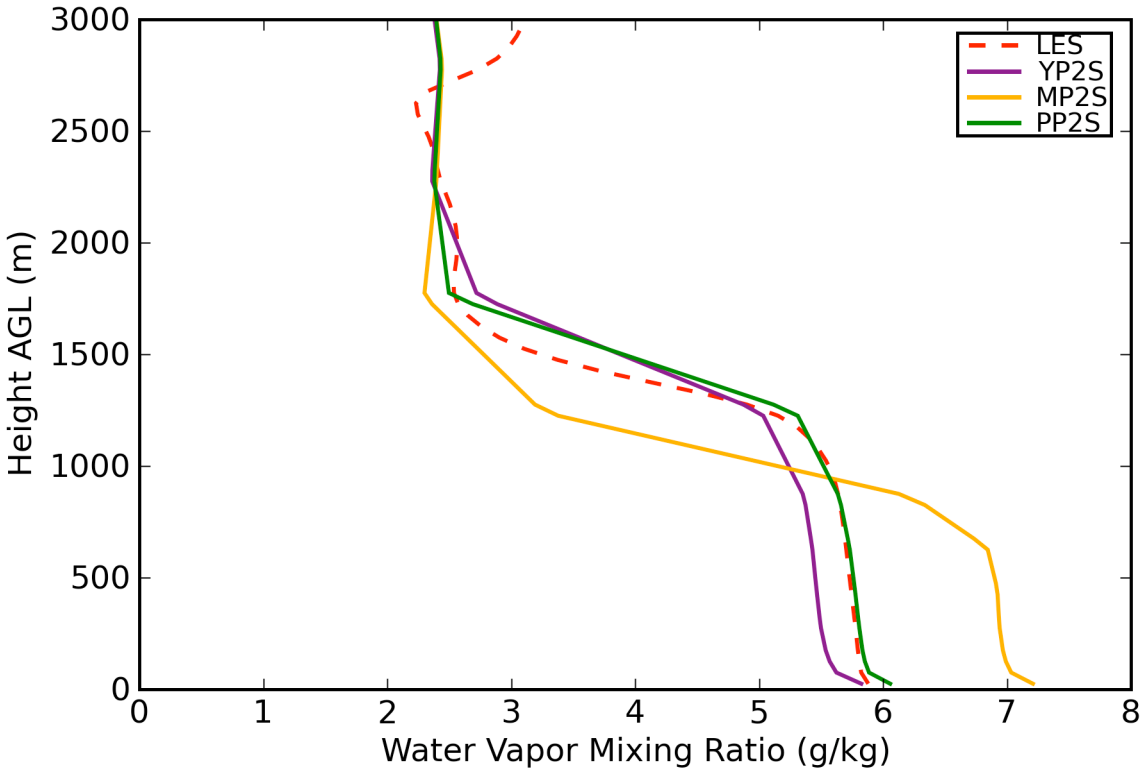

Figure 4.45: Same as Figure (4.45) but for June 8, 2007 22UTC.

At 22UTC, WRF model solutions closely followed the vertical structure of the LES predictions, as seen in Figure (4.45). MP2S produced a markedly more moist and shallower well-mixed layer than the other WRF model configurations. PP2S nearly matched the magnitude and depth of the well-mixed layer as that prescribed by the LES profile exactly. YP2S reproduced similar well-mixed layer behavior to that as LES, but was slightly drier. Above the layer of strong negative moisture gradient, the LES profile again showed the effects of entrainment, while each of the WRF predictions prescribed a gradually decreasing moisture profile with height.

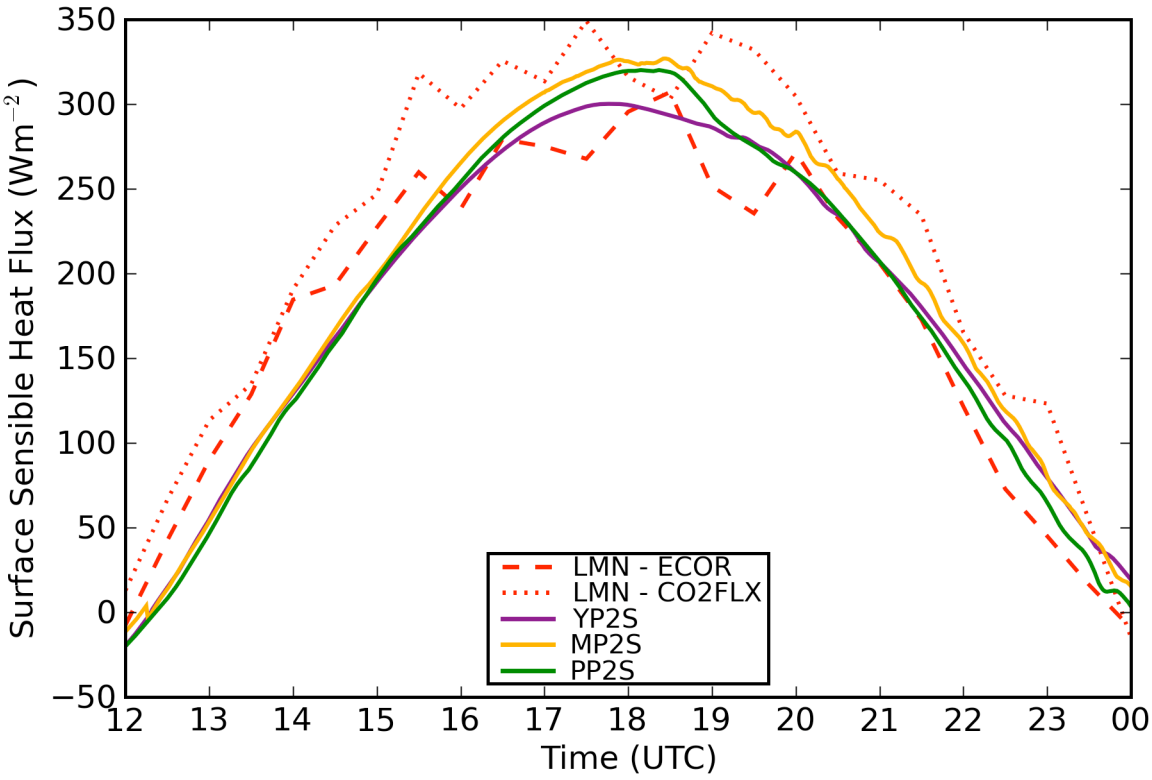

Figure 4.46: Time series of surface heat flux (Wm^{-2}) for the entire simulation window. Values represent the horizontal planar average taken across the comparison domain.

As outlined in (4.2.2), following the examination of basic first-order atmospheric quantities, higher-order turbulence statistics were compared between LES and the WRF model configurations. The first such higher-order turbulence term inspected was the surface sensible heat flux (Wm^{-2}), which is given by Eq. (4.1). Again, it is important to note that the surface heat flux in LES represents prescribed values at a single point in space and time from the LMN ARM site, which are uniformly applied across the entire comparison domain. Oppositely, the WRF model values represent predicted values at each grid point averaged in the horizontal plane. The WRF model has knowledge of geographic land use through static geographic data and the LSM, whereas LES relies on a single point measurement. As discussed in the Dryline Case, little change occurred when taking the predicted values at the grid-cell nearest to the

LMN measurement site as compared to taking a horizontal average. Surface sensible heat flux values are plotted in Figure (4.46).

Again, The ECOR and CO2FLX measurements were used to compare with the WRF model solutions. Magnitudes between measurements and those from all WRF model solutions remained close throughout the entire simulation window. From the simulation start to 16UTC, every WRF model configuration reproduced slightly underestimated surface sensible heat flux values. Between 16UTC and 20UTC, WRF model predictions were slightly larger than the ECOR measurements and slightly smaller than the CO2FLX measurements. MP2S produced the largest sensible heat flux and YP2S produced the smallest. Beyond 20UTC, values were nearly equivalent between model predictions and measurements.

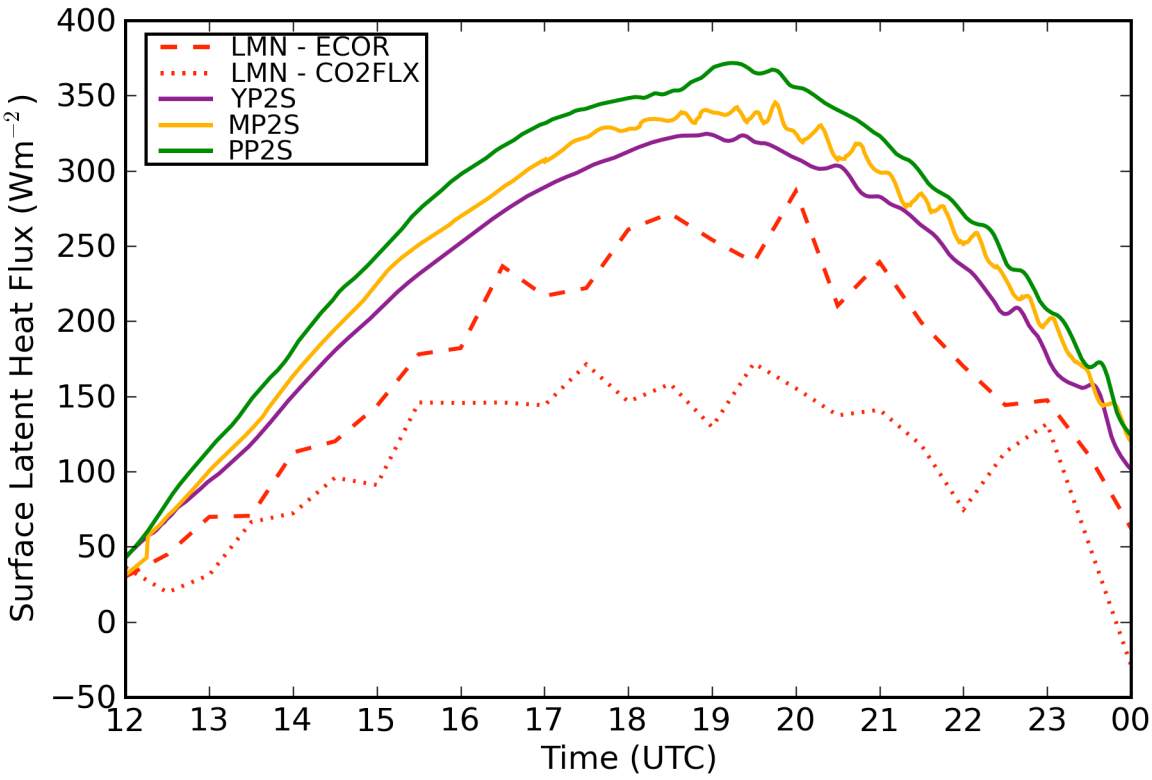

Figure 4.47: Time series of surface latent heat flux (Wm^{-2}) for the entire simulation window. Values represent the horizontal planar average taken across the comparison domain.

Time series analysis was also performed for the surface latent heat flux (Wm^{-2}), which is given by Eq. (4.2), as illustrated in Figure (4.47). Similar to results shown in Figure (4.22), surface latent heat flux was overpredicted across all model configurations throughout the entire simulation window, when compared to the ECOR and CO2FLX measurements. The YP2S configuration was the closest to LES solutions and PP2S overprescribed such values by the largest margin. The flux behavior seen in this case was the same to that in the Dryline Case, where surface sensible heat flux was generally underestimated and surface latent heat flux was overprescribed.

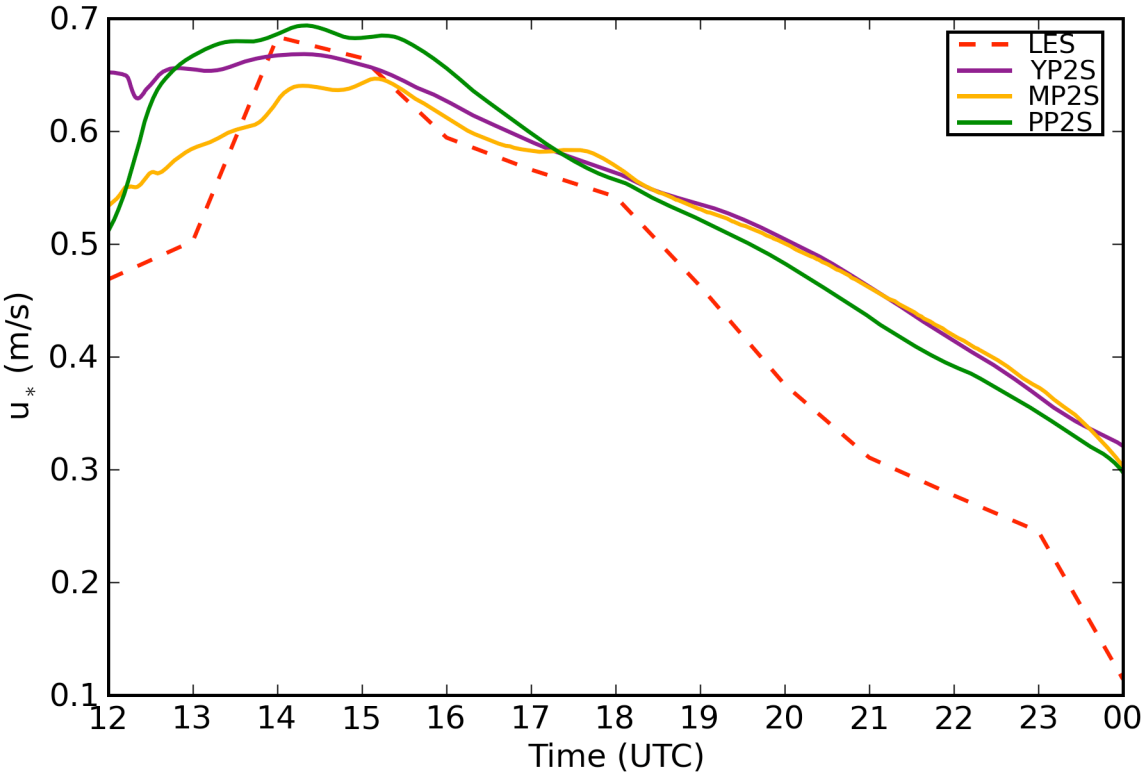

Figure 4.48: Time series of u_* (m/s) for the entire simulation window.

One important parameter from similarity theory is the turbulence velocity scale, or friction velocity (u_*), given by Eq. (2.1a). Figure (4.48) illustrates the horizontally averaged friction velocity for both LES and WRF model solutions. Both models exhibit a gradual increase in the early portion of the simulation, followed by a linear

decrease for the remainder of the simulation window. In the first half of the simulation window, WRF model configurations followed the friction velocity prescribed by LES rather closely. As the end of the day was approached, the friction velocity predicted in the WRF model was overprescribed compared to that from LES. Such behavior was evident when looking at the horizontal velocity components in which WRF values failed to reduce toward the end of the simulation window as was done in the LES solutions.

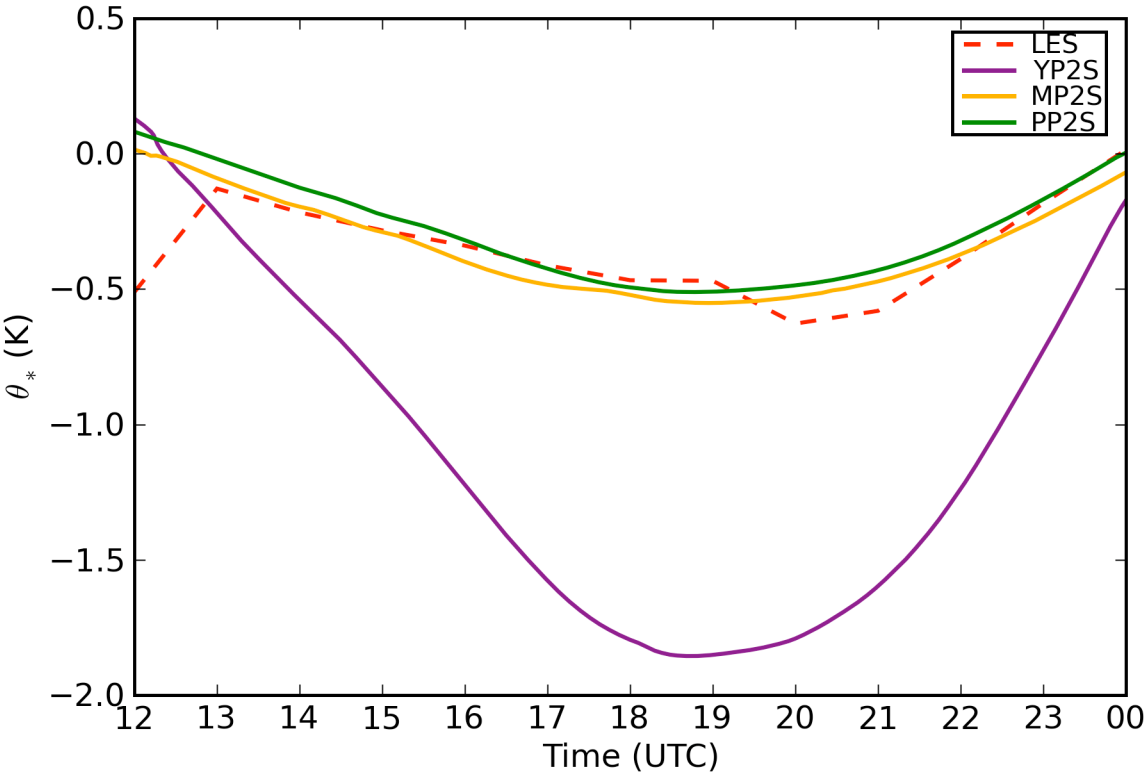

Figure 4.49: Time series of θ_* (K) for the entire simulation window.

Another parameter from similarity theory is the turbulence temperature scale (θ_*), given by Eq. (2.1b). Figure (4.49) illustrates the horizontally averaged temperature scale for both LES and WRF model solutions. With the exception of the YP2S configuration, each WRF model prediction modeled values close to those prescribed

by LES. The YP2S configuration again seemed to incorrectly calculate θ_*, as it failed to meet the condition that $H = |u_*\theta_*|$.

Next, estimates of the boundary layer depth were compared in time. Owing to the noisy nature of LES solutions in time, hourly estimates were extracted, as seen in Figure (4.50). Values represent the horizontal mean of boundary layer depth estimates across the comparison domain As discussed in (2.7.1), YP2S follows the flux method, whereas PP2S follows the gradient method, as outlined in (2.7.3). As summarized in (2.7.2), MP2S follows the TKE approach.

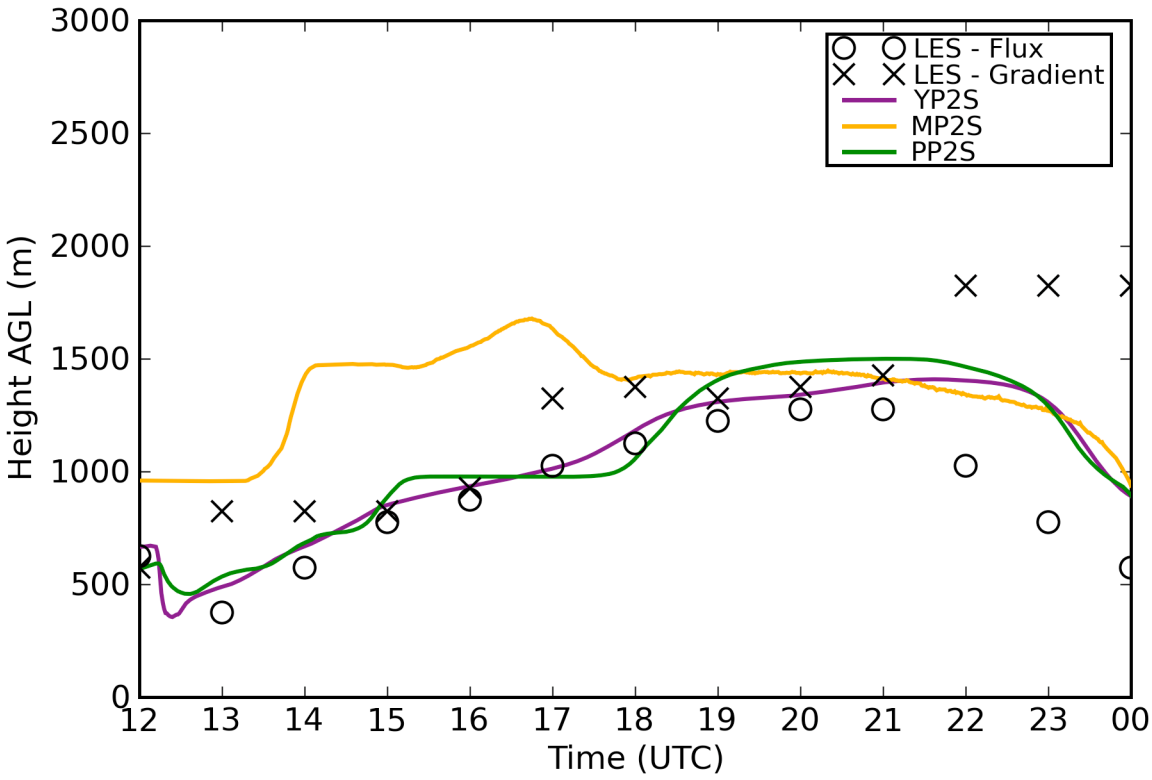

Figure 4.50: Time series of boundary layer depth (m) estimates for the entire simulation window. The flux method refers to finding the height in which virtual temperature flux reaches a minimum. The gradient method refers to finding the height in which the vertical gradient of virtual temperature reaches a maximum

At the beginning of the simulation window, every WRF model solution for boundary layer depth estimations fell between the flux and gradient methods of LES, with the exception of the MP2S configuration. As the day continued, MP2S greatly overprescribed the boundary layer depth compared to all other solutions. This is apparently due to an internal error in the aforementioned TKE method. Generally, all other configurations produced boundary layer depth estimates which fell between the flux method and gradient method. For all times, the flux method produced lower boundary layer heights than the gradient method. Overall, WRF model predictions of the boundary layer depth remained within range of the LES prescribed bounds, but were slightly overestimated throughout the course of the day. The boundary layer did not develop as much as in the Dryline Case due to the stronger static stability following the cold front.

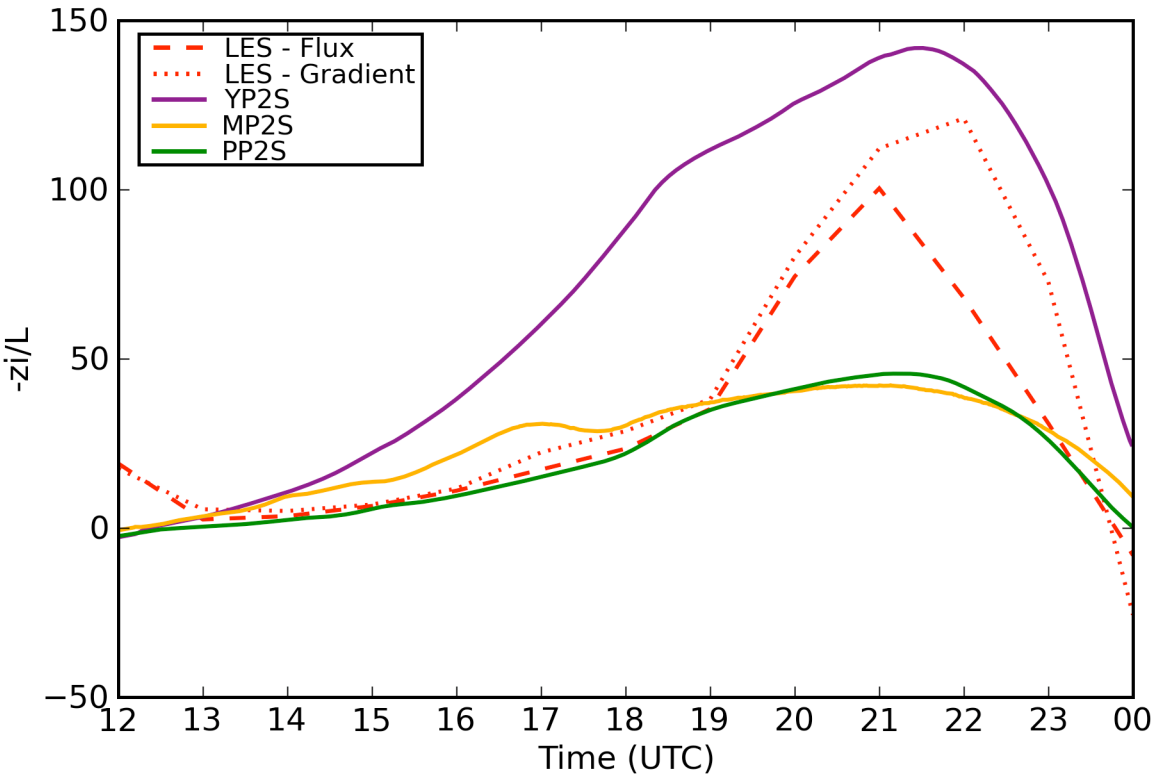

Figure 4.51: Time series of $(-zi/L)$ estimates for the entire simulation window.

Next, the quantity $-zi/L$ was investigated. Figure (4.51) illustrates the timeline evolution of $-zi/L$. Horizontal averages of zi and L were taken in time. From the start of the simulation window until 19UTC, model solutions remained relatively small and positive. This indicates that shear production dominated the boundary layer evolution. PP2S predictions were consistent with the LES solutions during this time, while YP2S was by far the largest due to its unrealistically large θ_*. The boundary layer depth overestimations by YP2S seems to confirm this behavior. After 19UTC, LES solutions predicted winds that approached zero. As the winds disappeared, the shear production terms decreased, meaning that L decreased. Accordingly, $-zi/L$ became large, meaning that buoyancy dominated the boundary layer growth. Oppositely, the WRF model predictions, sans YP2S, remained relatively small because they did not predict weakening winds to the extent of LES. Subsequently, L stayed larger and thusly $-zi/L$ remained smaller as compared to LES. While YP2S came close to predicting similar values to that of the LES solutions, it was a case of arriving at the correct solutions by the wrong reasons, as was detailed in the overprescription of θ_*. All solutions quickly approached stable conditions toward the end of the simulation window.

4.4 Discussion

Two cases offering different temporally inhomogeneous atmospheric environments were chosen to evaluate the adeptness of the WRF model in representing sub-grid scale atmospheric processes in terms of TTSI physics. The first case was deemed Dryline, as its simulation window occurred during the passage of a dryline. The day saw a dryline move through the comparison domain, leading to strong warming and wind shear allowing for a growing boundary layer. The second case was deemed Post-frontal, as a cold front preceded the simulation window. The day was marked with high pressure and cooler temperatures, along with an increased static stability.

As noted previously, there existed great differences among some of the instruments offered at the ARM site. Generally speaking, the ECOR and CO2FLX were closer than the EBBR measurement. Figures (4.52) and (4.53) demonstrate the scatter of surface sensible and latent heat fluxes, respectively, for the month of June 2007 for the EBBR and ECOR measurements. It is clear that the EBBR is biased toward the high end on latent heat flux and toward the low end on the sensible heat flux when compared to the ECOR data. However, when looking at the same scatter plots for CO2FLX and ECOR, as seen in Figures (4.54) and (4.55), there is a much higher correlation. This seems to indicate that the EBBR is the least reliable or consistent of the three measurement systems, and was accordingly precluded from comparison.

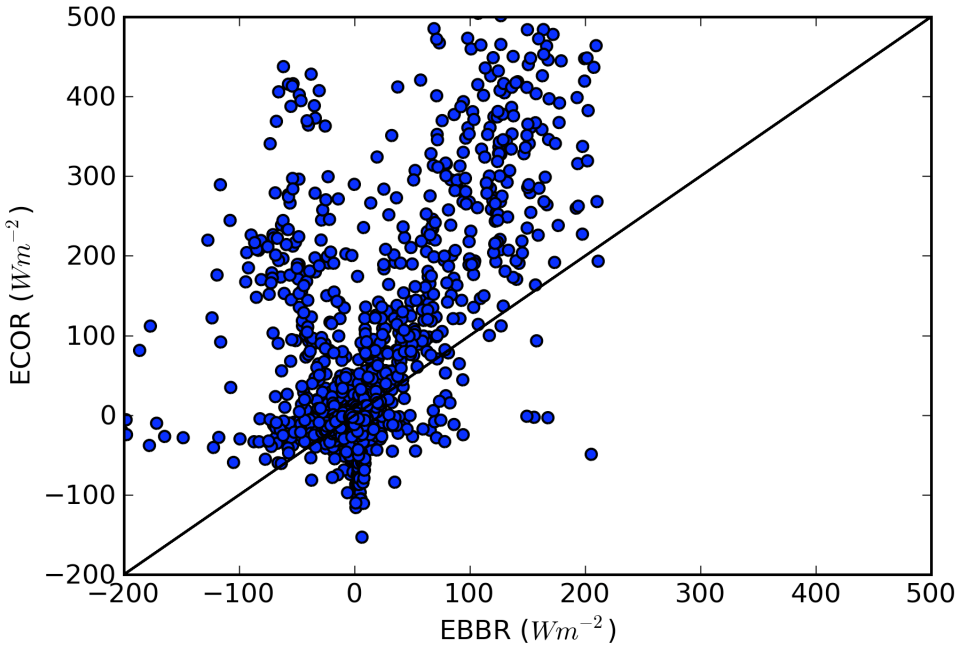

Figure 4.52: Scatter of surface sensible heat flux (Wm^{-2}) from the EBBR vs. ECOR for the month of June 2007 at the LMN ARM site.

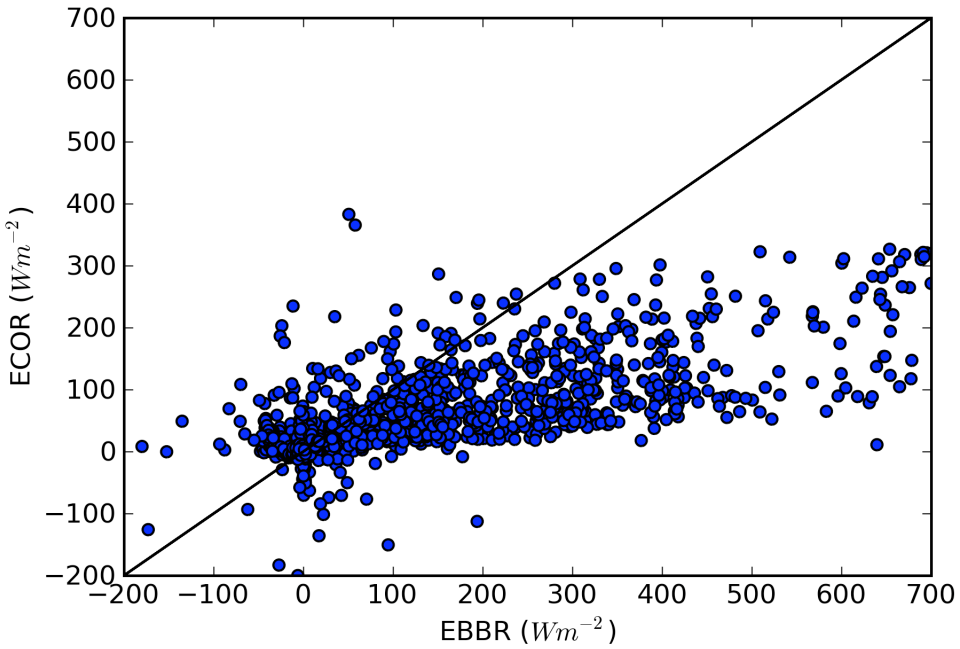

Figure 4.53: Scatter of surface latent heat flux (Wm^{-2}) from the EBBR vs. ECOR for the month of June 2007 at the LMN ARM site.

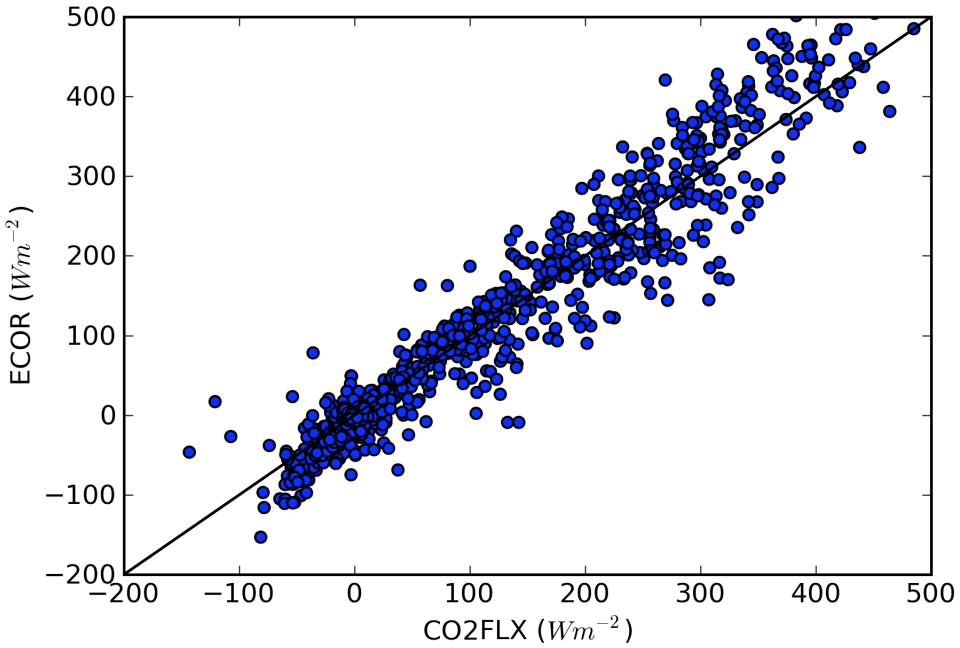

Figure 4.54: Same as Figure (4.52) except for CO2FLX vs. ECOR.

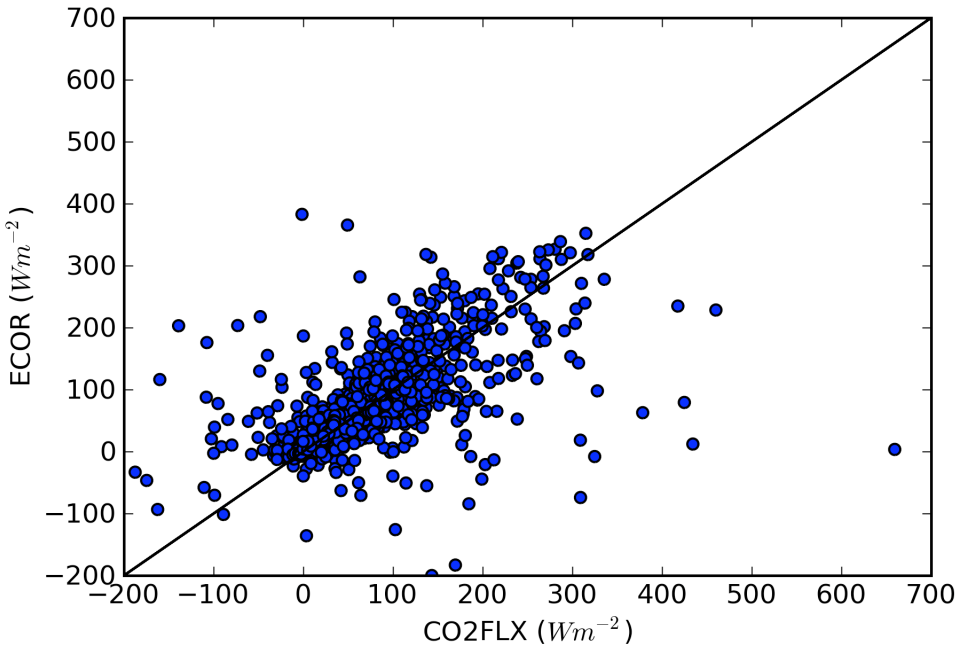

Figure 4.55: Same as Figure (4.53) except for CO2FLX vs. ECOR.

Generally, in both cases, the timeline analysis of atmospheric quantities matched well with those from LES. When looking at the vertical structure of these meteorological fields, it became evident that some TTSI schemes better represented vertical mixing and transport by turbulent means more than others. The YP2S and PP2S configurations routinely produced more realistic profiles of atmospheric features, denoted by a sufficiently deep well-mixed layer. On the other hand, MP2S routinely produced weaker mixing and a shallower well-mixed layer.

When looking at higher-order statistics, differences were seen between the WRF model and LMN measurements. Of note was the surface sensible and latent heat fluxes. Results in both cases indicate that WRF model predictions did not adequately partition surface fluxes, as was evident with the lower sensible heat flux and higher latent heat flux predictions. While the WRF model predictions for surface latent heat flux were overestimated by a notable amount as compared to the measurements, the fact that the sensible heat flux is more closely predicted has a far greater bearing on

the development of the boundary layer. This is why the WRF model estimates for the boundary layer depth were fairly close, as seen in Figures (4.25) and (4.50). This is explained by looking at vertical buoyancy flux, which is defined as

$$\overline{w'B'} = \underbrace{\frac{g}{\theta_r}\overline{w'\theta'}}_{C_\theta} + \underbrace{0.61g\overline{w'q'}}_{C_q} \ , \tag{4.3}$$

where C_θ represents the contribution by the kinematic heat flux and C_q is the contribution by the kinematic moisture flux. $B^{'}$ represents the perturbation of buoyancy. Using Eqs. (4.1) and (4.2) to solve for the respective kinematic fluxes yields

$$C_\theta = \frac{Hg}{c_p \rho \theta_r} \quad \text{and} \tag{4.4a}$$

$$C_q = \frac{0.61LEg}{L_v \rho} \ . \tag{4.4b}$$

Using order of magnitude reasoning, the individual contributions to scale as

$$C_\theta = \frac{\left[10^2\right]\left[10\right]}{\left[10^3\right]\left[1\right]\left[10^2\right]} = \left[10^{-2}\right] \tag{4.5a}$$

$$C_q = \frac{\left[10^2\right]\left[1\right]\left[10\right]}{\left[10^6\right]\left[1\right]} = \left[10^{-3}\right] \ . \tag{4.5b}$$

This indicates that the contribution to the vertical buoyancy flux by the surface sensible heat flux is an order of magnitude larger than that from the surface latent heat flux for the conditions present in this study. Accordingly, the boundary layer development throughout the day in both cases is driven mainly by an accurately prescribed surface sensible heat flux. Subsequently, none of the WRF model configurations were greatly affected by the sometimes large discrepancies observed in surface latent heat flux. Figures (4.56) and (4.57) illustrate the buoyancy flux for the Dryline Case and Postfrontal Case, respectively.

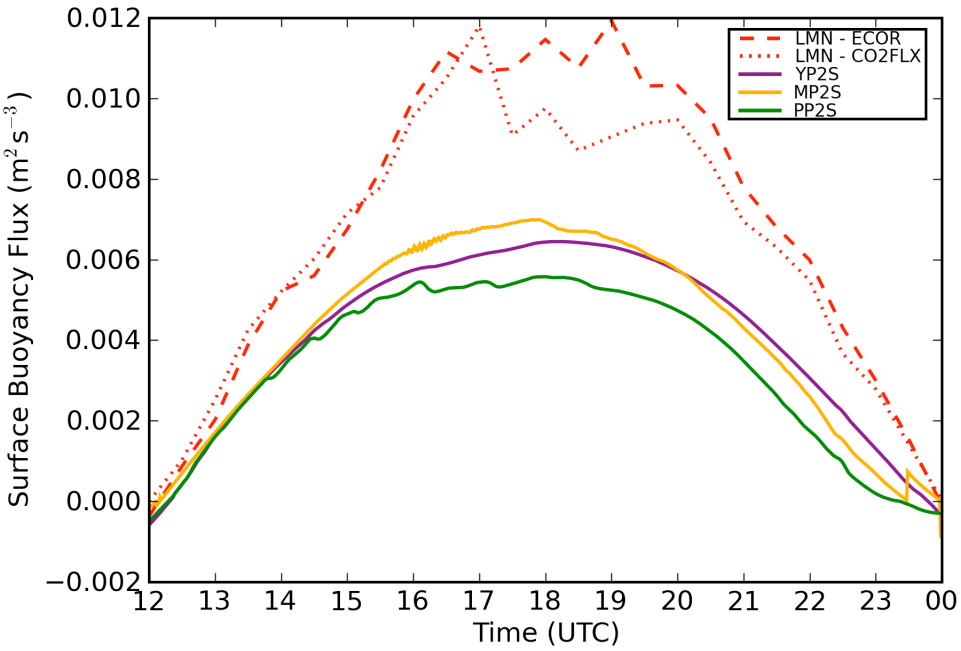

Figure 4.56: Surface buoyancy flux ($m^2 s^{-3}$) on June 7, 2007 for the entire simulation window.

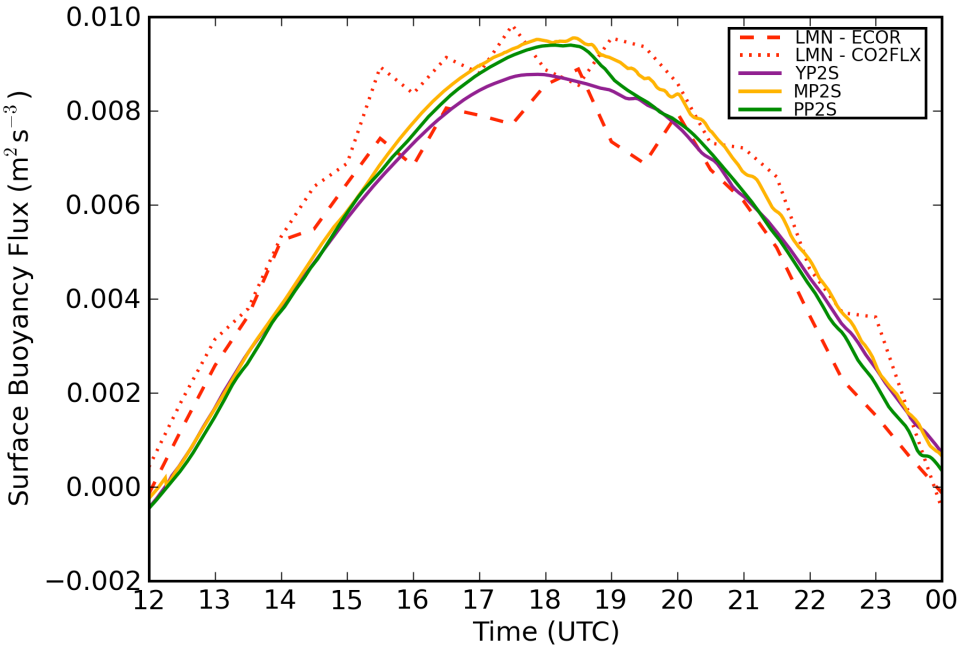

Figure 4.57: Surface buoyancy flux ($m^2 s^{-3}$) on June 8, 2007 for the entire simulation window.

Further higher-order fields include the turbulent scales of velocity and temperature. In the Dryline Case, WRF model results produced underestimated u_*, meaning the representation of turbulent shear production was underestimated. Additionally, θ_* was also slightly underestimated, with the exception of YP2S, which incorrectly calculated the turbulence temperature scale. This correlates with the reduced surface sensible heat flux. Boundary layer depths were generally consistent except for MP2S, which was due to an internal error. Lastly, $-zi/L$ was relatively small as turbulence shear production dominated the boundary layer growth. MP2S and PP2S closely followed the solutions from LES, whereas YP2S varied greatly, again due to the incorrect calculation of θ_*. In the Postfrontal Case, WRF model results produced overestimated u_*, meaning the representation of turbulent shear production was overrepresented. Additionally, θ_* was slightly underestimated, with the exception of YP2S, which incorrectly calculated the turbulence temperature scale. This correlates with the nearly equal surface sensible heat fluxes. Boundary layer depths were generally close, except for MP2S owing to the previously mentioned internal error. Lastly, $-zi/L$ became relatively larger in LES solutions than in the WRF model predictions because LES predicted stronger vanishing winds. Overall, $-zi/L$ was larger than in the Dryline Case, meaning that buoyant, convective motions acted to drive the boundary layer development. This is seen in Figures (4.56) and (4.57), as greater buoyancy flux existed during the Postfrontal Case.

During neutral or unstable conditions, it seemed evident that the YP2S and PP2S configurations generally best represented meteorological quantities and turbulence statistics when compared to LES solutions. The MP2S configuration routinely failed to reproduce the same mixing as the other two schemes. The explicit handling of the entrainment layer, as well as the approach to non-local mixing, seems to lend reasons why the YP2S and PP2S configurations generally performed the best. Each

scheme routinely outperformed all other configurations in the representation of turbulent parameters and boundary layer development. Conversely, as was evident with the beginning and ending of each simulation window, PP2S and MP2S performed the best under stable conditions. It appears that PP2S contained the best combination of similarity theory estimations and mixing effects. Given that PP2S performed well under most conditions present in this study, the settings contained within that configuration are recommended for use under the representative meteorological conditions present in this case.

Chapter 5

Summary and Conclusions

5.1 Final Remarks

The capabilities of a numerical weather prediction system to adequately parameterize sub-grid scale processes was investigated through two cases exemplifying inhomogeneous atmospheric environments representative of conditions found during late spring in Oklahoma. The Dryline Case included the passage of a dryline through the comparison domain, along with the associated warming, moisture changes, and wind shifts. The boundary layer growth on this day was notable and was mainly driven by shear production of turbulence. The Postfrontal Case was preceded by the passage of a cold front and included weakening winds associated with the movement of a surface high-pressure system, along with a dry and more stably stratified atmosphere. It should be noted that findings listed in this thesis are specific to the presented cases and should not be taken to apply in all cases.

One consistent behavior for both cases confirmed that the failure to utilize a PBL parameterization scheme, even at such fine-scale grid spacing as 1km, resulted in poor representation of turbulent mixing. This is a finding that is general enough to possibly apply in most cases because the model simply cannot adequately resolve turbulent eddies which are so important to the transport of momentum, heat and moisture. Unless implementing a computational grid with spacing on the order of a few hundred meters, the use of a PBL parameterization scheme is strongly suggested.

Additionally, the WRF model appeared to poorly partition surface fluxes. This behavior may result from the grid spacing used, in which contributions from explicit

calculations and parameterization schemes are not easily delineated, leading to an unknown additive effect. While the measurements from the LMN ARM site (not including EBBR) were generally considered sensible, the age of the instruments as well as some behavior listed in the manuals should lead to a careful approach to using such data. Assuming that the measurements were within reasonable bounds, it is clear that improvement is needed in how the WRF model partitions surface fluxes under certain meteorological conditions and model configurations. Varying the LSM used is one method to explore how fluxes work within the model. The noted behavior may simply highlight a problem in the NOAH LSM, while other schemes may work as expected.

Overall, meteorological conditions were adequately reproduced, but with insufficient turbulent mixing and transport as was represented by the fine-scale data from LES. Generally speaking, YP2S and PP2S reproduced mixing in the boundary layer more realistically than did MP2S. Further study is needed to investigate this behavior. This study clearly showed the spread among WRF model predictions based on TTSI configurations and hopefully elucidated the need to carefully consider which combination to use. Hopefully, the shortcomings of the schemes present in the WRF model illustrated the need for further study into the parameterization of sub-grid scale processes in NWP models, as was proposed so eloquently by Stensrud (2007). While the goals were met in so far as presenting comparability of WRF model predictions with observational and fine-scale simulation data, as well as offering the recommendation of PP2S, findings are somewhat limited in scope since only two case studies were shown. Formally, this limits the findings to those conditions present in this study, however, since representative conditions were employed, the results may be applied to slightly broader applications. Clearly, further research is needed to confirm results and illuminate WRF model behavior under different conditions.

5.2 Future Research

Future studies will seek to improve upon the methodologies provided in this thesis and offer broader insight into parameterization schemes. The first evident need is investigation of surface flux partitioning in the model. This could be done through implementing differing LSM, instead of only using the NOAH LSM, as there may be a problem with that particular scheme. Additionally, differing methods to represent fluxes needs further study. Methods to improve upon vertical mixing should be explored, as such mixing was generally underrepresented in the model. Additionally, the WRF model should be run in "LES-mode", in which horizontal grid spacing is fine enough to preclude the use of many parameterization schemes. This will allow for a more direct comparison of the underlying equations that drive both LES and the WRF model.

Also of importance is improving upon the representation of "truth" in comparability studies. LES should be run with finer grid spacing, allowing for a more realistic representation of atmospheric fields. In doing this, different methods should be implemented in order to best drive LES. Firstly, LES should be given horizontally inhomogeneous surface fluxes, instead of the uniform method currently employed. This will allow for a better delineation of the surface, especially when fluxes are far from uniform as was the case in the comparison domain. Secondly, different sources should be considered to nudge LES towards the large-scale atmospheric state. Such sources may include differing objective analyses and observational data. Studying different implementations of the nudging force should also be investigated. Hopefully the implementation of such experiments will elucidate the goals set forth in this thesis in a broader sense.

Bibliography

Beljaars, A. C. M., 1994: The parameterization of surface fluxes in large-scale models under free convection. *Quart. J. Roy. Meteor. Soc.*, **121**, 255–270.

Blackadar, A. K., 1976: Modeling the nocturnal boundary layer. *Preprints, Third Symp. on Atmospheric Turbulence and Air Quality*, Raleigh, NC, 46–49.

—, 1978: Modeling pollutant transfer during daytime convections. *Preprints, Fourth Symp. on Atmospheric Turbulence, Diffusion, and Air Quality*, Amer. Metor. Soc., Reno, NV, 443–447.

Chen, F. and J. Dudhia, 2001: Coupling an advanced land-surface/ hydrology model with the Penn State/ NCAR MM5 modeling system. Part 1: Model description and implementation. *Mon. Wea. Rev.*, **129**, 569–585.

Davies, H. C. and R. E. Turner, 1977: Updating prediction models by dynamical relaxation: an examination of the technique. *Quart. J. Roy. Meteor. Soc.*, **103**, 225–245.

Deardorff, J. W., 1972: Numerical investigation of neutral and unstable planetary boundary layers. *J. Atmos. Sci.*, **29**, 91–115.

Dudhia, J., 1989: Numerical study of convection observed during the winter monsoon experiment using a two-dimensional model. *J. Atmos. Sci.*, **46**, 3077–3107.

—, 2008: WRF Physics Options, Technical documentation for general WRF model users.

Dyer, A. J. and B. B. Hicks, 1970: Flux-gradient relationships in the constant flux layer. *Quart. J. Roy. Meteor. Soc.*, **96**, 715–721.

Fedorovich, E., R. Conzemius, and D. Mironov, 2004: Convective entrainment into a shear-free linearly stratified atmosphere: bulk models reevaluated through large eddy simulations. *J. Atmos. Sci.*, **61**, 281–295.

Fedorovich, E., T. M. Nieuwstadt, and R. Kaiser, 2001a: Numerical and laboratory study of horizontally evolving convective boundary layer. Part I: Transition regimes and development of the mixed layer. *J. Atmos. Sci.*, **58**, 70–86.

—, 2001b: Numerical and laboratory study of horizontally evolving convective boundary layer. Part II: Effects of elevated wind shear and surface roughness. *J. Atmos. Sci.*, **58**, 546–560.

Holtslag, A. A. M. and B. A. Boville, 1993: Local versus non-local boundary layer diffusion in a global climate model. *J. Climate*, **6**, 1825–1842.

Hong, S., H. M. H. Juang, and Q. Zhao, 1998: Implementation of prognostic cloud scheme for a regional spectral model. *Mon. Wea. Rev.*, **126**, 2621–2639.

Hong, S., Y. Noh, and J. Dudhia, 2006: A new vertical diffusion package with an explicit treatment of entrainment processes. *Mon. Wea. Rev.*, **134**, 2318–2341.

Janjic, Z. I., 1994: The step-mountain eta coordinate model: further developments of the convection, viscous sublayer, and turbulence closure schemes. *Mon. Wea. Rev.*, **122**, 927–945.

—, 1996: The surface layer in the NCEP Eta Model. *Preprints, Eleventh Conf. on Numerical Weather Prediction*, Boston, MA, 354–355.

—, 2002: Nonsingular Implementation of the Mellor-Yamada 2.5 Scheme in the NCEP Meso Model. Technical report, NCEP, USA.

Lin, S., R. D. Farley, and H. D. Orville, 1983: Bulk parameterization of the snow field in a cloud model. *J. Climate Appl. Meteor.*, **22**, 1065–1092.

Mellor, G. L. and T. Yamada, 1982: Development of a turbulence closure model for geophysical fluid problems. *Rev. Geophys. Space Phys.*, **20**, 851–875.

Mlawer, E. J., S. J. Taubman, P. D. Brown, M. J. Iacono, and S. A. Clough, 1997: Radiative transfer for inhomgeneous atmosphere: Rrtm, a validated correlated-k model for the longwave. *J. Geophys. Res.*, **102**, 16663–16682.

Monin, A. S. and A. M. Obukhov, 1954: Basic Laws of turbulent mixing in the surface layer of the atmosphere. *Contrib. Geophys. Inst. Acad. Sci., USSR*, **151**, 163–187.

Panofsky, H. A., 1963: Determination of stress from wind and temperature measurements. *Quart. J. Roy. Meteor. Soc.*, **89**, 85–94.

Paulson, C. A., 1970: The mathematical representation of wind speed and temperature profiles in the unstable atmospheric surface layer. *J. Appl. Meteor.*, **9**, 857–861.

Pleim, J. E., 2006: A simple, efficient solution of flux-profile relationships in the atmospheric surface layer. *J. Appl. Meteor. and Clim.*, **45**, 341–347.

—, 2007: A combined local and non-local closure model for the atmospheric boundary layer. Part 1: Model description and testing. *J. Appl. Meteor. and Clim.*, **46**, 1383–1395.

Pleim, J. E. and J. S. Chang, 1992: A non-local closure model for vertical mixing in the convective boundary layer. *Atmos. Environ.*, **26A**, 965–981.

Skamarock, W. C., J. B. Klemp, J. Dudhia, D. O. Gill, D. M. Barker, W. Wang, and J. G. Powers, 2008: A Description of the Advanced Research WRF Version 3. Technical report, NCAR, USA.

Smagorinsky, J., 1963: General Circulations Experiments With The Primitive Equations. *Mon. Wea. Rev.*, **91**, 99–164.

Stensrud, D. J., 2007: *Parameterization Schemes - Keys to Understanding Numerical Weather Prediction Models*. Cambridge University Press, New York, 459 pp.

Webb, E. K., 1970: Profile relationships: The log-linear range, and extension to strong stability. *Quart. J. Roy. Meteor. Soc.*, **96**, 67–90.

Zhang, D. L. and R. A. Anthes, 1982: A high resolution model of the planetary boundary layer - sensitivity test and comparisons with SESAME-79 data. *J. Appl. Meteor.*, **21**, 1594–1609.

Zilitinkevich, S. S., 1995: Non-local turbulent transport: pollution dispersion aspects of coherent structure of convective flows. *Air Pollution III - Air Pollution Theory and Simulation*, Computational Mechanics Publications, Southampton Boston, volume 1, 53–60.